UNIVERSITY OF CALIFORNIA
RIVERSIDE

Quantum Transport in Misoriented Layers of Graphene: Physics and Device Applications

A Dissertation submitted in partial satisfaction
of the requirements for the degree of

Doctor of Philosophy

in

Electrical Engineering

by

K. M. Masum Habib

December 2013

Dissertation Committee:
Dr. Roger K. Lake, Chairperson
Dr. Alexander A. Balandin
Dr. Jing Shi

The Dissertation of K. M. Masum Habib is approved:

Committee Chairperson

University of California, Riverside

Acknowledgments

I would like to express my hear-felt gratitude and appreciation to my supervisor Roger Lake for teaching everything I know about quantum transport and device modeling. Without his constant guidance, this work would not be possible. I would also like to thank my lab-mates for their friendship and support.

I acknowledge the activities of student community of Bangladesh at UCR through which I found a living Bangladesh around myself. I would like to thank my family for supporting me to pursue my dreams. Within all of their limitations they provided me with the best. Last but not least, I would like to thank my beloved wife for a wonderful, enjoyable journey through the graduate student life.

The text of this dissertation, in part or in full, is a reprint of the material as it appears in the following journals and/or proceedings:

- Applied Physics Letters [1]. Reprinted with permission from [1]. © [2011] American Institute of Physics.

- Physical Review B. [2]. Reprinted with permission from [2]. © [2012] American Physical Society.

The co-author Roger K. Lake, listed in the above publications directed and supervised the research which forms the basis for this dissertation. The remaining co-authors listed provided technical expertise and support as collaborators. This work

is supported in part by the Microelectronics Advanced Research Corporation Focus Center on Nano Materials (FENA) and FAME, one of the six centers of STARnet, a Semiconductor Research Corporation program sponsored by MARCO and DARPA.

To my family

ABSTRACT OF THE DISSERTATION

Quantum Transport in Misoriented Layers of Graphene: Physics and Device Applications

by

K. M. Masum Habib

Doctor of Philosophy, Graduate Program in Electrical Engineering
University of California, Riverside, December 2013
Dr. Roger Lake, Chairperson

Graphene is one of the promising candidates for the channel material of future electronic devices. Negligible spin-orbit coupling combined with high carrier mobility and long mean free path make graphene a very attractive material for post CMOS device applications. The individual layers in a misoriented or twisted stack of graphene behave as if they were electronically decoupled due to destructive quantum interference. The interlayer coupling is increased and the Fermi velocity is reduced in presence of a vertical electric field and negative differential conductance is predicted at small biases. These properties of misoriented graphene can potentially be exploited in novel switching mechanisms. In order to utilize these exceptional properties in device applications, it is important to understand if these phenomena still hold in the limit of nanoscaled device dimensions.

Our numerical simulations show that the coherent electronic decoupling between the layers of two-dimensional misoriented bilayer graphene is still present in lower dimensions when the misoriented region is reduced to the nanometer scale. We found a novel current switching mechanism in nanoscaled misoriented graphene layers that

utilizes the voltage controlled quantum interference of electrons to achieve large, rapid modulation of the current with small voltage swings. Utilizing the voltage controlled quantum interference between standing electronic waves we demonstrated an oscillatory current voltage response suitable for multi-state switching. This switching mechanism does not rely on a bandgap or a potential barrier. Thus, it is not limited by the thermal limitation of 60 mV/dec.

The coherent, interlayer resistance of a misoriented, rotated interface in vertically stacked graphene is determined for a variety of misorientation angles. The fundamentally limiting quantum-resistance of the ideal interface with $\theta = 0^{\circ}$ is on the order of 10^{-3} $\Omega\mu\text{m}^2$. For small rotations, the coherent interlayer resistance is a strong function of the Fermi energy, and it exponentially approaches the ideal quantum resistance at energies away from the charge neutral point. At room temperature, the total interlayer resistance can still be sensitive to the rotation angle changing one to two orders of magnitude as the angle changes by a few degrees. Over a range of intermediate angles, the coherent resistance is much larger than the phonon-mediated resistance which results in a relatively constant total resistance on the order of 100 $\Omega\mu\text{m}^2$.

Contents

List of Tables

List of Figures

Chapter 1

Rationale

1.1 Introduction

As the continuous down scaling of the conventional silicon metal-oxide-semiconductor field-effect transistor (MOSFET) is approaching its fundamental limits, the need for alternative channel materials and device architectures is growing fast. Graphene, a sheet of carbon atoms arranged in a honeycomb structure, is one of the promising candidates for the channel material of future electronic devices. Negligible spin-orbit coupling combined with high carrier mobility and long mean free path make graphene a very attractive material for post CMOS electronic devices. Although graphene has many exceptional electronic and mechanical properties, lack of a bandgap reduces its utility for conventional electronic device applications. A bandgap can be opened by various means but it is difficult to create a sufficiently large bandgap without degrading the electronic properties of graphene. One approach to circumvent the bandgap problem is to utilize the unique properties of graphene in alternative device architectures which is one of the primary objectives of this work.

One remarkable property of graphene is that when graphene layers are stacked together, as often is the case in chemical vapor deposition (CVD) and multilayer epitaxial graphene, a relative rotation between the layers is introduced [4, 5]. Bilayer graphene with a relative rotation between the layers is known as misoriented or twisted bilayer graphene (TBG). It is established that the individual layers in TBG with a relative rotation angle greater than 20° are electronically decoupled [6–9]. The decoupling results from the destructive quantum interference between the electron wave functions of the top and bottom graphene layers [6–8]. An interesting property of TBG from the application point of view is that the inter layer coupling is increased [10] and the Fermi velocity is reduced [11] in presence of a vertical electric field, and negative differential conductance is predicted at small biases [12].

In search for a replacement of conventional transistor, this dissertation has been primarily focused on understanding the exceptional properties of misoriented graphene layers and design, modeling and simulation of novel electronic devices that utilize these properties. My work exploits the voltage controlled quantum interference of twisted bylayer graphene to achieve large, rapid modulation of the current with small voltage swings. The physical mechanism of such current modulation does not rely on a bandgap, or tunneling through or transmission over a potential barrier. Thus, it is not limited by the thermal limitation of 60 mV/dec.

Novel electronic devices constructed from multiple heterogeneous layers of van der Waals materials are being proposed with estimates of extremely high-frequency operation. In general, there will be misorientation between the layers. Understanding how the misorientation affects the inter-layer resistance is essential for engineering and determining the performance metrics of such devices. In this work, he coherent, interlayer resistance of a misoriented, rotated interface in vertically stacked graphene is determined for a variety of misorientation angles. These values are compared

with previously calculated values for the phonon-mediated, interlayer resistance of misoriented bilayer graphene.

1.2 Background and Motivation

Driven by Moore's law, the semiconductor industry has scaled down the feature sizes of MOSFET to improve the performance of CMOS circuits. After aggressive down scaling over the last half century the feature sizes of MOSFET have reached the length scale comparable to the atomic lengths. Further down scaling of the channel length will reach a functional limit within the next decade as predicted by most semiconductor industry projections. Over the past several years there has been an intense debate concerning the future of such nanoscaled electronic devices and search for alternatives has been growing fast.

Carbon based electronics is one of the potential candidates in low-power post CMOS logic alternative. This idea of carbon base electronics has been around since the discovery of carbon nanotubes (CNT) [13]. Although CNTs have demonstrated nearly ideal switching characteristics, increased device speed, and lower power consumption than traditional CMOS logic by utilizing band-to-band tunneling [14], their implementation has been unsuccessful due to the fact that the metallic CNTs can not be sorted from semiconducting ones.

Recently, graphene has been being studied extensively as another possible platform for carbon based electronics. High carrier mobility, negligible spin-orbit coupling and long coherence length [15–17] make graphene a very attractive material for post CMOS electronic devices. However, lack of a bandgap in graphene [17, 18] is one of the challenges for achieving high ON/OFF current ratios in graphene field effect transistors (FETs).

A bandgap can be introduced by patterning a 2D graphene sheet into a narrow (<10 nm) nanoribbon, known as a graphene nanoribbon (GNR) [19–21]. Another way to modify the band structure of graphene is to stack two monolayers to form a bilayer in which the bandgap can be tuned by creating a potential difference between the two layers [22–24]. A bandgap can also be introduced by using chemical doping [25–27]. However, it is difficult to create a sufficiently large bandgap without degrading the electronic properties of graphene.

The possibility of field effect transistors (FETs) using bilayer graphene as the channel material was recently studied [28]. It was shown that such a FET had a poor on-off current ratio, $I_{\rm on}/I_{\rm off}$, due to strong band-to-band tunneling. However, a tunnel FET using bilayer graphene showed promising performance [29].

One way to circumvent the bandgap problem is to utilize the unique properties of graphene in alternative FET architectures [30–34]. A highly nonlinear current-voltage relationship can be obtained in a graphene-insulator-graphene p-n junction [35]. Some devices exhibiting negative differential resistance (NDR) have been proposed [36–39]. However, most of these devices have relatively complex architectures [33, 34, 36–38], limited scalability [30], or low on-off or peak-to-valley current ratios [38, 39].

Interest in twisted, or misoriented, layers of graphene was recently motivated by the need to understand the electronic properties of multilayer graphene furnace-grown on the C-face of SiC [4]. Experimental analysis showed that the layers tended to be rotated with respect to each other at certain angles corresponding to allowed growth orientations with respect to the SiC substrate [5]. Calculations, based on density functional theory [4, 5, 7, 8], empirical tight binding [40] and continuum [6] models for such rotated bilayers found linear dispersion near the K-points. A recent experiment showed that in twisted bilayer graphene for twist angles greater than $\sim 3^{\rm o}$, the low-energy carriers behave as massless Dirac Fermions with a reduced Fermi

velocity compared to that of single layer graphene, and that for twist angles greater than 20°, the layers are effectively decoupled and act as independent layers [9]. The decoupling results from the destructive quantum interference between the electron wave functions of the top and bottom graphene layers [8]. The interlayer coupling is increased [10] and the Fermi velocity is reduced [11] in presence of a vertical electric field, and negative differential conductance is predicted at small biases [12]. The voltage controlled coupling in misoriented graphene layers opens up possibilities of novel switching mechanisms.

Although the physics of the decoupled layers in twisted bilayer graphene has been studied extensively, it is not clear if these properties still hold in the limit of nanoscaled device dimensions, for example, in the twisted bilayer that occurs in the overlap region of two crossed GNRs fabricated by unzipping two carbon nanotubes [41]. Understanding the physical mechanism of interlayer transport in nano scaled twisted bilayer graphene is one of the motivations of this dissertation.

There is rapidly growing interest in vertically stacked van der Waals materials for electronic device applications [33, 42–47]. In such structures the interfaces between different materials will, in general, be misoriented with respect to each other [48]. THz cutoff frequencies have been predicted for such devices [46]. At such high frequencies, any small series resistance can degrade performance. For example, an emitter contact resistance of 2.5 $\Omega\mu\text{m}^2$ is required to achieve a THz cutoff frequency in a heterostructure bipolar transistor [49]. Understanding the effect of the misorientation on the interlayer resistance is required to fully understand the design requirements and performance of proposed vertically stacked devices.

The most well studied and well understood van der Waals material is graphene [17, 48]. Although the effect of misorientation on the electronic structure of bilayer graphene has been studied extensively [4–9, 40, 50–52], the study of the interlayer

resistance in misoriented bilayer graphene has received far less attention [3, 12, 53]. Bistritzer and MacDonald used a transfer Hamiltonian approach to calculate the coherent interlayer resistance as a function of rotation angle θ and found it to vary by 16 orders of magnitude as the misorientation angle varies from zero degree to 30 degrees [12]. In the method of Ref. [12], the calculated quantitative values of the coherent interlayer resistance depend inversely on the value of the 75 meV lifetime (Γ) used in the calculation. Thus, the quantitative values of the interlayer resistance cannot be determined from this approach without knowing the actual values of the lifetime broadening Γ.

The room-temperature, phonon-mediated interlayer resistance shows far less dependence on the misorientation angle [3, 53]. It changes by less than an order of magnitude as the angle varies from zero to 30 degrees [3, 53]. The room-temperature, phonon-mediated interlayer resistance is a smooth, monotonic function of the misorientation angle.

To first order, the resistance from the coherent channel (R_c), and the resistance from the phonon-mediated channel (R_p) are in parallel [54, 55]. Thus, to determine the total inter-layer resistance between two misoriented graphene layers, one requires quantitative values for the coherent component of the resistance. In this work, we provide those values. Combining our values for R_c with the values calculated previously for R_p, we obtain estimates for the total room-temperature interlayer resistance for a variety of commensurate misorientation angles.

1.3 Objective

Misoriented graphene has interesting electronic properties that can potentially be used for current switching in post CMOS devices. However, several open questions

needed to be answered before the properties of misoriented graphene can be considered for device applications. Although the physics of twisted bilayer graphene is well understood, the scaling effect of misoriented layers is yet to be determined. Quantitative study of interlayer resistance in misoriented graphene interfaces is also an important issue for devices constructed from multiple heterogeneous layers of van der Waals materials.

The objective of this dissertation is to answer aforementioned open questions using theoretical studies. In this study, the electronic properties of misoriented graphene layers is modeled using density functional theory (DFT), extended Hückel theory (EHT) or empirical tight binding (TB) models. The quantum transport is taken into account using the non equilibrium Green's functional formalism (NEGF). Wave function approach is employed to elucidate the underlying physics.

To facilitate the computation, several numerical simulators were developed. The programming was done in C++, Fortran (F90), MATLAB and shell scripts along with numerically efficient math libraries such as BLAS, LAPACK and ScaLAPACK. These simulators were run on in-house compute clusters in parallel computing environment. The parallelization was done using the message passing interface library MPICH2. In C++, the math libraries like BLAS and LAPACK were integrated using armadillo and boost libraries.

1.4 Layout

The rest of this dissertation is organized as follows. In chapter 2, quantum transport in two independently contacted, AA or AB stacked graphene nanoribbons is presented. It is shown that this system behave as a resonant tunneling diode featuring negative differential resistance. Current modulation by voltage control of the quantum

phase in two infinite crossed GNRs is discussed in chapter 3. Utilizing the voltage controlled quantum interference between standing electronic waves in semi-infinite crossed GNR we demonstrated an oscillatory current voltage response suitable for multi-state switching in chapter 4. In chapter 5, the coherent, interlayer resistance of a misoriented, rotated interface in vertically stacked graphene is determined for a variety of misorientation angles. Finally, in chapter 6 we summarize the key findings of this thesis. In Appendix A the user manual and tutorials of Twister is given. Twister is the C++ code that can calculate the electronic structure and vertical transport of misoriented layers of vdW materials. Tutorials on armadillo and boost libraries are given in Appendix B.

Chapter 2

Negative Differential Resistance in Bilayer Graphene Nanoribbons

Lack of a bandgap is one of the significant challenges for application of graphene as the active element of an electronic device. A bandgap can be induced in bilayer graphene by application of a potential difference between the two layers. The simplest geometry for creating such a potential difference is two overlayed graphene nanoribbons independently contacted. Calculations, based on density functional theory and the non-equilibrium Green's function formalism, show that transmission through such a structure is a strong function of applied bias. The simulated current voltage characteristics mimic the characteristics of resonant tunneling diode featuring negative differential resistance.

2.1 Introduction

Graphene has fascinating electronic properties featuring the Dirac fermion [15] with high mobility [16] and a long coherence length. However, lack of a bandgap in two-

dimensional (2D) graphene [18] reduces its utility for conventional electronic device applications. A bandgap can be introduced by patterning a 2D graphene sheet into a narrow (<10nm) nanoribbon, known as a graphene nanoribbon (GNR) [20, 21]. Another way to modify the band structure of graphene is to stack two monolayers to form a bilayer in which the bandgap can be tuned by creating a potential difference between the two layers [23, 24].

The possibility of field effect transistors (FETs) using bilayer graphene as the channel material was recently studied [28]. It was shown that such a FET had a poor on-off current ratio, $I_{\text{on}}/I_{\text{off}}$, due to strong band-to-band tunneling. However, a tunnel FET using bilayer graphene showed promising performance [29]. Other proposed devices include a nanoelectromechanical FET based on interlayer distance modulation [56, 57], a FET utilizing a bilayer exciton condensate [31] and GNR junction diodes featuring negative differential resistance based on chemical [39] and field effect [38] doping.

Many proposed FET type graphene based devices have multiple gates making them relatively complex device structures. We consider the simplest possible geometry by which a potential can be applied between two GNR layers. Such a geometry consists of two single layer GNRs with one placed on top of the other. Each GNR is independently contacted such that one GNR is held at ground while the other has a bias applied to it. Such a geometry and biasing scheme would occur, for example, in a cross-bar architecture. Independently contacting the top and bottom GNR maximizes the voltage drop between them. Assuming that the majority of the potential drop occurs between the two nanoribbons, the potential difference between the two nanoribbons is the applied bias. Since the bandgap increases with applied source-drain bias, we hypothesized that negative differential resistance (NDR) would occur.

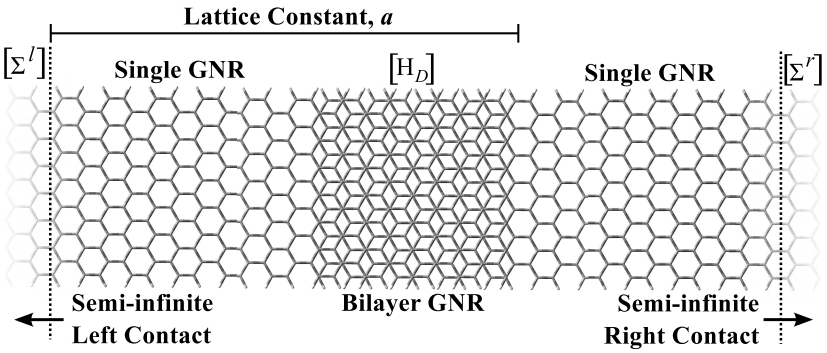

Figure 2.1: Atomic geometry of modeled AB–stacked device.

2.2 Method

To test this hypothesis, we performed numerical simulations of a model GNR geometry using *ab-initio* density functional theory (DFT) to simulate the electronic structure and a non-equilibrium Green's Function (NEGF) approach to determine the electron transport. The model structure of the overlapping GNRs is shown in Fig. 2.1. It consists of a left and a right semi-infinite, armchair, H-passivated GNR which overlap in the central region. Two well known bilayer stacking sequences, AB and AA, are considered. The widths of the armchair GNRs (AGNRs) are chosen to be 14 atomic C layers (3n+2) $\sim$ 1.8 nm to minimize the bandgap resulting from the finite width. The bandgap of the 14-AGNR calculated from DFT code, Fireball [58, 59], is 130 meV which is in good agreement with Son *et al.* [60]. When one GNR is stacked on top of another to form AB or AA bilayer GNRs, the bandgap is reduced further consistent with the results of Lam and Liang [21]. For AA GNR, the bandgap is removed completely, and for AB GNR, the bandgap is reduced to 20 meV. The lengths of the overlap regions for AB and AA stacking are 1.7 nm and 1.6 nm, respectively. The total simulated length between the two ideal leads indicated by the self-energies in Fig. 2.1 is $\sim$ 6.8 nm. Transmission through similar systems in equilibrium and with gate bias was recently studied in detail with π-band and $\mathbf{k}\cdot\mathbf{p}$

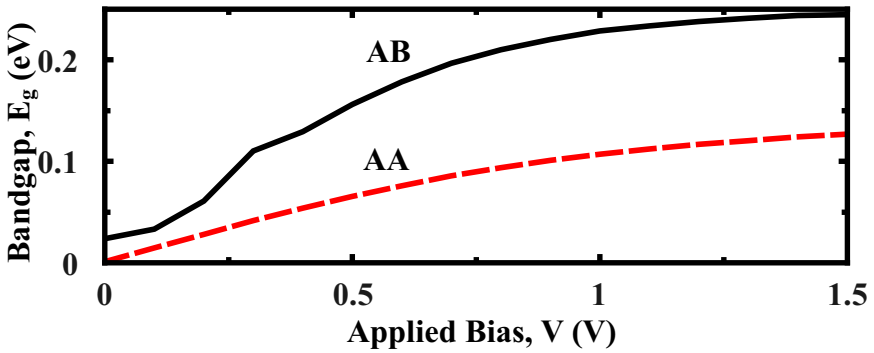

Figure 2.2: Bandgap as a function of applied bias for infinite AA– and AB–stacked bilayer GNRs.

models [61, 62], and strong resonant and anti-resonant features were observed in the transmission in agreement with our results below.

Both the AA and AB GNR bilayers are either metallic or have a bandgap less than k_BT at room temperature. Creating a potential difference between the two layers creates a bandgap with a maximum of 0.25 eV for the AB GNR and 130 meV for AA GNR as shown in Fig. 2.2. Understanding the band structure of the bilayer GNRs and the effect of bias, we are now ready to investigate the current-voltage response of the structure shown in Fig. 2.1. Before doing so, we provide a brief description of the theoretical models.

The electronic structure of the GNRs and bilayer GNRs is modeled with the quantum molecular dynamics, DFT code Fireball using separable, nonlocal Troullier-Martins pseudopotentials [63], the BLYP exchange correlation functional [64, 65], a self-consistent generalization of the Harris-Foulkes energy functional [66, 67] known as DOGS after the original authors [68,69], and a minimal sp^3 Fireball basis set. The radial cutoffs of the localized pseudoatomic orbitals forming the basis are $r_c^{1s} = 4.10$ Å for hydrogen and $r_c^{2s} = 4.4$ Å and $r_c^{2p} = 4.8$ Å for carbon [70].

A super-cell of hydrogen passivated single layer armchair GNR with periodic boundary conditions is relaxed quantum-mechanically with Fireball. The relaxed sin-

gle layer super-cell is then repeated to construct single-layer GNRs. These single-layer GNRs are then placed one above the other at the experimental separation distance of 3.35 Å and aligned to form the AB stacked structure shown in Fig. 2.1. The same procedure is followed to form the AA stacked structure with a separation distance of 3.55 Å. No further relaxation is performed on the structure. The region between the vertical lines in Fig. 2.1 is used as the supercell for bilayer GNR with lattice vector, **a**. A single point self-consistent calculation is performed with Fireball to generate the Hamiltonian matrix elements of this super-cell. The matrix elements within 16 atomic layers of the end overlap regions are discarded and replaced with the matrix elements for the relaxed single-layer GNR.

The applied bias is modeled by applying a rigid shift to the energy of the lower GNR by the amount of the applied bias, $U = -eV$. The matrix elements of U are calculated as $\langle i, \alpha | U | j, \beta \rangle = S_{\alpha_i, \beta_j} \left[U(\mathbf{r}_i) + U(\mathbf{r}_j) \right] / 2$ where, the indices i and j label the atoms, the indices α and β label the basis orbitals, and S_{α_i, β_j} is the overlap matrix $\langle i, \alpha | j, \beta \rangle$. $U(\mathbf{r}_i) = U$ for atoms on the lower GNR and zero for atoms on the upper GNR. This approach in which the matrix elements have the same form as in an extended Huckel model has been used by others [71]. The approach captures the Stark effect, but not non-equilibrium self-consistency. These and the Fireball Hamiltonian matrix elements are used in the NEGF algorithm to calculate the surface self-energies, Green's function of the device, the spectral function, the transmission, and the current as described in Ref. [72].

2.3 Results and Discussion

The simulated $I-V$ characteristics for the AB– and AA–stacked GNRs corresponding to Fig. 2.1 are shown in Fig. 2.3. Both the AB and AA structure exhibit NDR. The

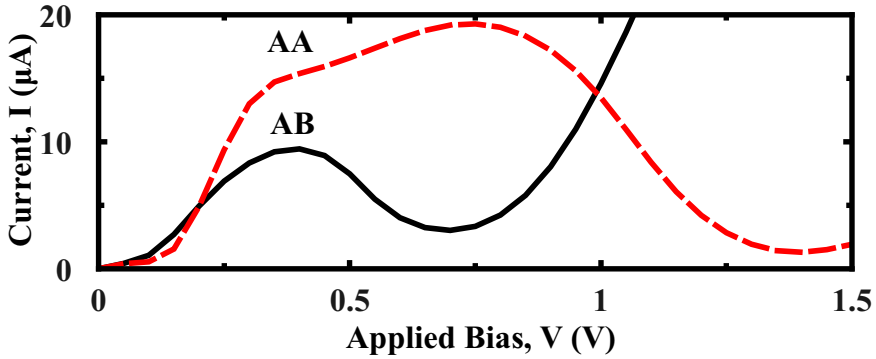

Figure 2.3: Simulated current voltage ($I-V$) characteristics of AA– and AB–stacked device. The valley current minimums occur at 0.7 V and 1.4 V for AB– and AA–stacked device, respectively.

peak current of the AB structure occurs at 0.4 V and the valley minimum occurs at 0.7 V. The peak and valley voltages for the AA structure are approximately twice those of the AB structure. Thus, the model structure does exhibit NDR confirming the initial hypothesis.

As a check, we repeated the $I-V$ calculation of the AB stacked structure using a π-bond model with tight-binding parameters for the intra-layer coupling (-2.569 eV) and the inter-layer coupling (-0.361 eV) taken from Ref. [22]. The peak and valley currents resulting from the π-bond model were, respectively, 24.5 μA and 2.1 μA, occurring at the peak and valley voltages of 0.5 V and 1.0 V. Thus, the two models, DFT and π-bond, give qualitatively the same $I-V$ with the π-bond model giving approximately twice the peak current and 4 times the peak-to-valley ratio as the DFT model.

To understand the $I-V$ characteristics shown in Fig. 2.3, the transmission coefficients are plotted as a function of electron energy. The transmission plots for the AB structure are shown in Fig. 2.4(a) and (b) at the peak and valley bias voltages, $V = 0.4$ V and $V = 0.7$ V, respectively. In both figures, the unbiased transmission and the biased quasi-Fermi levels of the left and right contacts are shown for reference.

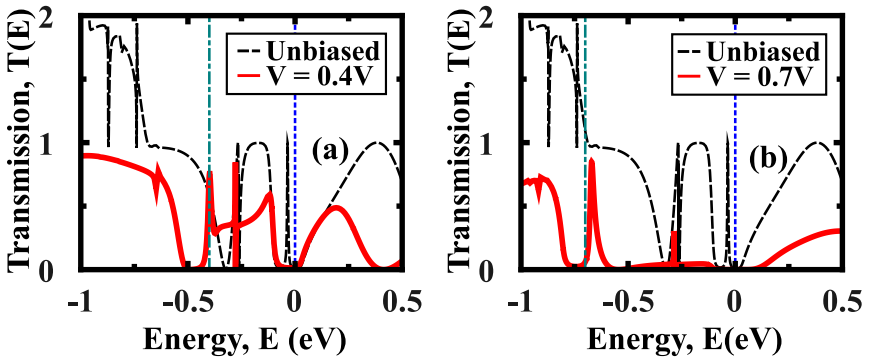

Figure 2.4: Transmission as a function of energy for AB–stacked device: (a) at bias, $V = 0.4$ V and (b) at bias, $V = 0.7$ V, superimposed on transmission at no bias. The vertical lines at the lower and upper energies represent the quasi-Fermi levels of right and left contacts, respectively. The quasi-Fermi level of the left contact is set at 0.

In agreement with and as discussed in [61, 62], the transmission shows a Fabry-Perot resonant feature at low energy and both resonances and antiresonances at more excited energies. The ends of the GNRs result in potential discontinuities at both ends of the overlap region giving rise to a resonant cavity in which multiple reflections can occur. At higher and lower energies multiple subbands allow multiple paths which can constructively or destructively interfere. Edge states also occur on the cut ends, and these states result in transmission peaks similar to those observed from the cut ends of carbon nanotubes [70].

At $V = 0.4$ V, the energy of the bottom GNR has been shifted down by 0.4 eV, and the low transmission regions near $E = 0$ and $E = -0.4$ eV are the result of the the small 130 meV bandgaps of the GNR leads. The region in between corresponds to transmission from hole states of the top lead to electron states of the bottom lead. As the bias of the bottom layer is increased to 0.7 V, the dip in transmission near -0.4 eV rigidly shifts down to ~ -0.7 eV, and the transmission from hole states to electron states between 0 and -0.7 eV is strongly suppressed due to the large wavevector mismatch [38, 62] of the states inside the contacts and the bilayer region

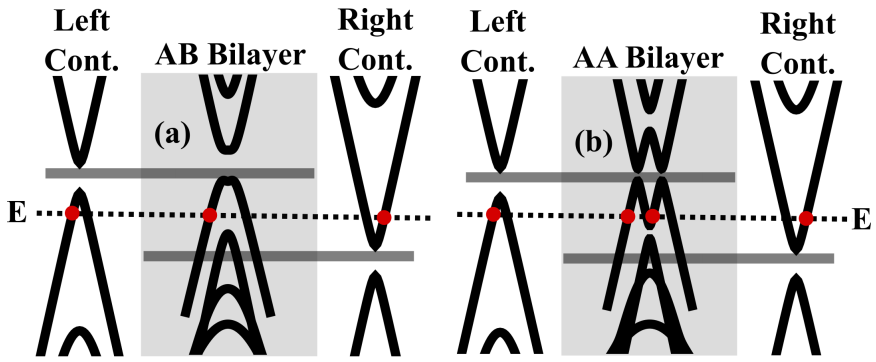

Figure 2.5: Schematic band diagrams of the leads and overlap regions of the (a) AB and (b) AA structures at a bias of 0.4 V. At a given energy, E, the wavevectors of the leads and bilayer region are different due to the shift of bands caused by applied bias. At a given energy between the quasi-Fermi levels of the left and right contacts, the number of right moving states available for carrying current is (a) one in the AB device and (b) two in the AA device.

as illustrated in Fig. 2.5. The resonant feature at ~ 0.3 eV results from an edge state on the cut end of the top GNR.

The coherent current at any bias is proportional to the area under the transmission curve bounded by the Fermi levels of the contacts. Beyond 0.7 V bias, the transmission between the Fermi levels in Fig. 2.4(b) begins to increase as the first excited subbands of the top and bottom GNR leads are pulled into the energy window, and the current begins to increase.

The dependence of transmission of the AA device on bias follows similar trends. However, the peak current is twice as large, and the strong suppression of transmission occurs at approximately twice the bias of the AB device. This can be understood by noting that the wavevector mismatch for the AA case is less, since at any energy, E, between the quasi-Fermi levels of the left and right contacts, the AA bilayer has two states whereas the AB bilayer has only one state for right moving electrons as illustrated in Fig. 2.5. Therefore, more voltage is required to generate the same amount of wavevector mismatch for the AA case. This also explains the doubling

of the magnitude of the peak current for the AA structure compared to that of the AB structure. This is consistent with the fact that there are twice as many nearest-neighbor matrix elements in AA stacking compared to those in AB stacking; i.e. in AA stacking, every atom in the lower GNR is directly below a corresponding atom in the upper GNR, whereas, in AB stacking, every second atom in the lower GNR is directly beneath an atom in the upper GNR.

2.4 Conclusion

In summary, we have performed *ab-initio* DFT, π-bond, and NEGF based calculations to study the $I - V$ characteristics of a bilayer GNR structure where bias is applied between the GNRs by independently contacting each layer. The simulations of the model structures with both AB and AA stacking provide proof-of-principle that NDR can occur in such structures.

Chapter 3

Current Modulation by Voltage Control of the Quantum Phase

A relative rotation of 90 degrees between two graphene nanoribbons (GNRs) creates a crossbar with a nano-scale overlap region. Calculations, based on the first principle density functional theory (DFT) and the non-equilibrium Green's function (NEGF) formalism, show that the electronic states of the individual GNRs of an unbiased crossbar are decoupled from each other similar to the decoupling that occurs in twisted bilayer graphene. Analytical calculations, based on Fermi's Golden Rule, reveal that the decoupling is a consequence of the cancellation of quantum phases of the electronic wavefunctions of the individual GNRs. As a result, the inter-GNR transmission is strongly suppressed over a large energy window. An external bias applied between the GNRs changes the relative phases of the wavefunctions resulting in modulation of the transmission and current by several orders of magnitude. A built-in potential between the two GNRs can lead to a large peak-to-valley current ratio (> 1000) resulting from the strong electronic decoupling of the two GNRs that occurs when they are driven to the same potential. Current switching by voltage control of the quantum phase

in a graphene crossbar structure is a novel switching mechanism. It is robust even with an overlap of ~ 1.8 nm $\times$ 1.8 nm which is well-below the smallest horizontal length scale envisioned in the International Technology Roadmap for Semiconductors (ITRS).

3.1 Introduction

Lack of a bandgap in graphene [15, 18] is one of the challenges for achieving high ON/OFF current ratios in graphene field effect transistors (FETs). The most obvious way to circumvent this problem is to open a bandgap, e.g. by using chemical doping [25], creating nanoribbons [19–21], or by applying a vertical electric field in bilayer graphene [22–24]. However, it is difficult to create a sufficiently large bandgap without degrading the electronic properties of graphene. Another way is to utilize the unique properties of graphene in alternative FET architectures [30, 31, 33, 34]. A highly nonlinear current-voltage relationship can be obtained in a graphene-insulator-graphene p-n junction [35]. Some devices exhibiting negative differential resistance (NDR) have been proposed [1, 36–39]. However, most of these devices have relatively complex architectures [33, 34, 36–38], limited scalability [30], or low on-off or peak-to-valley current ratios [1, 38, 39]. In this work, we unveil a novel current switching mechanism in graphene crossbars in which the current can be modulated by several orders of magnitude. This switching mechanism is based on voltage control of the relative phases of the electronic wavefunctions of two crossed graphene nanoribbons. It does not rely on a bandgap, and it is not based on tunneling through or over a potential barrier. It is relatively independent of temperature. It is robust even when the overlap of the active region is scaled down to ~ 1.8 nm $\times$ 1.8 nm. This length scale is well below any horizontal scale envisioned in the ITRS [73].

Interest in twisted, or misoriented, layers of graphene was recently motivated by the need to understand the electronic properties of multilayer graphene furnace-grown on the C-face of SiC [4]. Experimental analysis showed that the layers tended to be rotated with respect to each other at certain angles corresponding to allowed growth orientations with respect to the SiC substrate [5]. Calculations, based on density functional theory [4, 5, 7, 8], empirical tight binding [40], and continuum [6] models for such rotated bilayers found linear dispersion near the K-points. A recent experiment showed that in twisted bilayer graphene for twist angles greater than $\sim 3^{o}$, the low-energy carriers behave as massless Dirac Fermions with a reduced Fermi velocity compared to that of single layer graphene, and that for twist angles greater than 20^{o}, the layers are effectively decoupled and act as independent layers [9]. A vertical electric field in a twisted bilayer graphene can couple the layers [10] and reduce the Fermi velocity [11]. A recent study of the conductivity between two infinite rotated sheets of graphene found enhanced conductance at commensurate angles with relatively small unit cells and negative differential resistance at small biases [12].

Although the physics of the decoupled layers in twisted bilayer graphene has been studied extensively, it is not clear if these properties still hold in the limit of nanoscaled device dimensions, for example, in the twisted bilayer that occurs in the overlap region of two crossed GNRs fabricated by unzipping two carbon nanotubes [41]. Botello-Méndez et al. very recently addressed this issue performing both DFT and empirical tight binding calculations of the transmission across and through crossed graphene nanoribbons [74]. Crossed armchair - zigzag (AZ) GNRs and crossed zigzag - zigzag GNRs were considered. Most relevant to our work, was their study of crossed AZ GNRs, approximately 5nm wide, aligned in AB stacking at right angles and then rotated. The minimum in the interlayer transmission between the armchair GNR (aGNR) and the zigzag GNR occurred when the angle of intersection was 60^{o}. This

is equivalent to the 90° angle of intersection between two aGNRs which is the system that we consider.

In this work, we analyse the physical mechanism of the inter-layer coupling at the nanoscale and its dependence on the potential difference between the two layers, and we show that it can be exploited for current switching by voltage control of the wavefunction phase.

The model structure shown in Fig. 3.1 consists of two armchair GNRs with one placed on top of the other at right angles forming a GNR crossbar (xGNR). In this case, the overlap region of the xGNR, which is neither AA nor AB stacking, is a twisted bilayer with an area of $\sim$ 1.8 nm $\times$ 1.8 nm and a twist angle of 90°. For two infinite sheets, a 90° rotation is the same as a 30° rotation which is not a commensurate rotation angle. A Moiré pattern can be observed at the intersection of the two nanoribbons in Fig. 3.1.

Calculations, based on *ab initio* density functional theory (DFT) coupled with the non-equilibrium Green's function formalism (NEGF), show that the inter layer decoupling still exists in such a small geometry containing approximately 220 C atoms leading to strong suppression of inter-GNR transmission when the two layers are at the same potential. An analytical model using Fermi's Golden Rule reveals that the suppression of the inter-layer transmission results from the cancellation of the quantum phases of the electronic wavefunctions of the individual GNRs. An external bias applied between the GNRs changes the relative phases of the wavefunctions resulting in modulation of the transmission and current by several orders of magnitude. The decoupling that occurs when the GNRs are at equal potentials can be exploited using a built-in potential similar to the one that occurs in a p-n junction to produce negative differential resistance with a large (> 1000) peak-to-valley current ratio. A large, dense array of crossed graphene nanoribbons, with each cross point providing

a non-linear current-voltage response, could serve in, for example, a cellular neural network [75], a memory array [76], or provide added functionality to standard transistor circuits [77]. The inter-layer potential difference governs the transmission. While in this paper, we consider a two-terminal configuration, one could also control the inter-layer potential with gates, in which case the physics described here could be exploited to implement ultra-scaled transistors.

3.2 Method

In this study, four different types of calculations are performed: (i) geometry optimization, (ii) band structure, and (iii) electron transport. The geometry optimization and band structure calculations are performed using DFT. The electronic transport of the xGNR is calculated using the NEGF formalism coupled with DFT. (iv) The numerical results are explained using analytical expressions for the wavefunctions in a π-orbital basis. The calculation methods and the device structure are discussed below.

3.2.1 Device Structure

The crossbar structure consists of two H-passivated, armchair GNRs shown in Fig. 3.1. In this arrangement, the GNR along the y-axis is placed on top of the GNR along the x-axis with a vertical separation of 3.35 Å in between. Throughout the rest of the paper, the GNRs placed along x- and y-axes will be referred to as the 'bottom' and 'top' GNRs, respectively. Since we are interested in current modulation in the absence of a bandgap, the widths of the GNRs are chosen to be 14-C atomic layers (3n+2) $\sim$ 1.8 nm to minimize the bandgap resulting from the finite width. The bandgap of the 14-aGNR, calculated from DFT code Fireball [58, 59] is 130 meV

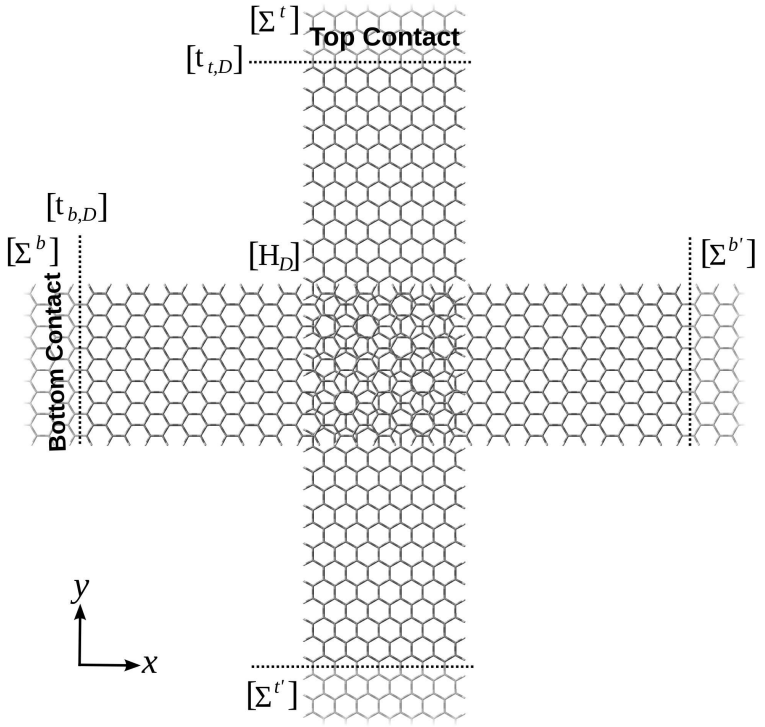

Figure 3.1: Atomistic geometry of the crossbar GNR (xGNR) consisting of two H-passivated, armchair GNRs with one placed on top of the other rotated by 90°. Each GNR is 14-C atomic layers wide ($\sim$ 1.8 nm) with a bandgap of 130 meV. The contacts are modeled by the self–energies of semi-infinite leads. The region bounded by the broken lines is used as a super-cell for the band structure calculations.

which is in good agreement with Son *et al.* [60]. The area of the overlap region of the xGNR is ~ 1.8 nm $\times$ 1.8 nm. The total simulated area between the four ideal leads indicated by the self-energies in Fig. 3.1 is ~ 7 nm $\times$ 7 nm.

The infinite xGNR, shown in Fig. 3.1, is constructed by attaching the the self-energies $\mathbf{\Sigma}^{t}$ and $\mathbf{\Sigma}^{t'}$ to the top GNR and the self-energies $\mathbf{\Sigma}^{b}$ and $\mathbf{\Sigma}^{b'}$ to the bottom GNR. Throughout this article, the semi-infinite leads indicated by the self-energies $\mathbf{\Sigma}^{t}$ and $\mathbf{\Sigma}^{b}$ are termed as top and bottom contacts respectively.

3.2.2 Fireball

The geometry optimization and the calculation of electronic structures are performed with the *ab initio* quantum mechanical molecular dynamics, DFT code Fireball [58,78] using separable, nonlocal Troullier-Martins pseudopotentials [63], the BLYP exchange correlation functional [64,65] and a self-consistent generalization of the Harris-Foulkes energy functional [66–69, 79]. A single zeta (single numeric) sp^3 Fireball basis set is used. These localized pseudoatomic orbitals are slightly excited due to hard wall boundary conditions imposed at radial cutoffs, r_c, for each atomic species. The cutoffs are $r^{1s} = 4.10$ Å for hydrogen and $r^{2s} = 4.4$ Å and $r^{2p} = 4.8$ Å for carbon [70].

3.2.3 Structure Relaxation

In order to construct the crossbar, the geometry of a super-cell of H-passivated single layer aGNR with periodic boundary conditions is optimized using Fireball. The super-cell, which has a length of 8-atomic layers, is repeated using the lattice vector $\vec{a} = 8.77\hat{x}$ (Å). The relaxation is performed until all the Cartesian forces on the atoms are < 0.05 eVÅ^{-1}. In the self-consistent field calculation, a Fermi smearing temperature of 50 K and self-consistent convergence factor of 10^{-7} are used. The

one dimensional Brillouin zone is sampled using 8 k points during optimization. This relaxed single layer super-cell is then repeated to construct longer GNR which, in turn, is used to construct the crossbar. No further relaxation is performed for crossbar.

3.2.4 Band Structure

The region indicated by the broken lines in Fig. 3.1 forms the crossbar super-cell for electronic bandstructure calculations. The super-cell is repeated with lattice vectors $\vec{a_1} = 7.016\hat{x}$ and $\vec{a_2} = 7.016\hat{y}$ (nm). For the self-consistent field calculation, the first Brillouin zone is sampled using a Monkhorst-Pack scheme with a k mesh of 7×7. The electronic structure of the super-cell is calculated with Fireball using the basis, pseudopotentials, functional, Fermi smearing temperature, and convergence factor as described above.

3.2.5 Transport

The Hamiltonian matrix elements used in the NEGF calculation are generated from the Fireball super-cell calculation. The matrix elements include the electron-electron interaction at the DFT/BLYP level of theory in equilibrium. The matrix elements of the external applied potential U are calculated as $\langle i, \alpha | U | j, \beta \rangle = S_{\alpha_i, \beta_j} \left[U(\mathbf{r}_i) + U(\mathbf{r}_j) \right] / 2$ where the indices i and j label the atoms, the indices α and β label the basis orbitals, and S_{α_i, β_j} is the overlap matrix $\langle i, \alpha | j, \beta \rangle$. This approach in which the matrix elements of the external potential have the same form as in an extended Hückel model has been used by others [71]. The approach captures the Stark effect, but not *non-equilibrium* charge self-consistency. The applied bias V is distributed symmetrically between the top and the bottom GNRs such that the electrostatic potential energies are $U(\mathbf{r}_i) = -eV/2$ for atoms on the top GNR and, $U(\mathbf{r}_i) = eV/2$ for atoms on the

bottom GNR.

The matrix elements are used in a recursive Green's function (RGF) algorithm that utilizes non-uniform block layers to calculate the Green's function of the device, $\mathbf{G}^R$, as described in Ref. [70]. The self-energies $\mathbf{\Sigma}^t$ and $\mathbf{\Sigma}^b$ are calculated with the decimation method [80] using a 10 meV broadening factor. The transmission spectrum, $T(E)$, is then calculated from the standard Green's function expression, $T(E) = \mathrm{tr}\left\{\mathbf{\Gamma}^b_{1,1}\mathbf{G}^R_{1,N}\mathbf{\Gamma}^t_{N,N}(\mathbf{G}^R_{1,N})^\dagger\right\}$, where the indices 1 and N indicate the first and last block-layers of the xGNR respectively, $\mathbf{\Gamma}^b_{1,1} = i\left(\mathbf{\Sigma}^b - \mathbf{\Sigma}^{b\dagger}\right)$, and $\mathbf{\Gamma}^t_{N,N} = i\left(\mathbf{\Sigma}^t - \mathbf{\Sigma}^{t\dagger}\right)$. The coherent current is calculated from

$$I = \frac{2e}{\hbar}\int \frac{dE}{2\pi} T(E)\left[f(E-(\mu+eV/2)) - f(E-(\mu-eV/2))\right] \tag{3.1}$$

where $f(E)$ is the Fermi function, and μ is the equilibrium Fermi level. The temperature is 300 K for all current calculations.

3.2.6 Analytical Model

An expression for the current flow between the two GNRs can also be obtained from Fermi's Golden Rule using analytical expressions for the wavefunctions and empirical tight-binding parameters for the matrix elements. The transition rate from a k_x state of mode n in the bottom GNR to a k_y state of mode m in the top GNR is

$$\frac{1}{\tau} = \frac{2\pi}{\hbar}\left|M_{mn}(k_x,k_y)\right|^2 \delta(E_m(k_y) - 2U - E_n(k_x)) \tag{3.2}$$

where $E_i(k)$ is the energy-wavevector relation of an individual GNR for mode i. $U = eV/2$ is the magnitude of the electrostatic potential energies of the individual GNRs. The matrix element M_{mn} is calculated between the k_x state on the bottom

GNR and the k_y state on the top GNR, and the detailed expression is given below in Eq. (3.13). The current is obtained by multiplying Eq. (3.2) with the Fermi factors of the top and bottom contacts $[f(E_n - (\mu + U)) - f(E_m - (\mu - U))]$ and summing over all initial and final states. The sum over k_x and k_y gives the joint density of states of the top and bottom GNR,

$$\sum_{k_x,k_y} \delta(E_m(k_y) - 2U - E_n(k_x)) = \int dE N_{1D}^n(E-U) N_{1D}^m(E+U) \tag{3.3}$$

where N_{1D}^i is the single-spin, 1D density of states for mode i that has the units of (energy^{-1}). The final expression for the current is

$$I = \frac{4\pi e}{\hbar} \sum_{m,n} \int dE \, |M_{mn}|^2 \, N_{1D}^n(E-U) N_{1D}^m(E+U) [f(E-(\mu+U)) - f(E-(\mu-U))] \tag{3.4}$$

which has the same form as the equation for current obtained for 2D twisted bilayer graphene [12]. Comparing Eq. (3.1) with Eq. (3.4) gives the analytical expression for the transmission,

$$T(E) = 4\pi^2 \sum_{m,n} |M_{mn}|^2 \, N_{1D}^n(E-U) N_{1D}^m(E+U). \tag{3.5}$$

The expression for the matrix element M_{mn} can be obtained from the expression for the electronic wavefunction of a single layer aGNR as follows. The energy-wavevector dispersion relationship of band n of an N-atomic layers wide aGNR can be written as [81],

$$E_n(k) = \epsilon + \mathrm{sgn}(n) \left| \tilde{t}_n(k) \right| \tag{3.6}$$

with

$$\tilde{t}_n(k) \equiv \langle \psi_{nkA} | H | \psi_{nkB} \rangle = -t_0 \left[2e^{ika_{cc}/2} \cos(\theta_n) + e^{-ika_{cc}} \right] \tag{3.7}$$

where ϵ is the site energy of the carbon atoms, k is the wave vector, sgn is the signum function, t_0 is the in-plane nearest neighbor hopping parameter, a_{cc} is the C-C bond length, and $\theta_n = \frac{|n|\pi}{N+1}$. The corresponding electronic wavefunction is given by [81],

$$|\psi_{nk}\rangle = \frac{1}{\sqrt{2}}\left(|\psi_{nkA}\rangle + \mathrm{sgn}(n)e^{-i\Theta_{nk}}|\psi_{nkB}\rangle\right) \tag{3.8}$$

with

$$\Theta_{nk} = \angle\tilde{t}_n(k) \tag{3.9}$$

and

$$|\psi_{nk\alpha}\rangle = \sqrt{\frac{2}{N_x(N+1)}}\sum_{p=1}^{N}\sum_{q=1}^{N_x} e^{ikx_q}\sin(\theta_n p)|\alpha_{pq}\rangle \tag{3.10}$$

where $\alpha \in \{A, B\}$ represents the A or B atomic sites, p and q count the atomic layers and the unit cells, respectively, and N_x is the total number of unit cells considered. $|\alpha_{pq}\rangle$ is the p_z orbital of the atomic site α in the unit cell q and atomic layer p of the GNR. The matrix element M_{mn} can be resolved into four components,

$$M_{mn} \equiv \langle\psi_{mk_y}|H_{int}|\psi_{nk_x}\rangle \tag{3.11}$$

$$= M_{mn}^{AA} + M_{mn}^{AB} + M_{mn}^{BA} + M_{mn}^{BB} \tag{3.12}$$

$$= \frac{1}{2}\sum_{\alpha=A,B}\sum_{\beta=A,B} C_{mn}^{\alpha\beta}H_{mn}^{\alpha\beta} \tag{3.13}$$

where

$$C_{mn}^{AA} = 1 \tag{3.14}$$

$$C_{mn}^{AB} = \mathrm{sgn}(n) e^{-i\Theta_{nk_x}} \tag{3.15}$$

$$C_{mn}^{BA} = \mathrm{sgn}(m) e^{i\Theta_{mk_y}} \tag{3.16}$$

$$C_{mn}^{BB} = C_{mn}^{AB} C_{mn}^{BA} = \mathrm{sgn}(nm) e^{i(\Theta_{mk_y} - \Theta_{nk_x})} \tag{3.17}$$

and

$$H_{mn}^{\alpha\beta} \equiv \langle \psi_{mk_y\alpha} | H_{int} | \psi_{nk_x\beta} \rangle \tag{3.18}$$

$$= \frac{2}{\sqrt{N_x N_y}(N+1)} \sum_{p=1}^{N} \sum_{q=1}^{N_y} \sum_{p'=1}^{N} \sum_{q'=1}^{N_x} e^{i(k_x x_{q'} - k_y y_q)} \sin(\theta_m p) \sin(\theta_n p') \langle \alpha_{pq} | H_{int} | \beta_{p'q'} \rangle \tag{3.19}$$

where H_{int} is the inter-GNR interaction, p and q are the indices of the atoms of the top GNR, and p' and q' are the indices of the the atoms of the bottom GNR. The quantity $\langle \alpha_{pq} | H_{int} | \beta_{p'q'} \rangle$ is calculated using the empirical formula [10],

$$\langle \alpha_{pq} | H_{int} | \beta_{p'q'} \rangle = -t_1 e^{-3(d_{pqp'q'} - d_o)} \tag{3.20}$$

where t_1 is the nearest-neighbor inter-layer hopping parameter, $d_{pqp'q'}$ is the distance between the atoms on the top and the bottom GNRs, and d_o is the inter GNR distance. The edge effects were taken into account by replacing $\tilde{t}_n(k)$ in Eq. (3.9) by $\tilde{t}_n(k) + \delta\tilde{t}_n(k)$ where $\delta\tilde{t}_n(k)$ is the correction for the edge bonds following Ref. [81]. While calculating M_{mn}, the site energies of the C atoms of the top and the bottom GNRs are rigidly shifted by $-eV/2$ and $eV/2$, respectively, to include the effects of the external bias voltage V.

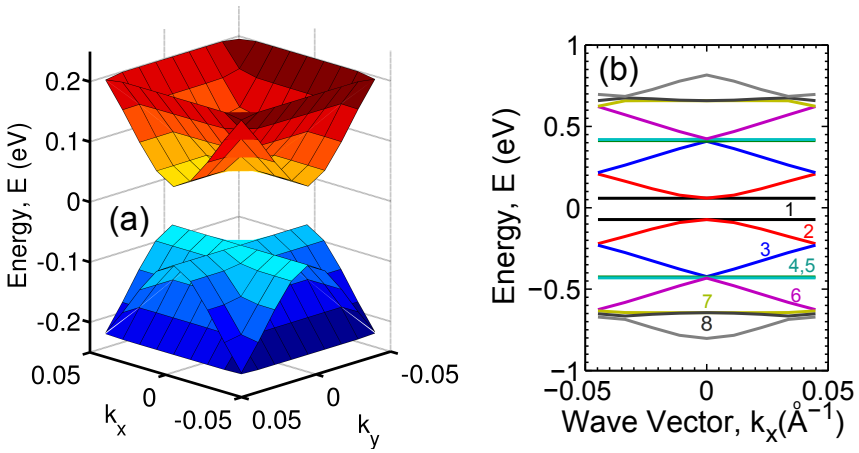

Figure 3.2: (Color Online) Band structure of the xGNR super-cell calculated using Fireball: (a) as a function of k_x and k_y, (b) as a function of k_x only, at $k_y = 0$. The energy $E = 0$ eV is set at the Fermi level. The bands shown in (a) appear as a superposition of bands of two isolated GNRs with one aligned in the x- and the other in y-direction. The bands indicated by 1 and 2 in (b) are degenerate at Γ indicating that they are decoupled.

For all the calculations presented below, the hopping parameters are $t_0 = 3.16$ eV and $t_1 = 0.39$ eV [10]. For the 14 atomic layer aGNR ($N = 14$), the conduction-band sub-band index is $n = 10$, and the valance-band sub-band index is $n = -10$.

3.3 Numerical Results

3.3.1 Band Structure

The bandstructure of the crossbar supercell, calculated as described in Sec. 3.2.4 using the DFT code Fireball, reveals that the low energy states of the top and the bottom GNRs are electronically decoupled. The calculated bandgap of the xGNR is found to be $\sim$ 130 meV, which is equal to the bandgap of a single aGNR. The low energy electronic dispersion of the xGNR as a function of wave vectors k_x and k_y shown in Fig. 3.2(a) appears as a superposition of the band structures of two

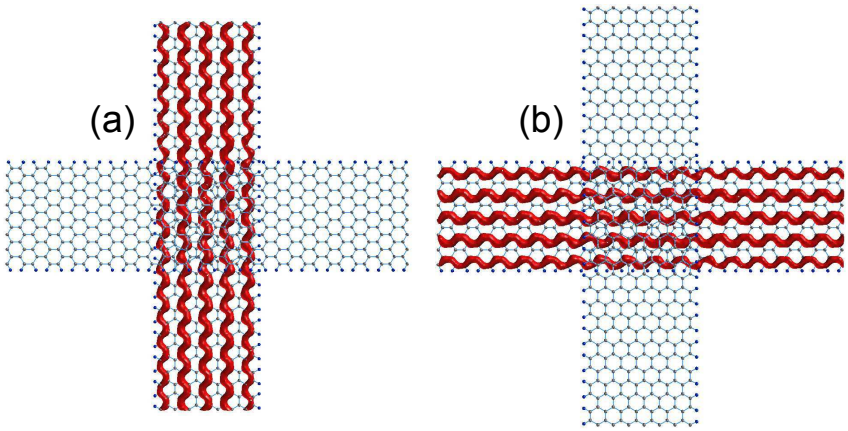

Figure 3.3: (Color Online) Three dimensional iso-surface of the eigenstate corresponding to (a) band 1 and (b) band 2 in Fig. 3.2(b) at Γ. The eigenstate of band 1 is localized on the top GNR, and the eigenstate of band 2 is localized on the bottom GNR.

infinite single aGNRs with one placed along the x-axis and the other along the y-axis. To see this in more detail, the electronic dispersion is plotted as a function of k_x (at $k_y = 0$) in Fig. 3.2(b). The band indicated by 1 in Fig. 3.2(b) does not have any dependence on k_x while band 2 is exactly the same as the valence band of an isolated GNR along the x-axis. These two bands are degenerate at gamma which indicates that they are decoupled from each other. This is confirmed by the 3D contour plots of the population at gamma for bands 1 and 2 shown in Figs. 3.3(a) and (b) respectively. Bands 1 and 2 are entirely localized on the top and bottom GNRs, respectively. Therefore, bands 1 and 2 correspond to the valance bands of the top and bottom GNRs, respectively. The decoupling is also consistent with recent experimental [9] and theoretical [8] studies of twisted bilayer graphene.

Coupling is observed between the fundamental modes and the first excited modes. Bands 3 and 6 in Fig. 3.2(b) are the folded valance bands of the the bottom GNR. Similarly, the bands 4 and 5 are the folded valance bands of the top GNR. Bands 7 and 8 are the first excited bands of the top and bottom GNRs. At these energies,

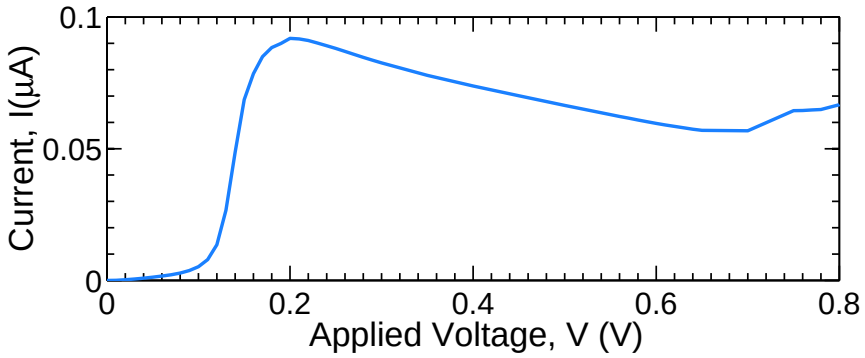

Figure 3.4: Current voltage (I-V) characteristic of the intrinsic xGNR.

splitting is seen at the super-cell Brillouin zone edge. These are the energies where the transmission becomes non-negligible. Similar analysis applies for the first excited conduction bands.

3.3.2 Transport

Intrinsic xGNR

The simulated current voltage (I-V) characteristic of the xGNR corresponding to Fig. 3.1 is shown in Fig. 3.4. Initially, the current increases sharply with the bias, reaches a peak at ~ 0.2 V and then decreases exhibiting NDR. The origin of this non-linear behavior can be understood in terms of the inter-GNR transmission plotted in Fig. 3.5. The transmission in the unbiased xGNR shown in Fig. 3.5(a) is strongly suppressed in a large energy window due to the decoupling of the fundamental modes. The asymmetry in the transmission is consistent with the fact that the electron-hole symmetry is broken in bilayer graphene. The peaks near ± 0.65 eV and ± 0.9 eV are due to the excited sub-bands. When the bias voltage is increased beyond the bandgap, e.g. at $V = 0.15$ V, the transmission within the energy window defined by the chemical potentials of the top and the bottom contacts increases several orders of

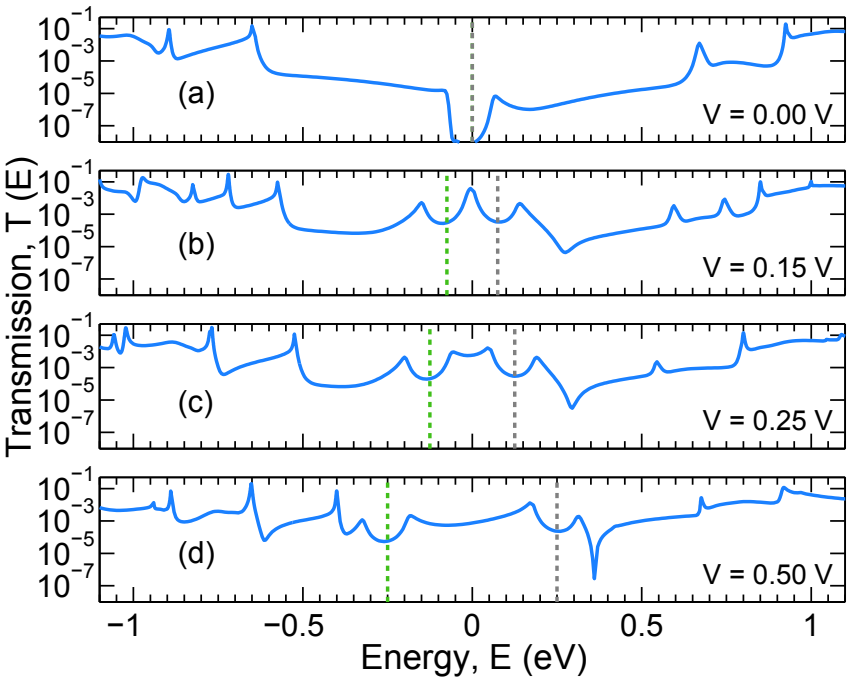

Figure 3.5: (Color Online) Transmission as a function of energy for different bias voltages. The energy $E = 0$ eV is set at the equilibrium Fermi level. The vertical lines represent the chemical potentials of the top and the bottom contacts. The dips in the transmission near the vertical lines correspond to energies lying inside the bandgap of either the top or the bottom GNR. The transmission does not go to zero at these energies as a result of the finite energy broadening used to calculate the surface self-energies of the contacts.

magnitude as shown in Fig. 3.5(b). The transmission between the chemical potentials remains high until $V \sim 0.2$ V, and then it decreases resulting in NDR. The analysis in Sec. 3.4 will show that the dependence of the transmission on the voltage difference between the two GNRs results from voltage control of the relative phases of the top and bottom GNR wavefunctions. The most important point to take away from the transmission plots in Fig. 3.5 is that the transmission is suppressed by several orders of magnitude when the potential difference between the GNRs at the cross point is zero.

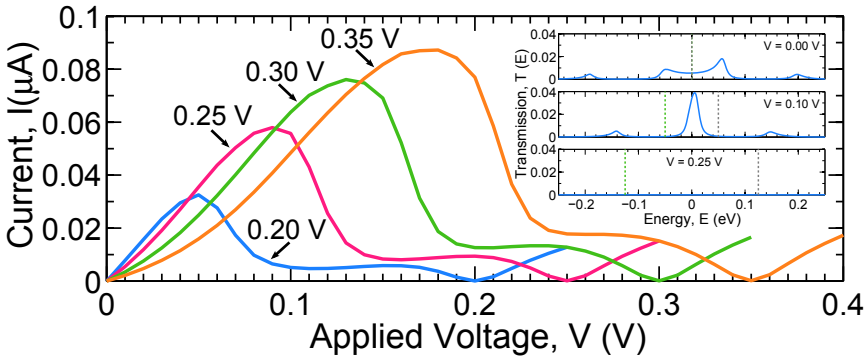

Figure 3.6: (Color Online) Simulated I-V characteristics of xGNR $p-n$ junctions with different built-in potentials. Inset: Transmission of the xGNR $p-n$ junction for $\phi_{bi} = 0.25$ V as a function of energy for different bias voltages. The energy $E = 0$ eV is set at the equilibrium Fermi level. The vertical lines represent the chemical potentials of the top and bottom contacts.

xGNR $p-n$ junction

The strong decoupling of the top and bottom GNR at zero bias can be exploited by creating a built-in potential using either field-effect [82, 83] or chemical [26, 27] doping. For simplicity, we assume that, the built-in potentials of the p-doped top GNR and n-doped bottom GNR are $-\phi_{bi}/2$ and $+\phi_{bi}/2$ respectively, where ϕ_{bi} is the total built in potential. The bias V is symmetrically distributed between the GNRs such that the electrostatic potential energies of the top and the bottom GNR are $U = -e(V - \phi_{bi})/2$ and $U = e(V - \phi_{bi})/2$, respectively, and the potential difference between the GNRs is $\Delta U = e(V - \phi_{bi})$.

In Fig. 3.6, the calculated I-V's through the xGNR are shown for different built in potentials. All of the I-V's show large peak-to-valley current ratios summarized in Table 3.1. The origin of such large peak-to-valley current ratios can be understood by looking at the transmission plots when $\phi_{bi} = 0.25$ V as shown in the inset of Fig. 3.6. The built in potential of 0.25 eV between the two GNRs results in a large transmission coefficient at zero bias. Increasing the bias to $V = 0.10$ V decreases the potential

ϕ_{bi} (V)	V_{peak} (V)	V_{valley} (V)	I_{peak} (nA)	I_{valley} (pA)	I_{peak}/I_{valley}
0.20	0.05	0.20	32.5	34.4	945
0.25	0.09	0.25	57.9	54.8	1057
0.30	0.13	0.30	76.1	82.2	926
0.35	0.18	0.35	87.2	118.4	737

Table 3.1: Calculated peak and valley currents for different built in potentials for xGNR $p-n$ junction.

energy difference ΔU between the GNRs to 0.15 eV and increases the difference of the chemical potentials of the leads to 0.10 V. The current is proportional to the area under the transmission curve between the two chemical potentials. Increasing the bias drives the potential difference ΔU between the two GNRs to zero. At $V = 0.25$ V, the potential difference between the GNRs becomes zero resulting in strong suppression of the transmission over a large energy window and strong suppression of current. Thus, the large peak-to-valley current ratios result from the strong modulation of the transmission with voltage. The physical mechanism governing the voltage dependence of the transmission is analyzed in the next section.

3.4 Analysis

The inter-GNR transmission calculated from the analytical expression given by Eq. (3.5) captures the essential physics of the transmission and its dependence on the potential difference of the two GNRs. The transmission calculated from Eq. (3.5) is plotted in Fig. 3.7 for two different biases with $\phi_{bi} = 0$ corresponding to Figs. 3.4 and 3.5. At $V = 0$ V the transmission is strongly suppressed in the energy range between the edges of the first excited sub-bands which is in agreement with the numerical calculations. The analytical calculations also capture the asymmetry in the transmission and the voltage modulation of the transmission. For example, at

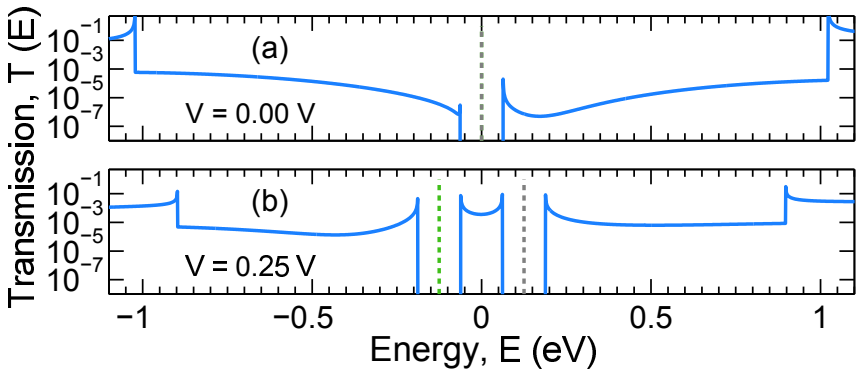

Figure 3.7: (Color Online) Transmission as a function of energy for different bias voltages calculated using Eq. (3.5). The energy $E = 0$ eV is set at the equilibrium Fermi level. The dashed vertical lines represent the chemical potentials of the top and the bottom contacts. The gaps in the transmission near the chemical potentials correspond to energies lying inside the bandgap of either the top or the bottom GNR. Since the analytical calculations include no energy broadening, the transmission is zero at those energies.

0.25 V the transmission inside the energy window bounded by the chemical potentials in Fig. 3.7(b) increases several orders of magnitude. The gaps in the transmission correspond to energies lying inside the bandgap of either the top or the bottom GNR. Since the analytical calculations include no energy broadening, the transmission is zero at those energies.

Although Eq. (3.5) clearly shows that the transmission is proportional to both the magnitude of the matrix element squared and the joint density of states of the two GNRs, the physics governing the transmission at low energies between the fundamental modes is primarily determined by the matrix element. For example, at $V = 0$ V the matrix element squared closely resembles the trend in the transmission at low energies as shown by the black curve in Fig. 3.8(a). The joint 1D density of states peaks at the band edges and, therefore, enhances the transmission at the band edges. Similarly, the matrix element squared at $V = 0.25$ V shown by the black curve in Fig. 3.8(b) captures the main features of the transmission at low energies and

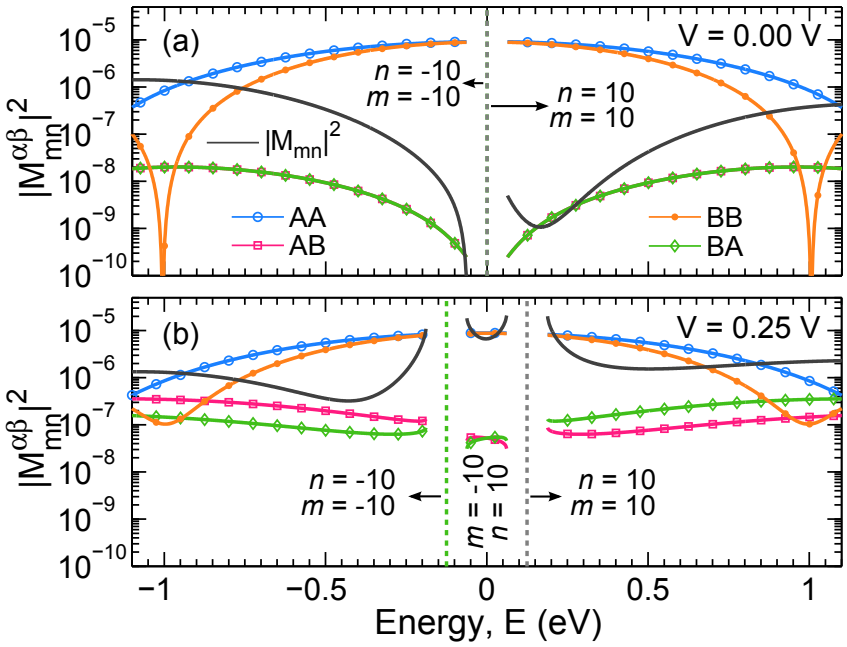

Figure 3.8: (Color Online) Magnitude squared of the matrix element and its four components considering only the fundamental modes. The total matrix element squared and its components are indicated according to the legend in (a). (a) $V = 0$ V. For $E \gtrsim 0$ eV, $m = 10$ and $n = 10$ and for $E \lesssim 0$ eV, $m = -10$ and $n = -10$. (b) $V = 0.25$ V. For $-0.06 < E < 0.06$ eV, $m = -10$ and $n = 10$; for $E < -0.19$ eV, $m = -10$ and $n = -10$; for $E > 0.19$ eV, $m = 10$ and $n = 10$. The AB and BA components are very small at low energies near $E = 0$ compared to the AA and BB components in both cases. The vertical lines represent the chemical potentials of the contacts.

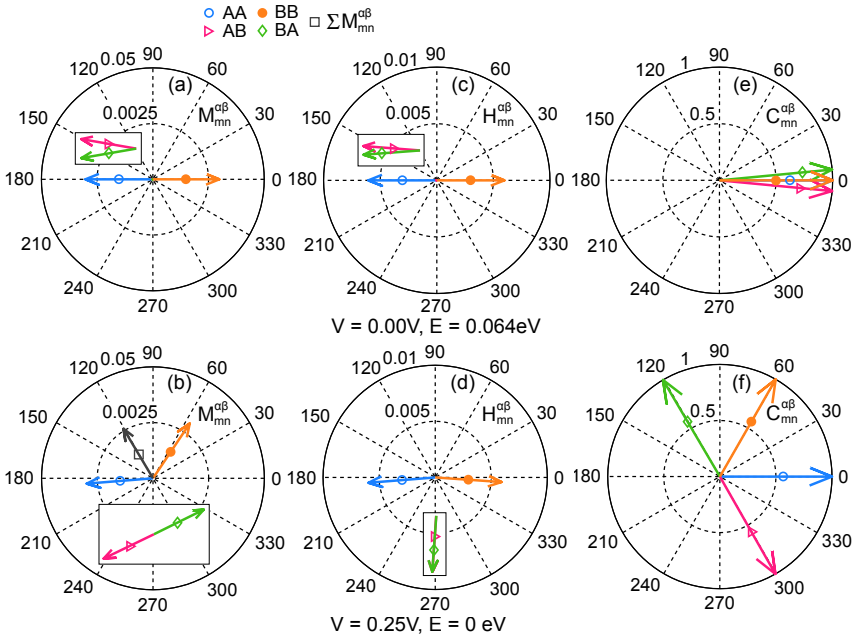

Figure 3.9: (Color Online) Phasor plots of $M^{\alpha\beta}_{mn}$ (a,b), $H^{\alpha\beta}_{mn}$ (c,d), and $C^{\alpha\beta}_{mn}$ (e,f). The AA, BB, AB, and BA components are indicated according to the legend at the top of the figure. (a, c, e) $V = 0$ V and $E = 0.064$ eV (the conduction band edge). (b, d, f) $V = 0.25$ V and $E = 0$ eV. The lengths and the directions of the arrows represent the magnitude and the angle of the corresponding complex quantities, respectively. Since the AB and BA components of H and M are very small, they are magnified several orders of magnitude and shown in the insets.

its enhancement by the applied bias. Hence the matrix element governs the voltage dependence of the transmission, and we shall concentrate only on M_{mn} below. In the discussion below, we shall only consider the fundamental modes and hence drop the subscript of M.

The matrix element consists of four components, $M = M^{AA} + M^{AB} + M^{BA} + M^{BB}$ as given by Eq. (3.12). These four components plotted in Fig. 3.8 are labeled as 'AA', 'BB', 'AB' and 'BA.' At low energies, $M \approx M^{AA} + M^{BB}$ since M^{AA} and M^{BB} are orders of magnitude larger than M^{AB} and M^{BA} for all bias voltages.

The cancellation of the phases of M^{AA} and M^{BB} suppresses the matrix element and hence the transmission at $V = 0$ V. This can be understood by looking at the

phasor diagram, Fig. 3.9(a), where the matrix element and its four components are shown in polar coordinates at the conduction band edge. The magnitude of M is very small since $|M^{AA}| \approx |M^{BB}|$ and $\angle M^{AA} - \angle M^{BB} \approx 180^{\text{o}}$.

The applied bias does not change $|M^{AA}|$ and $|M^{BB}|$, but it modulates the phase difference between these components which, in turn, results in a significant change in the magnitude of the total matrix element, M. For example, at $V = 0.25$ V, the magnitudes of M^{AA} and M^{BB} shown in Fig. 3.8(b) remain unchanged. Although $|M^{AB}|$ and $|M^{BA}|$ increase by an order of magnitude, they are still several orders of magnitude smaller compared to $|M^{AA}|$ and $|M^{BB}|$ and hence insignificant. The applied bias changes $\angle M^{BB}$ by $\sim 60^{\text{o}}$ while leaving $\angle M^{AA}$ almost unchanged as shown in Fig. 3.9(b). Thus, a bias voltage of 0.25 V changes the phase difference, $\angle M^{AA} - \angle M^{BB}$ from 180^{o} to $\sim 120^{\text{o}}$. As a consequence, the total matrix element $M \approx M^{AA} + M^{BB}$ and the resulting transmission increase by several orders of magnitude.

The voltage modulation of the phases of the major components $M^{\alpha\alpha} = \frac{1}{2} C^{\alpha\alpha} H^{\alpha\alpha}$ is controlled by the voltage dependent quantum phase factors $C^{\alpha\alpha}$ defined by Eqs. (3.14) and (3.17) . Figs. 3.9(c) and (d) clearly show that the phases of H^{BB} and H^{AA} are only slightly modified by the bias. On the other hand, it is clear from Figs. 3.9(e) and (f) that the bias changes the phase of C^{BB} by $\sim 60^{\text{o}}$. The phase of C^{AA} remains unchanged for all energies and for all biases due to the particular construction of the wavefunction given by Eq. (3.8). Thus, the voltage dependency of the quantum phases are lumped into the quantity C^{BB}.

The asymmetry in transmission at zero bias results from the phase factors C^{AB} and C^{BA} and the small difference between $|M^{AA}|$ and $|M^{BB}|$. At the conduction band edge, $n = 10$ and hence $\angle C^{AB} = \angle \text{sgn}(n) e^{-i\Theta_{nk_x}} = -\Theta_{nk_x}$ where Θ_{nk_x} is a small angle. At the valance band edge, $n = -10$ and hence $\angle C^{AB} = \angle \text{sgn}(n) e^{-i\Theta_{nk_x}} = 180^{\text{o}} - \Theta_{nk_x}$. Thus, $\angle C^{AB}$ and hence $\angle M^{AB}$ at the conduction and valence band

edges differ by 180°. The same is true for the phase of C^{BA} and M^{BA}. The sum of M^{AB} and M^{BA} adds to M^{AA} at the conduction band edge as shown in Fig. 3.9(a), and the sum adds to M^{BB} at the valence band edge. $|M^{AA}|$ is slightly larger than $|M^{BB}|$. At the valence band edge, the addition of $(M^{AB} + M^{BA})$ to M^{BB} gives a better cancellation with M^{AA} resulting in the matrix element minimum shown in Fig. 3.8(a). At the conduction band edge, the addition of $(M^{AB} + M^{BA})$ to M^{AA} reduces the cancellation with M^{BB} resulting in a larger total matrix element and increased transmission.

In a preliminary study of the sensitivity of the transport properties to the detailed geometry of the overlap region we have considered four variations of the xGNR shown in Fig. 3.1: the x and the y coordinates of the top GNR are shifted by (a) $a_{cc}/2$ and (b) $3a_{cc}/2$, (c) the width of both arms are increased to 4.5 nm (38 atomic C layers), and (d) the width of the top GNR is increased to 20 C atoms so that the xGNR consists of a 14-aGNR and a 20-aGNR. Calculations, based on the model presented in Sec. 3.2.6, show that the transport properties of all of these xGNRs are similar to that of the crossbar shown in Fig. 3.1. The I-V characteristics of these xGNRs with the biasing scheme described in Sec. 3.3.2 are all similar to the I-V's shown in Fig. 3.6. The peak-to-valley current ratios for the (a), (b), (c), and (d) configurations at $\phi_{bi} = 0.25$ V are ~ 100, ~ 1000, ~ 150, and ~ 120, respectively.

3.5 Conclusions

We have performed *ab-initio* DFT and NEGF based calculations to study the inter-layer coupling and transport properties of nanometer scale twisted bilayer graphene that occurs in the overlap region of a crossbar consisting of two GNRs with one placed on top of the other at right angles. The GNRs in the crossbar are electronically decou-

pled from each other similar to the decoupling that occurs in twisted bilayer graphene. An analytical model based on Fermi's Golden Rule reveals that the decoupling is a consequence of the cancellation of quantum phases of the electronic states of the individual GNRs. This leads to strong suppression of the inter-GNR transmission when the two GNRs are at the same potential. A potential difference between the GNRs changes the relative phases of the top and bottom wavefunctions and destroys the phase cancellation resulting in strong coupling and high transmission. Thus, the transmission can be modulated several orders of magnitude by controlling the quantum phase using an external bias. A built-in potential between the two GNRs can lead to large peak-to-valley current ratios (> 1000) resulting from the strong electronic decoupling of the two GNRs that occurs when they are driven to the same potential. Current switching by voltage control of the quantum phase in graphene crossbar structure is a novel switching mechanism. It is robust even with an overlap of ~ 1.8 nm $\times 1.8$ nm containing only ~ 220 C atoms which is well-below the smallest horizontal length scale envisioned in the ITRS.

Chapter 4

Multi-State Current Switching by Voltage Controlled Coupling

The interlayer transport between two semi-infinite crossed graphene nanoribbons (GNRs) is governed by the quantum interference between the standing waves of the individual GNRs. An external bias applied between the GNRs controls the wavelength and hence the relative phase of these standing waves. Sweeping the applied bias results in multiple constructive and destructive interference conditions. The oscillatory nature of the voltage controlled interference gives rise to an oscillatory current-voltage (I-V) response with multiple negative differential resistance (NDR) regions. The period of oscillation is inversely proportional to the length of the finite ends of the GNRs. Quantum interference is explicitly shown to be the physical mechanism controlling the interlayer current by direct evaluation of the interlayer matrix element using analytical expressions for the wavefunctions.

4.1 Introduction

One remarkable property of graphene is that the individual layers in misoriented or twisted bilayer graphene (TBG) are electronically decoupled [4–9, 40, 50, 51, 53]. The decoupling results from the destructive quantum interference between the electron wave functions of the top and bottom graphene layers [8]. Between two misoriented sheets of graphene, the coherent interlayer resistance has been found to vary between 8 to 16 orders of magnitude as the rotation angle is varied between 0 and 30 degrees [3, 12]. Contact resistances resulting from the coherent coupling between two rotated graphene layers have been calculated to vary between $\sim 10^7$ Ωcm^2 and $\sim 10^{-9}$ Ωcm^2 as a function of the rotation angle [12]. The interlayer coupling is increased [10] and the Fermi velocity is reduced [11] in presence of a vertical electric field, and negative differential conductance is predicted at small biases [12]. Since the coherent interlayer coupling can be so small, the interlayer, room-temperature conductance for all but the smallest misorientation angles is dominated by phonon-assisted transport mediated by an out-of-plane beating mode of the bilayer with phonon energies ranging from 10 meV to 30 meV as the misorientation angle varies from zero to 30 degrees [3].

The coherent electronic decoupling between two-dimensional (2D) misoriented bilayers is still present in lower dimensions when the overlap region is reduced to the nanometer scale [2]. The crystallographic misorientation angle of two overlapping armchair nanoribbons placed at a 90° angle with respect to each other is 30°. The coherent interlayer transmission between two crossed, 1.8 nm, armchair, graphene nanoribbons was suppressed by 5 orders of magnitude. Applying a 0.15 V voltage between the nanoribbons increased the transmission by 4 orders of magnitude [2]. The GNR crossbar in Ref. [2] consisted of two *infinite* nanoribbons in which the electron states were *propagating* waves.

This work investigates the electronic coupling between two *semi-infinite* armchair GNRs in which the electron states are standing waves. Despite the equivalence of the atomistic geometry of the overlap regions, the inter-layer transport properties of the crossed infinite GNRs (IxGNR) and the crossed semi-infinite GNRs (SxGNR) differ due to the difference of the electronic wavefunctions. Unlike the current-voltage response of the IxGNR, sweeping a two-terminal voltage applied between the two crossed semi-infinite GNRs results in an oscillatory current-voltage (I-V) characteristic with multiple NDR regions. Since the vibrational modes of such structures have not yet been calculated, only the coherent inter-layer current will be considered. Estimates of the relative magnitudes of the coherent current and the phonon-assisted current will be given at the end.

The occurrence of transmission resonances and antiresonances in single layer graphene structures is not uncommon [84–91]. Such structures would display many features in the *low-bias conductance* as a function of gate voltage. In contrast, the individual features in the transmission spectra of the rotated graphene nanoribbons are not of primary importance. The *average magnitude* of the transmission and the dependence of the average magnitude on the applied *two terminal* voltage are of primary interest. Sweeping an external two-terminal bias applied between the GNRs alters the relative phases of the two standing waves resulting in a periodic modulation of the *average* interlayer transmission and an oscillatory I-V characteristic with multiple NDR regions. The voltage period of oscillation is inversely proportional to the length of the truncated ends of the GNRs.

A GNR device with oscillatory I-V characteristics and multiple NDR regions is complementary to numerous graphene field effect transistors [32–34, 92–94]. Such a non-linear I-V response can provide increased functional density in all-carbon based electronics [76, 77, 95].

4.2 Method

Three different types of calculations are performed. (i) The geometry of the graphene nanoribbons are optimized using density functional theory (DFT). (ii) The electronic transport is calculated using the non-equilibrium Green's function (NEGF) formalism. The Hamiltonian matrix elements used in the NEGF calculations are generated using the extended Hückel theory (EHT). (iii) The physics governing the electron transport is explained by direct evaluation of the interlayer matrix element using analytical expressions for the wavefunctions.

4.2.1 Device Structure and Transport

The structure, as shown in Fig. 4.1, consists of two overlapping, semi-infinite, armchair GNRs. Each GNR has one truncated end with a zigzag edge. To minimize the bandgap resulting from the finite width, the number of atoms across the width of the GNRs is chosen to be $N_w = 3p + 2$ where p is an integer. The analysis is carried out for $N_w = 14$ with a calculated bandgap of 136 meV. Different and unequal widths are also numerically simulated. The GNRs are H-passivated, and their structure is relaxed using a projector augmented wave method within the framework of the Perdew-Burke-Ernzerhof type generalized gradient approximation of the density functional theory as implemented in the software package VASP [96]. The relaxed GNRs are placed one above the other with a vertical separation of 3.35 Å to create the crossbar, and no further relaxation is performed. The top and bottom contacts are modeled as infinite leads using self-energies $\mathbf{\Sigma}^t$ and $\mathbf{\Sigma}^b$ on the top GNR (tGNR) and the bottom GNR (bGNR), respectively as shown in Fig. 4.1. An external bias V is applied between the tGNR and the bGNR such that the electrostatic potential energies are $U(\mathbf{r}) = -eV/2$ for atoms on the tGNR and, $U(\mathbf{r}) = eV/2$ for atoms on

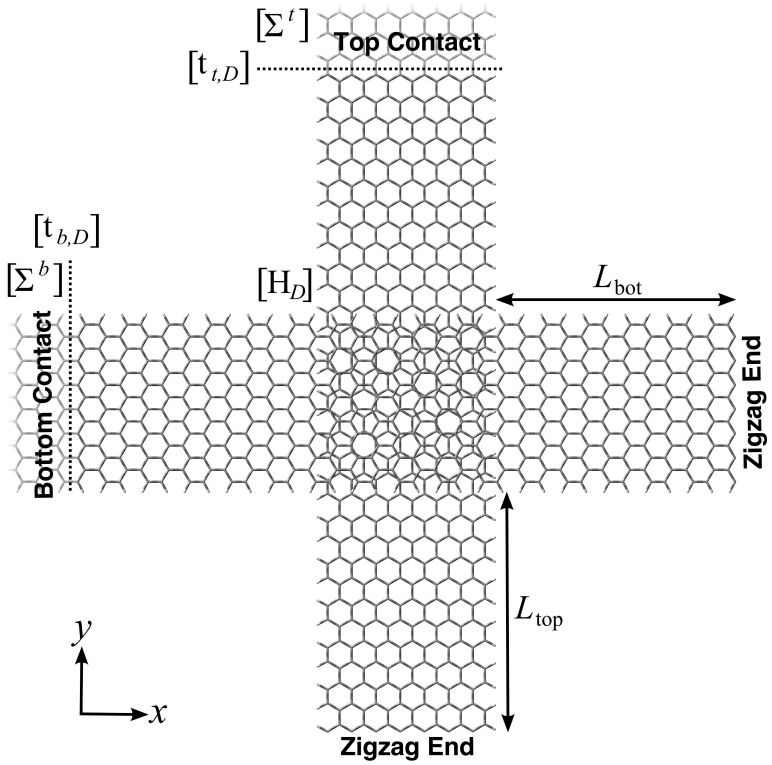

Figure 4.1: The structure consists of two crossed semi-infinite, armchair nanoribbons. To minimize the bandgap due to quantization, the number of atoms across the width is chosen to be $3p + 2$ where p is an integer. The length of the top and bottom truncated ends are L_{top} and L_{bot}, respectively. The coordinate system is chosen such that the origin is at the center of the overlap region.

the bGNR. The Hamiltonian matrix elements used in the NEGF calculation are generated from the EHT using non-orthogonal Slater-type orbitals. The EHT graphene parameters are taken from Ref. [97]. The Hamiltonian matrix elements are used in the NEGF algorithm to calculate the transmission coefficient, $T(E)$, as described in Ref. [2]. The current is calculated from

$$I = \frac{2e}{\hbar} \int \frac{dE}{2\pi} T(E) \left[f_b(E) \; - \; f_t(E) \right] \tag{4.1}$$

where $f_b(E)$ and $f_t(E)$ are the Fermi distributions of the bGNR and tGNR contacts respectively. In all current calculations, the temperature of the Fermi distributions is 300 K.

4.2.2 Analytical Model

The analytical expression for the inter-layer transmission obtained using Fermi's Golden Rule is given by [2],

$$T(E) = 4\pi^2 \sum_{m,n} |M_{m,n}|^2 \, N_n(E - eV/2) N_m(E + eV/2). \tag{4.2}$$

where the subscripts m and n index a mode on the top and bottom GNR, respectively, $N_m(E)$ and $N_n(E)$ are the corresponding single-spin density of states, and $M_{m,n} = \langle \psi_{mk_y} | H_{int} | \psi_{nk_x} \rangle$ is the matrix element between the states on the top and bottom GNRs. Here, $|\psi_{mk_y}\rangle$ is the injected state at the top contact, and $|\psi_{nk_x}\rangle$ is the collected state at the bottom contact. Both states are at energy E. Since the low energy transport of the SxGNR is governed by the fundamental modes, we will only consider the wavefunctions of the conduction and valance bands and drop the subscripts of M below.

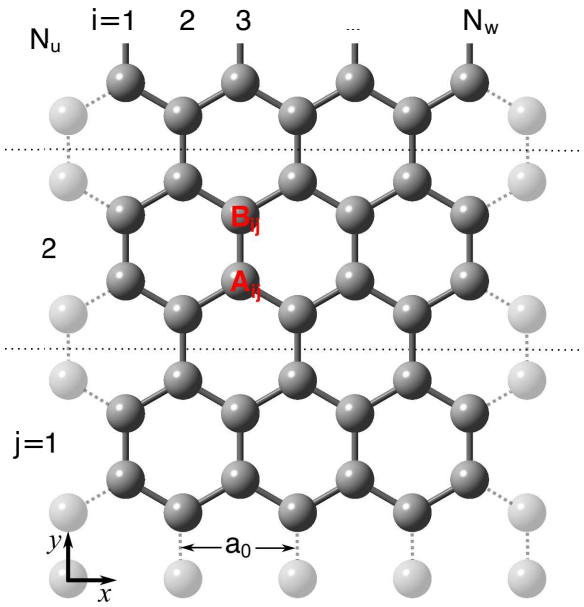

Figure 4.2: (Color Online) Atomistic geometry of the model semi-infinite armchair graphene nanoribbon (aGNR) with a zigzag end. The origin of the coordinate system is placed on the atom at the bottom left corner. The edge-atoms removed from the GNR are shown in gray. The envelope function is zero at those positions. For the analytical calculations presented in Sec. 4.4, the GNR width $N_w = 14$.

Within the framework of the continuum model, the wavefunction of mode n of the semi-infinite armchair graphene nanoribbon (aGNR) shown in Fig. 4.2 can be written as [98, 99],

$$|\psi_{nk_y}\rangle = |\psi_{nk_yA}\rangle + |\psi_{nk_yB}\rangle \tag{4.3}$$

with

$$|\psi_{nk_y\alpha}\rangle = \sum_{\mathbf{R}_\alpha} \left(\mathrm{e}^{\mathrm{i}\mathbf{K}.\mathbf{R}_\alpha} \psi_{n\alpha} - \mathrm{e}^{\mathrm{i}\mathbf{K}'.\mathbf{R}_\alpha} \psi'_{n\alpha} \right) |\alpha_{\mathbf{R}_\alpha}\rangle \tag{4.4}$$

where $|\alpha_{\mathbf{R}_\alpha}\rangle$ is the p_z orbital of the carbon atom located at $\mathbf{R}_\alpha$ with $\alpha \in \{A, B\}$ and, $\psi_{n\alpha}$ and $\psi'_{n\alpha}$ are envelope wave functions at $K \equiv (-4\pi/3a_0, 0)$ and $K' \equiv (4\pi/3a_0, 0)$ valleys, respectively. The envelope wave functions of π-electrons can be written as a four component spinor [98, 99],

$$\begin{bmatrix} \psi_{nA} \\ \psi_{nB} \\ -\psi'_{nA} \\ -\psi'_{nB} \end{bmatrix} = C_1 \begin{bmatrix} \sin(k_y y_{_A}) \mathrm{e}^{\mathrm{i}k_{nx} x_{_A}} \\ \frac{s}{k_n} \left(-k_{nx} \sin(k_y y_{_B}) \mathrm{e}^{\mathrm{i}k_{nx} x_{_B}} + k_y \cos(k_y y_{_B}) \mathrm{e}^{\mathrm{i}k_{nx} x_{_B}} \right) \\ -\sin(k_y y_{_A}) \mathrm{e}^{-\mathrm{i}k_{nx} x_{_A}} \\ \frac{s}{k_n} \left(k_{nx} \sin(k_y y_{_B}) \mathrm{e}^{-\mathrm{i}k_{nx} x_{_B}} - k_y \cos(k_y y_{_B}) \mathrm{e}^{-\mathrm{i}k_{nx} x_{_B}} \right) \end{bmatrix} \tag{4.5}$$

with

$$k_n = \sqrt{k_{nx}^2 + k_y^2} \tag{4.6}$$

where $s = +1$ and -1 for the conduction and valance bands, respectively. The quantized wavevector k_{nx} is given by,

$$k_{nx} = \tilde{k}_{nx} - \frac{4\pi}{3a_0} \tag{4.7}$$

where, $n = 0, \pm 1, \pm 2, \ldots$ and $\tilde{k}_{nx} = \frac{2n\pi}{(N_w+1)a_0}$. The dispersion relationship of the

electron associated with the wavefunction in Eq. (4.3) is

$$E_n(k_y) = s\gamma k_n = s\hbar v k_n \tag{4.8}$$

where $\gamma = \frac{\sqrt{3}a_0 t_0}{2} = \hbar v$, $t_0 = 2.7$ eV is the nearest neighbor tight binding parameter [100] and v is the velocity of electron near the Dirac point of graphene. One difference between the wavefunction of a semi-infinite aGNR given by Eq. (4.5) and the wavefunction of a graphene quantum dot (GQD) derived in Ref. [98] is that in a GQD, k_y is discrete due to the fourth hard-wall boundary imposed on the GQD.

For a $N_w = 3p + 2$ atomic layer wide metallic aGNRs, the band index for the conduction and valance band is given by $n = 2(p + 1)$. Hence, $k_{nx} = 0$ and the dispersion relationship for these bands is linear,

$$E_n(k_y) = s\gamma k_y = s\hbar v k_y. \tag{4.9}$$

The corresponding wavefunction components obtained from Eqs. (4.4), (4.5) and (4.6) are given by,

$$|\psi_{nk_y\alpha}\rangle = C \sum_{i}^{N_w} \sum_{j}^{N_u} \phi_{k_y\alpha}(j) \sin(\tilde{k}_{nx} x_{\alpha_i}) |\alpha_{ij}\rangle \tag{4.10}$$

where the envelope wavefunctions along y,

$$\phi_{k_y A}(j) = \sin(k_y y_{A_j}) \tag{4.11}$$

and

$$\phi_{k_y B}(j) = s \cos(k_y y_{B_j}) \tag{4.12}$$

are standing waves. Here, the normalization constant $C = \sqrt{(\frac{2}{(N_w+1)N_u})}$, $\tilde{k}_{nx} = \frac{2\pi}{3a_0}$ and $|\alpha_{ij}\rangle$ is the p_z orbital of the atomic site α in the atomic layer i and the unit cell j of the aGNR.

This continuum model does not take into account the reduced C-C bond length at the armchair edges and therefore $N_w = 3p + 2$ atomic layer wide aGNRs do not show any bandgap. Also, this model does not include the edge state localized at the zigzag edge of the truncated end. Although it does not include the bandgap and the edge states, in section 4.4, we will show that this model captures the essential physics governing the quantum transport in the SxGNR. The missing transmission features corresponding to the bandgap and the edge states do not affect the conclusions drawn by this continuum description.

The coordinate system of the SxGNR shown in Fig. 4.1 is chosen such that the origin is located at the center of the overlap region. The top and bottom stubs are equal in length i.e., $L_{bot} = L_{top} \equiv L$. In this coordinate system, the envelope wavefunctions along y for the fundamental modes of the tGNR are

$$\phi_{k_yA}(j) \quad = \quad \sin k_y(y_{A_j} + L_s) \tag{4.13}$$

and

$$\phi_{k_yB}(j) \quad = \quad s\cos k_y(y_{B_j} + L_s) \tag{4.14}$$

where the stub length L_s is measured from the origin i. e., $L_s = L + W/2$. Here, W is the width of the GNRs. Similarly, the envelope wavefunctions for the fundamental

modes of the bGNR are obtained by replacing y with $-x$ in Eqs. (4.13) and (4.14),

$$\phi_{k_x A}(j) = -\sin k_x(x_{A_j} - L_s) \tag{4.15}$$

$$\phi_{k_x B}(j) = s\cos k_x(x_{B_j} - L_s). \tag{4.16}$$

For the fundamental modes, the quantized wavevectors for the tGNR and the bGNR are equal i. e., $q_n \equiv \tilde{k}_{nx} = \tilde{k}_{ny}$.

The matrix element M between a k_y state of the tGNR and a k_x state of the bGNR can be resolved into four components

$$M = M_{AA} + M_{AB} + M_{BA} + M_{BB} \tag{4.17}$$

where the subscripts indicate the A or B atom of each primitive unit cell. The matrix elements are given by

$$M_{\alpha\beta} \equiv \langle\psi_{k_y\alpha}|H_{int}|\psi_{k_x\beta}\rangle \tag{4.18}$$

$$= C^2 \sum_{i,j,i',j'} \phi_{k_y\alpha}(j)\phi_{k_x\beta}(j')\sin(q_n x_{\alpha_i})\sin(q_n y_{\beta_{i'}})t_{ij,i'j'} \tag{4.19}$$

where i, j and i', j' are the indices of the atoms on the top and the bottom GNRs, respectively. The inter-layer matrix elements between the π-orbitals are obtained following Ref. [10] with $t_{ij,i'j'} = -t_1 e^{-3(d_{ij,i'j'}-d_o)}$ where $d_{ij,i'j'}$ is the distance between the atom on the top layer at site (i,j) and the atom on the bottom layer at site (i',j'), and d_o is the distance between the two layers (3.35 Å). The inter-layer parameter $t_1 = 0.36$ eV [100].

Since the site energies of the top and bottom GNRs are shifted by $+eV/2$, and

$-eV/2$, respectively, the wavevectors for the top and bottom GNRs are given by

$$k_y = \frac{1}{s\gamma}(E + \frac{eV}{2}) \tag{4.20}$$

and

$$k_x = \frac{1}{s\gamma}(E - \frac{eV}{2}) \tag{4.21}$$

respectively. Hence, the external bias can be used to control the relative phase of the envelope wavefunctions inside the overlap region. In section 4.4, we show that this voltage controlled phase determines the nature of the interference between the standing waves of the tGNR and bGNR.

4.3 Numerical Results

The inter layer current in the SxGNR, calculated using the NEGF and EHT formalism, is an oscillatory function of the applied bias with multiple NDR regions as shown in Fig. 4.3. The period of oscillations are 0.5 V, 0.35 V, 0.27 V and 0.18 V for SxGNRs with stub lengths 2.5 nm, 4.2 nm, 5.9 nm and 9.3 nm respectively. Using an analytical model we show below that the period of oscillation is inversely proportional to the stub length.

The inter-GNR transmission plots for stub length $L = 4.2$ nm at the current minima and maxima are shown in Fig. 4.4. At zero bias the transmission shown in Fig. 4.4(a) is strongly suppressed within -0.25 eV $< E < 0.5$ eV due to the destructive interference between the standing waves of the top and bottom GNR states as explained in section 4.4 below. The dip in the transmission near $E = 0$ eV is due to the 136 meV bandgap of the top and bottom GNRs. The narrow peak in the transmission at $E = 0$ eV results from the edge states localized at the zigzag

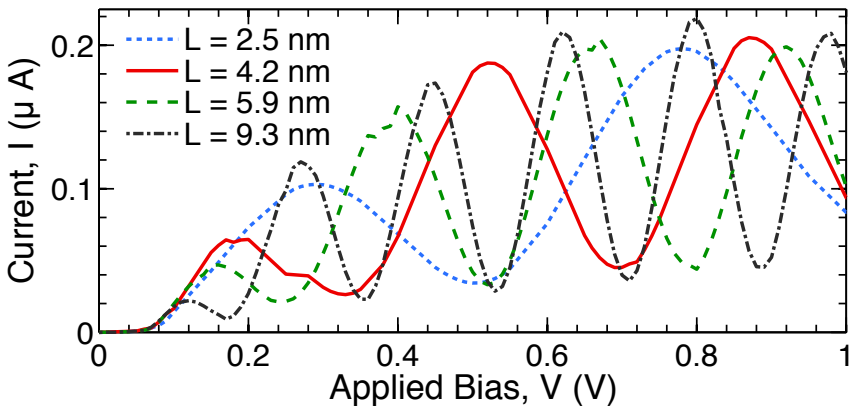

Figure 4.3: (Color online) Current voltage (I-V) characteristics of a symmetric SxGNR with different stub-lengths as shown in the legend.

edges of the top and the bottom GNRs [101].

When the bias is increased to 0.2 V, the transmission increases by five orders of magnitude as shown in Fig. 4.4(b) and the current reaches its first maximum. The transmission peaks at $E = -0.1$ eV and $E = 0.1$ eV are due to the edge states of the top and the bottom GNR, respectively. This is confirmed by the three dimensional contours of the local density of states shown in Fig. 4.5. The states at $E = -0.1$ eV and $E = 0.1$ eV are localized at the zigzag edges of the top and the bottom GNR, respectively.

To understand the contribution of the edge states to the total current we have plotted the cumulative current in Fig. 4.4. The expression of cumulative current is, $I_{cum}(E) = \frac{2e}{\hbar}\int_{-\infty}^{E}\frac{dE'}{2\pi}T(E')\,[f_b(E') - f_t(E')]$ where f_b and f_t are the Fermi distributions at the bottom and the top contacts, respectively. At $V = 0.2$ V the majority of the current is transferred through the evanescent edge states at $E = \pm 0.1$ eV as indicated by I_{cum} in Fig. 4.4(b). However, at $V = 0.52$ V and $V = 0.88$ V all of the states within the Fermi window contribute to the current as shown in Figs. 4.4(d) and (f), respectively. It is found that up to the first current minimum the I-V is

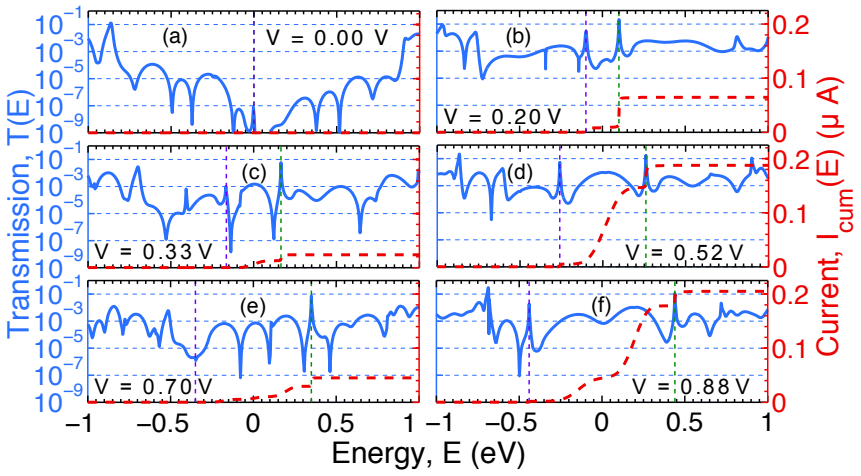

Figure 4.4: (Color online) Transmission (solid line) and the cumulative current (dashed line) as functions of energy for $L = 4.2$ nm at the current minima and maxima. The vertical lines represent chemical potentials of the top and the bottom contacts.

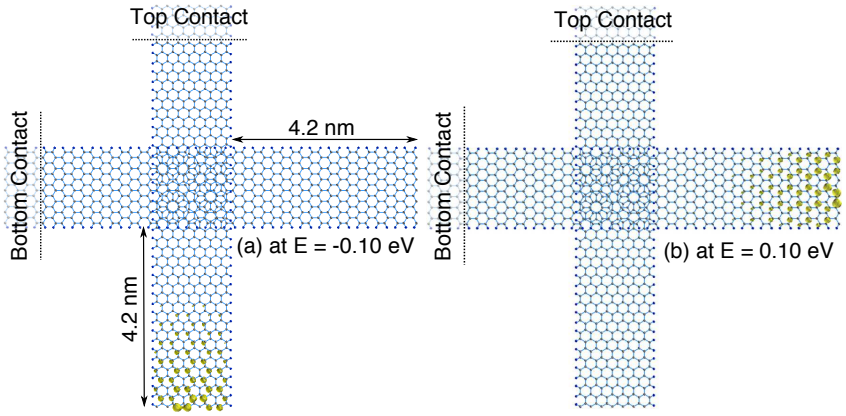

Figure 4.5: (Color online) Three dimensional contour plots of local density of states (LDOS) for $V = 0.2$ V and $L = 4.2$ nm at (a) $E = -0.1$ eV and (b) $E = 0.1$ eV.

governed by the interference between the edge state and the standing wave. Since the edge state decays exponentially inside the GNR, the matrix element between the edge state of one GNR and the standing wave of the other GNR decreases with increasing stub length. This explains the lowering of the first peak in the I-V with increasing stub length.

At $V = 0.33$ V and 0.7 V, the transmission decreases due to the destructive interference between the standing waves of the tGNR and the bGNR and the current minima appear in the I-V. In Sec. 4.4, we will show that with increasing bias the successive appearance of the constructive and destructive interference leads to successive enhancement and suppression of the interlayer transmission, and hence the current oscillates.

To determine if the current-voltage response was qualitatively the same for variations of the symmetric geometry shown in Fig. 4.1, we carried out a preliminary study of three asymmetric structures: (a) $L_{bot} = 2.5$ nm, $L_{top} = 4.2$ nm, $N_w = 14$, (b) $L_{bot} = \infty$, $L_{top} = 4.2$ nm, $N_w = 14$, and (c) $N_w = 20$ (14) for the top (bottom) GNR with $L_{top} = L_{bot} = 4.2$ nm. The current-voltage responses remain similar to those shown in Fig. 4.3. The periods of oscillation for the (a), (b) and (c) configurations are 0.4 V, 0.44 V and 0.36 V respectively. For the (b) configuration with one infinite GNR, the first current peak becomes smaller due to absence of one of the edge states.

To determine how a built-in potential difference between the top and bottom GNRs affects the current-voltage response, we simulated the same four structures as in Fig. (4.3) with a built-in potential difference of 0.25 V. A forward bias drives the potential difference between the two GNRs to zero. When the potential difference is zero, the transmission is reduced several orders of magnitude as shown in Fig. (4.4)(a). At this bias (0.25 V), the current is reduced by several orders of magnitude. The current-voltage curves of the 4 structures with a built-in voltage of 0.25 V are

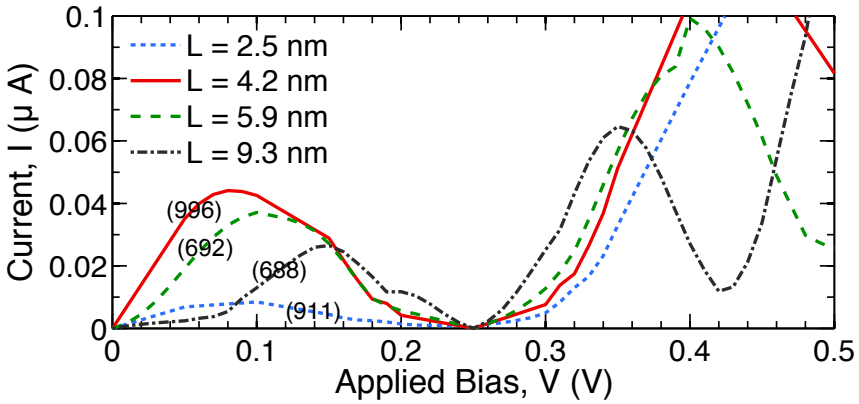

Figure 4.6: (Color Online) Simulated I-V characteristics of SxGNR p-n junctions with built-in potential, $\phi_{bi} = 0.25$ V for different stub lengths. The numbers inside the parentheses represent the peak-to-valley current ratios.

shown in Fig. (4.6). The current ratio of the first current peak to the current minimum at 0.25 V is given in parenthesis for each curve. Because of the large reduction in transmission when the GNRs are drive to equal potentials, peak-to-valley ratios of approximately three orders of magnitude are observed.

4.4 Analysis

Analysis based on Fermi's Golden Rule and analytical expressions for the wavefunctions reveals the physics of the inter-GNR transport. The transmission is governed by both the matrix element squared and the density of states as shown in Eq. (4.2). The transmission calculated numerically with NEGF and the matrix element squared calculated from the analytical expressions for the wavefunctions are plotted in Fig. 4.7(a-b). A comparison of the plots shows that the energy dependence of the transmission and the overall change in magnitude with bias are determined by the matrix element. The mismatch between $T(E)$ and $|M(E)|^2$ near $E = 0$ eV in Fig. 4.7(a) is due to the fact that the bandgap and the edge state are not included in the analytical

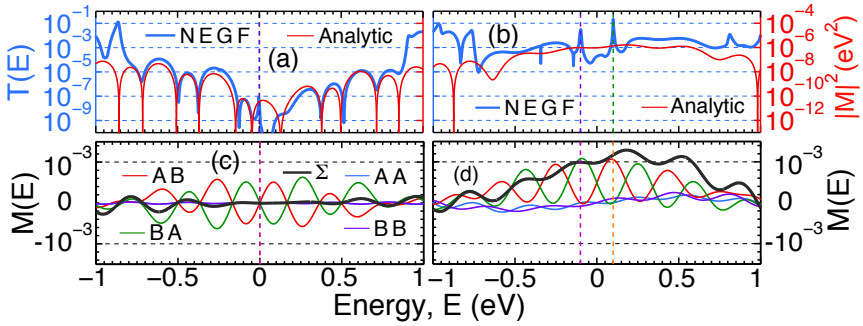

Figure 4.7: (Color online) Transmission $T(E)$ (thick line) and matrix element $|M(E)|^2$ (thin line) at (a) $V = 0$ V and (b) $V = 0.2$ V. Four components of matrix element $M = M_{AA} + M_{AB} + M_{BA} + M_{BB}$ labeled as AA, AB, BA, and BB at (c) $V = 0$ V and (d) $V = 0.2$ V. The black thick line shows the sum of the four matrix elements, M.

model. Outside of that 136 meV range, the energy dependence of $T(E)$ follows closely that of $|M(E)|^2$. Similarly, the matrix element squared at $V = 0.2$ V shown in Fig. 4.7(b) captures the enhancement of the transmission at low energies by the applied bias. The peaks in the $T(E)$ plot at $E = \pm V/2$ are due to the edge states and are not reproduced in the $|M(E)|^2$ plot. Overall, the matrix element governs the voltage dependence of the transmission, and we shall concentrate only on M below.

The four components of the matrix element given by Eqs. (4.17) and (4.19) are plotted in Figs. 4.7(c-d). The total matrix element, M, is well approximated by the sum of M_{AB} and M_{BA}, since these two matrix elements are orders of magnitude larger than either M_{AA} or M_{BB}. At $V = 0$ V, M_{AB} and M_{BA} are approximately equal in magnitude but 180° out of phase as shown in Fig. 4.7(c). Thus the destructive interference between the AB and the BA components of M suppresses the total matrix element and hence the transmission.

When the bias is increased to 0.2 V, the quantum phases of the standing electron waves are modulated by the bias and M_{AB} and M_{BA} acquire a non-zero average value as shown in Fig. 4.7(d). As a result, the AB and BA components do not cancel.

The nature of the voltage controlled quantum interference can be understood by looking at the envelope wavefunctions in the long wavelength limit. At low energies when the wavelength $\lambda >> W$, the variation of the envelope function inside the overlap region is negligible i.e., $\phi_{k_yA}(j) = \sin k_y(y_{A_j} + L_s) \approx \sin(k_y L_s)$. Using the dispersion relationship given by Eq. (4.20) we get

$$\phi_{k_yA}(j) \approx \sin \frac{L_s}{\gamma}(E + eV/2). \tag{4.22}$$

Similarly, for the B sites of bGNR,

$$\phi_{k_xB}(j) \approx s \cos \frac{L_s}{\gamma}(E - eV/2). \tag{4.23}$$

Using Eqs. (4.19), (4.22) and (4.23) we get the expression for M_{AB} in the long wavelength limit,

$$M_{AB} \approx \frac{1}{2}\left(\sin \frac{2L_sE}{\gamma} + \sin \frac{L_seV}{\gamma}\right) H_{AB}. \tag{4.24}$$

Similarly,

$$M_{BA} \approx \frac{1}{2}\left(\sin \frac{2L_sE}{\gamma} - \sin \frac{L_seV}{\gamma}\right) H_{BA}. \tag{4.25}$$

Here, the quantity $H_{\alpha\beta}$ is the energy independent part of $M_{\alpha\beta}$ that depends on the atomic positions of the α atoms of the tGNR and the β atoms of the bGNR,

$$H_{\alpha\beta} = C^2 \sum_{i,j,i',j'} \sin(q_n x_{\alpha_i}) \sin(q_n y_{\beta_{i'}}) t_{iji'j'}. \tag{4.26}$$

Numerical calculations show that

$$H_{BA} = -H_{AB}. \tag{4.27}$$

The quantity, H_{AB} (H_{BA}) is the weighted sum of the interlayer hopping parameter between all the A (B) atoms of the tGNR and all the B (A) atoms of the bGNR weighted by the transverse sine functions of $|\psi_{nk_yA(B)}\rangle$ and $|\psi_{nk_xB(A)}\rangle$. Thus, they are sums over different matrix elements and are not Hermitian conjugates.

Using relation (4.27) in Eqs. (4.24) and (4.25) we get the final expressions for M_{AB} and M_{BA},

$$M_{AB} \approx \frac{1}{2}\left(\sin\frac{2L_sE}{\gamma} + \sin\frac{L_seV}{\gamma}\right)H_{AB} \tag{4.28}$$

$$M_{BA} \approx \frac{1}{2}\left(-\sin\frac{2L_sE}{\gamma} + \sin\frac{L_seV}{\gamma}\right)H_{AB}. \tag{4.29}$$

Eqs. (4.28) and (4.29) clearly show that at $V = n\frac{\pi\gamma}{eL_s}$ where $n = 0, 1, 2, ...$, the AB and the BA components of the matrix element cancel each other as indicated in Fig. 4.7(c). Thus the voltage controlled destructive interference between the A and the B atoms results in suppression of transmission and current minima. Similarly, at $V = (2m+1)\frac{\pi\gamma}{2eL_s}$ where $m = 0, 1, 2, \ldots$, the A and B atoms interfere constructively giving rise to enhancement in transmission and current maxima. Thus the voltage controlled interference between the tGNR and the bGNR is an oscillatory function of the bias which results in an oscillatory current voltage response with multiple NDR regions. The period of the oscillation is inversely proportional to the stub length,

$$V_p = \frac{\pi\gamma}{eL_s}. \tag{4.30}$$

The periods of the oscillations in the current-voltage responses calculated using Eq. (4.30) are 0.52 V, 0.35 V, 0.26 V and 0.18 V for the SxGNRs with 2.5 nm, 4.2 nm, 5.9 nm and 9.3 nm stub lengths, respectively, which closely match with the numerical results calculated using NEGF.

With an understanding of the magnitude of the coherent current, we can compare it to an estimate of the magnitude of the phonon assisted current. Since the phonon modes of the structures under consideration are not known, we estimate an order-of-magnitude of the phonon-assisted current from the phonon-assisted conductivity G_{ph} of 2D misoriented graphene. In 2D misoriented graphene, G_{ph} is a smoothly decreasing function of the rotation angle. At low temperature (T = 20 K) and finite bias, $V > 0.1$ V, the inter-layer conductance lies between 10^{-9} S/nm^2 and 10^{-8} S/nm^2 [3]. The overlap region of the crossbar in Fig. 4.3 is 3.24 nm^2. Choosing a one volt bias, the maximum estimate of the phonon-assisted current would be 32.4 nA. The coherent current shown in Fig. 4.3 is on the order of 100 nA. Thus, from this crude estimate, the current oscillations in the coherent current should still be observable in the presence of phonon-assisted current.

4.5 Conclusions

The inter-layer transport between two crossed, semi-infinite armchair GNRs is governed by voltage controlled quantum interference between the standing waves of the individual GNRs. An external bias applied between the GNRs controls the wavelength and hence the relative phases of these standing waves. Sweeping the applied two-terminal bias causes multiple constructive and destructive interference conditions resulting in a periodic modulation of the average transmission and an oscillatory I-V characteristic with multiple NDR regions. The voltage period of the oscillation is inversely proportional to the length of the truncated ends of the GNRs. An estimate of the magnitude of the phonon-assisted current based on the 2D phonon-assisted conductivity indicates that the oscillations in the coherent current will not be masked by the phonon-assisted current.

Chapter 5

The Interlayer Resistance of a Misoriented, Rotated Interface in Vertically Stacked Graphene

The coherent, interlayer resistance of a misoriented, rotated interface in vertically stacked graphene is determined for a variety of misorientation angles. These values are compared with previously calculated values for the phonon-mediated, interlayer resistance of misoriented, bilayer graphene. The fundamentally limiting quantum-resistance of the ideal interface with $\theta = 0^{\text{o}}$ is on the order of 10^{-3} $\Omega\mu\text{m}^2$. For small rotations, the coherent interlayer resistance is a strong function of the Fermi energy, and it exponentially approaches the ideal quantum resistance at energies away from the charge neutral point. At room temperature, the total interlayer resistance can still be sensitive to the rotation angle changing one to two orders of magnitude as the angle changes by a few degrees. Over a range of intermediate angles, the coherent resistance is much larger than the phonon-mediated resistance which results in a relatively constant total resistance on the order of 100 $\Omega\mu\text{m}^2$.

5.1 Introduction

There is rapidly growing interest in vertically stacked van der Waals materials for electronic device applications [33, 42–47]. In such structures the interfaces between different materials will, in general, be misoriented with respect to each other [48]. THz cutoff frequencies have been predicted for such devices [46]. At such high frequencies, any small series resistance can degrade performance. For example, an emitter contact resistance of 2.5 $\Omega\mu\text{m}^2$ is required to achieve a THz cutoff frequency in a heterostructure bipolar transistor [49]. Understanding the effect of the misorientation on the interlayer resistance is required to fully understand the design requirements and performance of proposed vertically stacked devices.

The most well studied and well understood van der Waals material is graphene [17, 48]. The effect of misorientation on the electronic structure of bilayer graphene has been studied extensively both theoretically and experimentally [4–9, 40, 50–52]. After a few degrees misorientation, the in-plane dispersion becomes linear, and after about 10 degrees misorientation, the in-plane velocity is the same as that of single-layer graphene. Thus, misoriented graphene bilayers act as if they are electronically decoupled.

The study of the interlayer resistance in misoriented bilayer graphene has received far less attention [3, 12, 53]. Bistritzer and MacDonald used a transfer Hamiltonian approach to calculate the coherent interlayer resistance as a function of rotation angle θ and found it to vary by 16 orders of magnitude as the misorientation angle varies from zero degree to 30 degrees [12]. The calculated coherent interlayer resistance values vary from approximately 10^{15} $\Omega\mu\text{m}^2$ to 0.1 $\Omega\mu\text{m}^2$ as a function of rotation angle. Furthermore, the variation with θ is highly non-monotonic, varying many orders of magnitude as θ changes by a few degrees. Our calculations show that the

resistance determined by this approach is inversely proportional to Γ, so that changing the lifetime broadening from 75 meV to 10 meV increases the resistance by an order of magnitude. Thus, the quantitative values of the interlayer resistance cannot be determined from this approach without knowing the actual values of the lifetime broadening Γ. What is independent of Γ is the extreme sensitivity of the coherent interlayer resistance to the rotation angle and the many-order-of-magnitude variation in resistance values as the misorientation angle is varied from zero to 30 degrees.

The room-temperature, phonon-mediated interlayer resistance shows far less dependence on the misorientation angle [3, 53]. It changes by less than an order of magnitude as the angle varies from zero to 30 degrees [3,53]. The room-temperature, phonon-mediated interlayer resistance is a smooth, monotonic function of the misorientation angle. Perebeinos et al. [3] calculated that it varied from about 50 $\Omega\mu\text{m}^2$ at $\theta = 3^\circ$ to 330 $\Omega\mu\text{m}^2$ at $\theta = 30^\circ$. Experimental measurements found approximately an order of magnitude larger resistance that varied from 750 $\Omega\mu\text{m}^2$ to 3400 $\Omega\mu\text{m}^2$ as the angle varied from 5° to 24° [53, 102].

To first order, the resistance from the coherent channel (R_c), and the resistance from the phonon-mediated channel (R_p) are in parallel [54, 55]. Thus, to determine the total inter-layer resistance between two misoriented graphene layers, one requires quantitative values for the coherent component of the resistance. In this work, we provide those values. We do so, by considering two stacks of AB graphite that are rotated with respect to each other at their interface. In such a structure, injection is well defined using the usual non-equilibrium Green function approach; a lifetime broadening factor is not required; and the resistance can be calculated for $\theta = 0^\text{o}$ providing a minimum baseline value. Furthermore, this type of structure is consistent with the proposed vertically stacked van der Waals structures. Combining our values for R_c with the values calculated previously for R_p, we obtain estimates for the total

room-temperature interlayer resistance for a variety of commensurate misorientation angles.

Interest in vertically stacked structures returns us to the many investigations of the c-axis resistance of graphite [103–107] in a more modern, controlled, and scaled context [108]. Ono [105] developed a theory of electron scattering from stacking faults and applied it to faults of the type $\cdots ABABACAC\cdots$ and $\cdots ABABCBCB\cdots$. This theory was enhanced, and, with a few empirical parameters such as the average distance between stacking faults and the transmission probability through a stacking fault, it fit the experimental data over a wide temperature range [107]. The experimental measurements of the c-axis resistivity have been performed through stacks of kish graphite or HOPG with a random ensemble of stacking faults and in the diffusive limit. There is considerable spread in the experimental data. We cannot, at this time, compare our calculations with results from the older body of work [103–107]. Our focus is on the rotated interfaces that naturally occur with the new mechanical stacking methods [48].

5.2 Model

5.2.1 Exact Model

The twisted bilayer graphene (TBG) supercell (i.e. the primitive cell of the commensurate twisted bilayer) is created following the method described in Ref. [40]. The top layer of the TBG supercell is used to create an AB stacked bilayer graphene supercell which, in turn, is used to create the top contact. Similarly, the bottom contact is created using the bottom layer of the TBG supercell. Thus, the twisted structure consists of two AB oriented stacks that are rotated with respect to each other as

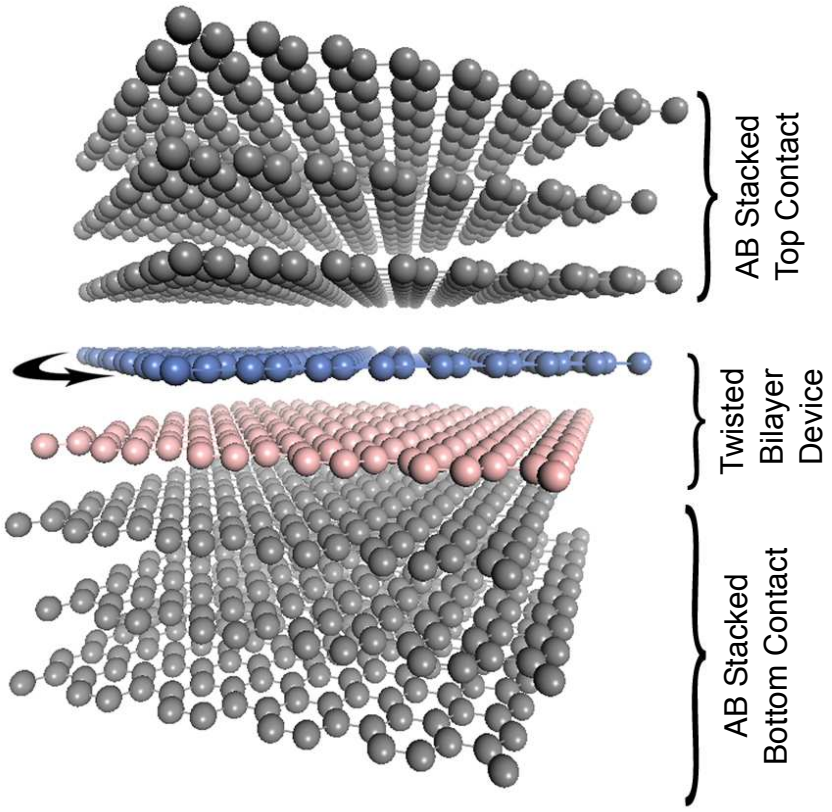

Figure 5.1: Atomistic geometry of the rotated interface. It consists of two AB oriented stacks that are rotated with respect to each other. The interface layers where the misorientation occurs have been colored for visualization. The two misoriented layers are the 'device' in the NEGF calculation.

shown in Fig. 5.1.

The inter layer coherent transport through the twisted structure is modeled using the non-equilibrium Green function (NEGF) formalism with an empirical tight binding Hamiltonian. The coherent resistance is calculated using

$$R = 1/\left[2\frac{\mathrm{e}^2}{\hbar}\int \frac{dE}{2\pi}\, T(E)\left(-\frac{\partial f}{\partial E}\right)\right] \tag{5.1}$$

where $f(E)$ is the Fermi function. The transmission $T(E)$ is given by

$$T(E) = \int_{1^{\mathrm{st}}\mathrm{BZ}} d\mathbf{k}\; T(E,\mathbf{k}) \tag{5.2}$$

where $\mathbf{k}$ is 2D wave vector in the TBG Brillouin zone and $T(E,\mathbf{k})$ is the wavevector resolved transmission calculated using NEGF. To exploit the symmetry, we sample one third of first Brillouin zone indicated by the rhombus $\Gamma K_1 K_2 K_3$ in Fig. 5.4. The rhombus is sampled using equally spaced ($\delta k = 0.005$ Å^{-1}) k-points. For a TBG supercell with $\theta = 21.7868^{\mathrm{o}}$, there are $\sim$ 17000 k-points for each energy. The transmission at each k-point is calculated using the standard Green function expression,

$$T(E,\mathbf{k}) = \mathrm{tr}\left\{\Gamma^b G_D^R \Gamma^t G_D^{R\,\dagger}\right\} \tag{5.3}$$

where $\Gamma^b = i\left(\Sigma^b(E,\mathbf{k}) - \Sigma^{b\dagger}(E,\mathbf{k})\right)$, $\Gamma^t = i\left(\Sigma^t(E,\mathbf{k}) - \Sigma^{t\dagger}(E,\mathbf{k})\right)$ and $\Sigma^b(E,\mathbf{k})$ and $\Sigma^t(E,\mathbf{k})$ are the self-energies of the bottom and the top contacts, respectively. The structure is partitioned such that the 'device' consists of the misoriented bilayer at the center of Fig. 5.1. The surface Green functions of the top and bottom AB stacks are calculated using the decimation algorithm [80] with a convergence factor of 1 meV, and the self energies are calculated from the surface Green functions in the

usual way [109]. The Green function of the twisted bilayer device is given by

$$G_D^R = \left[E\mathrm{I} - H_D(\mathbf{k}) - \Sigma^b(E,\mathbf{k}) - \Sigma^t(E,\mathbf{k})\right]^{-1} \tag{5.4}$$

where $H_D(\mathbf{k})$ is the Hamiltonian matrix of the twisted bilayer in the p_z orbital basis.

The Hamiltonian matrix elements of the twisted bilayer, the top contact and the bottom contact are generated using an empirical tight binding model with an in-pane first nearest neighbor hopping element of $t = 3.16$ eV [17]. The model developed by Perebeinos et al. is used for the out-of-plane coupling [3]. The out-of-plane coupling between atom i in top layer and atom j in the bottom layer is calculated using [3]

$$t_{ij} = t_\perp \exp\left(-\frac{r_{ij} - d_\perp}{\lambda_z}\right) \exp\left[-\left(\frac{r_{ij}^{xy}}{\lambda_{xy}}\right)^\alpha\right] \tag{5.5}$$

where the inter layer distance $d_\perp = 3.35$ Å, the inter layer AB hopping parameter $t_\perp = 0.39$ eV, r_{ij} is the distance between atom i and atom j, the in-plane distance $r_{ij}^{xy} = [(x_i - x_j)^2 + (y_i - y_j)^2]^{1/2}$, $\lambda_{xy} = 1.7$ Å, $\lambda_z = 0.6$ Å and $\alpha = 1.65$. This model is known to reproduce the LDA results for twisted bilayer graphene [3].

5.2.2 Perturbative Model

In the model used by Bistritzer and MacDonald in Ref. [12] for calculating the interlayer transport between two weakly coupled misoriented layers of graphene, the interlayer coupling is treated as a small perturbation between perfect 2D electron gases. In this section, we describe a similar formalism.

The schematic diagram of the device structure used in this formalism is shown in Fig. 5.2. It consists of two misoriented graphene layers. The misoriented bilayer supercell is created following the method described in Ref. [40]. Assuming the inter

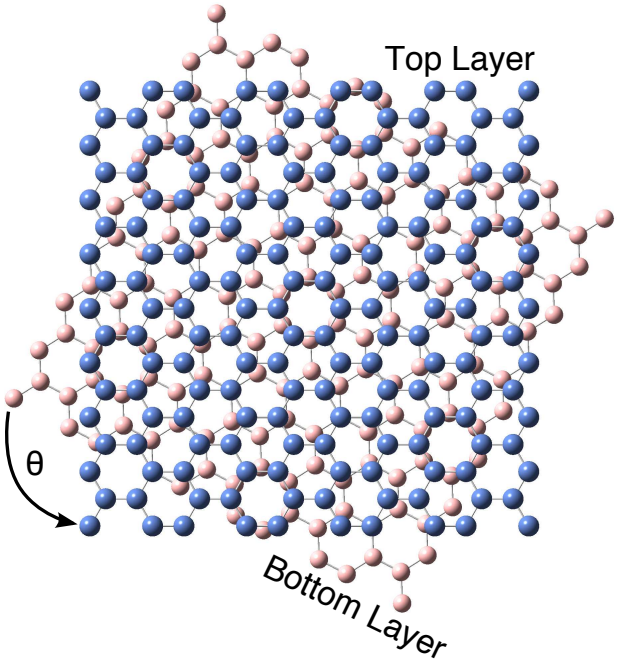

Figure 5.2: Atomistic geometry of the rotated bilayer structure used in perturbative calculations. The atoms on the top and the bottom layers have been colored for visualization.

layer coupling between the misoriented layers as a small perturbation, the wavevector resolved interlayer transmission $T(E, \mathbf{k})$ is given by,

$$T(E, \mathbf{k}) = \mathrm{tr}\left\{t_{10}(\mathbf{k}) a_{00}(E, \mathbf{k}) t_{01}(\mathbf{k}) a_{11}(E, \mathbf{k})\right\} \tag{5.6}$$

where the $t_{ij}(\mathbf{k})$ is the inter layer coupling between layer i and layer j and $a_{ii}(E, \mathbf{k}) = i[g_{ii}(E, \mathbf{k}) - g_{ii}^{\dagger}(E, \mathbf{k})]$ is the unperturbed spectral function of layer i. The unperturbed Green function of layer i is

$$g_{ii}(E, \mathbf{k}) = \left[E\mathrm{I} - H_{ii}(\mathbf{k}) + i\eta\right]^{-1} \tag{5.7}$$

where η is the energy broadening which limits the lifetime of Bloch state in each layer and $H_{ii}(\mathbf{k})$ is the Hamiltonian matrix of layer i in the p_z orbital basis. The total

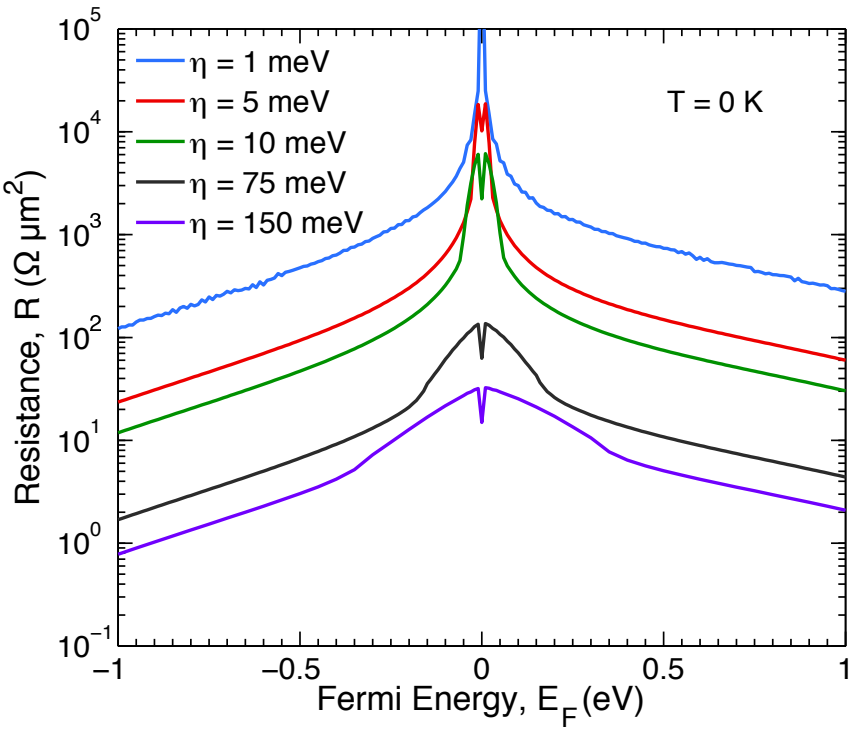

Figure 5.3: Zero temperature coherent contact resistance of twisted bilayer graphene as a function of Fermi Energy calculated using Eq. (5.6) for different energy broadening for $\theta = 21.8^{\circ}$.

transmission $T(E)$ and resistance R is then calculated using Eq. (5.2) and (5.1), respectively.

This formalism is similar to the formalism used by Bistritzer and MacDonald in Ref. [12]. It is very fast because it does not require the self-energy calculations. However, the transmission $T(E)$ calculated using this method depends strongly on the energy broadening factor η as we will show bellow.

5.3 Results and Discussion

The interlayer coherent resistance between two misoriented layers of graphene for different broadening factor η calculated using the perturbative method described in

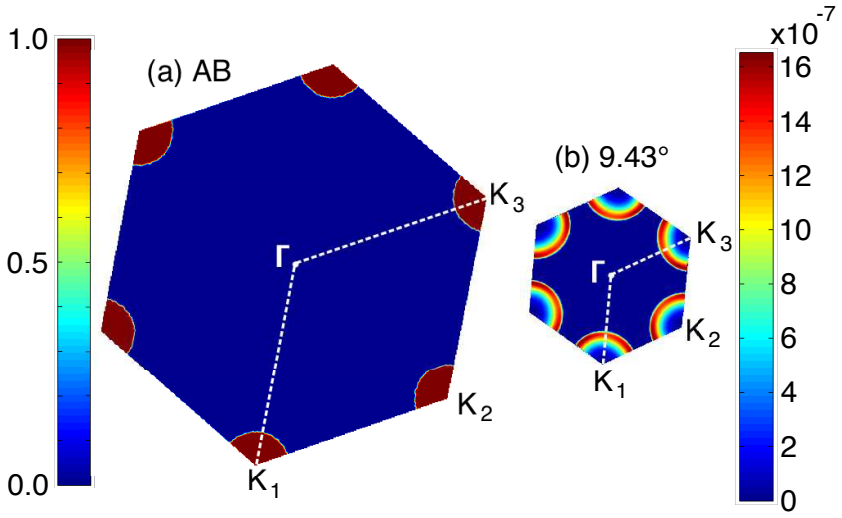

Figure 5.4: Wavevector resolved transmission $T(E, \mathbf{k})$ in the first Brillouin zone at $E = 0.5$ eV for (a) perfect AB stacking calculated using the 21.8° supercell, and (b) a misoriented structure with $\theta = 9.43°$. To exploit the symmetry, the rhombus $\Gamma K_1 K_2 K_3$ is sampled by equally spaced k-points.

Sec. 5.2.2 is shown in Fig. 5.3. The resistance varies inversely with η exhibiting a strong dependence. The calculated quantitative values of the coherent interlayer resistance increases approximately an order of magnitude when the broadening is changed from 1 meV to 10 meV. The resistance calculated using Eq. (5.6) with $\eta = 150$ meV is five times higher than that calculated using Eq. (5.3). Thus, this method fails to give correct quantitative values of interlayer coherent resistance between two misoriented layers of graphene. Therefore, we will use the exact method described in Sec. 5.2.1 for all the results shown below.

Fig. 5.4 shows the momentum resolved transmission $T(E, \mathbf{k})$ calculated using Eq. (5.3) in the first Brillouin zone for two structures at an energy of 0.5 eV. The left one is for ideal AB stacked graphite calculated using a supercell corresponding to the 21.8° structure. The transmission is centered at the K and K' points, and within the isoenergy circle, it is 1.0 as one would expect for an ideal crystal. The supercell of the 21.8° twisted structure is the smallest of all the nonzero twist angles. At other

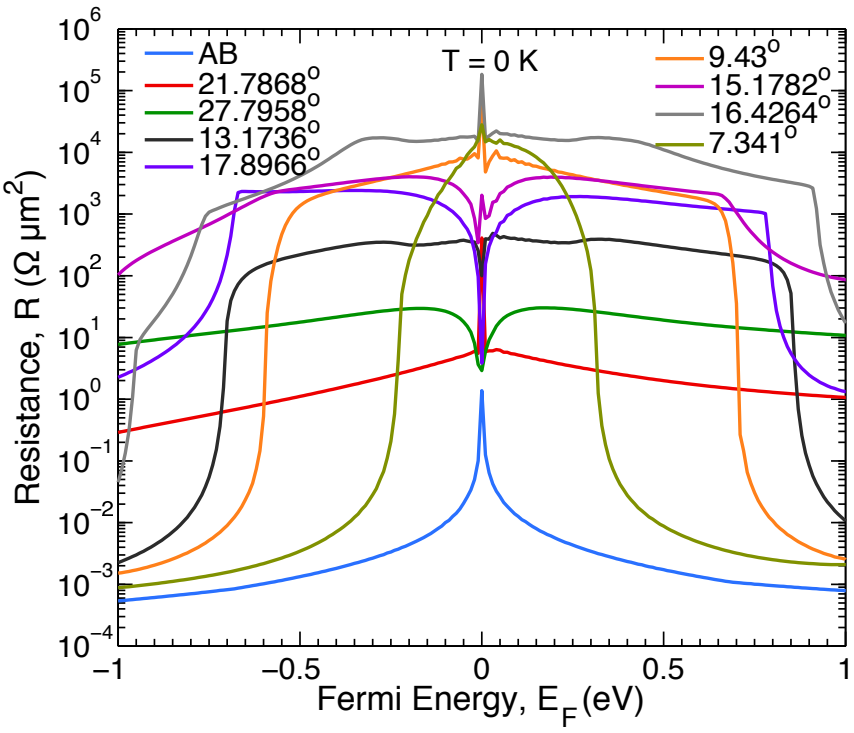

Figure 5.5: Zero temperature coherent contact resistance of twisted bilayer graphene as a function of Fermi Energy for different rotation angles.

angles, the supercell is larger and the first Brillouin zone becomes smaller as shown in Fig. 5.4b for a twist angle of 9.43°. It is still hexagonal, and the transmission is still centered around the K and K' points. However, now the transmission is peaked at the isoenergy surface. Furthermore, the overall scale has been reduced by 7 orders of magnitude (compare the scale bars on the left and right). At each energy E, these functions are integrated over the first Brillouin zone to obtain the transmission as a function of energy $T(E)$ and then the interlayer resistance from Eq. (5.1).

Fig. 5.5 shows the zero-temperature, interlayer resistance over a range of Fermi energies from ±1 eV around the charge neutrality point for different rotation angles θ. The lowest curve is the coherent resistance of the ideal AB stack with $\theta = 0°$. This resistance is the fundamental limiting 'quantum resistance' inversely proportional to the number of transverse modes available to carry the current at a given

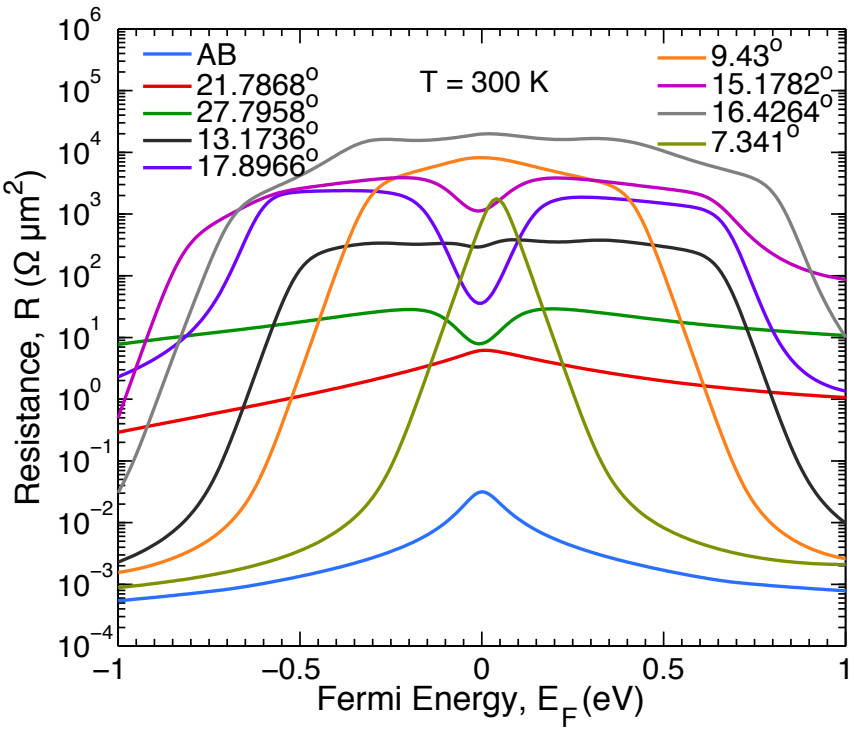

Figure 5.6: Room temperature coherent contact resistance of twisted bilayer graphene as a function of Fermi energy for different rotation angles.

energy. This quantity has recently been calculated for other materials to determine the fundamental lower limit on the contact resistance [110–112].

The magnitude of the coherent interlayer resistance increases several orders of magnitude as the layers become misaligned. The legend is ordered according to the size of the corresponding supercell so that, among the rotated bilayers, $\theta = 21.8°$ gives the smallest supercell and $\theta = 7.34°$ gives the largest supercell. In general, the magnitude of the resistance increases with the size of the supercell. However, the resistance for the two smallest angles, 7.34° and 9.43°, falls off most quickly with energy, so that at larger energies this trend can fail for the smaller rotation angles.

The coherent interlayer resistance at $T = 300$ K is shown in Fig. 5.6. It is obtained by convolving the transmission with the room temperature thermal broadening function in Eq. (5.1) which removes the sharpest features in Fig. 5.5. At a Fermi

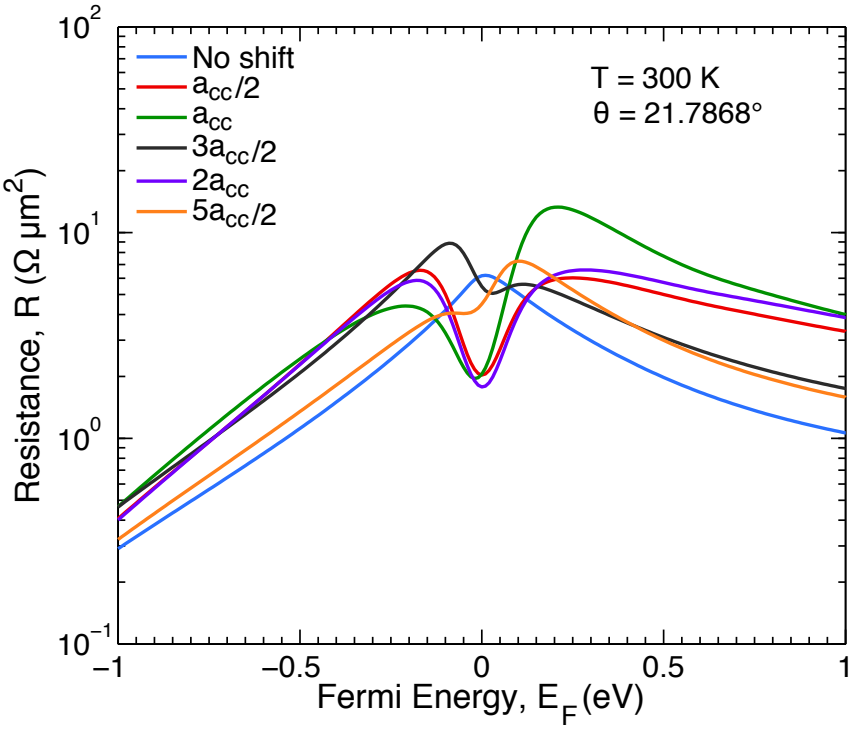

Figure 5.7: Room temperature coherent contact resistance of a 21.8° misoriented interface as a function of the Fermi energy for different relative in-plane translations.

energy of 0.26 eV considered in Refs. [3, 12], the trend of increasing resistance with supercell size is generally followed except for the two smallest angles, and the smallest angle of 7.34° falls far outside of the trend.

The coherent room temperature resistance is also sensitive to translation of one plane with respect to the other. Fig. 5.7 shows the room temperature resistance for different translations of one plane with respect to the other for a misorientation angle of 21.8°. The coherent resistance changes by a factor of 4 to 5 for different translations. The sensitivity to translation is far less than the sensitivity to rotation. Translation alters the coherent resistance value within the same order of magnitude, whereas rotation alters the coherent resistance by many orders of magnitude.

The total resistance is the parallel combination of the phonon-mediated resistance

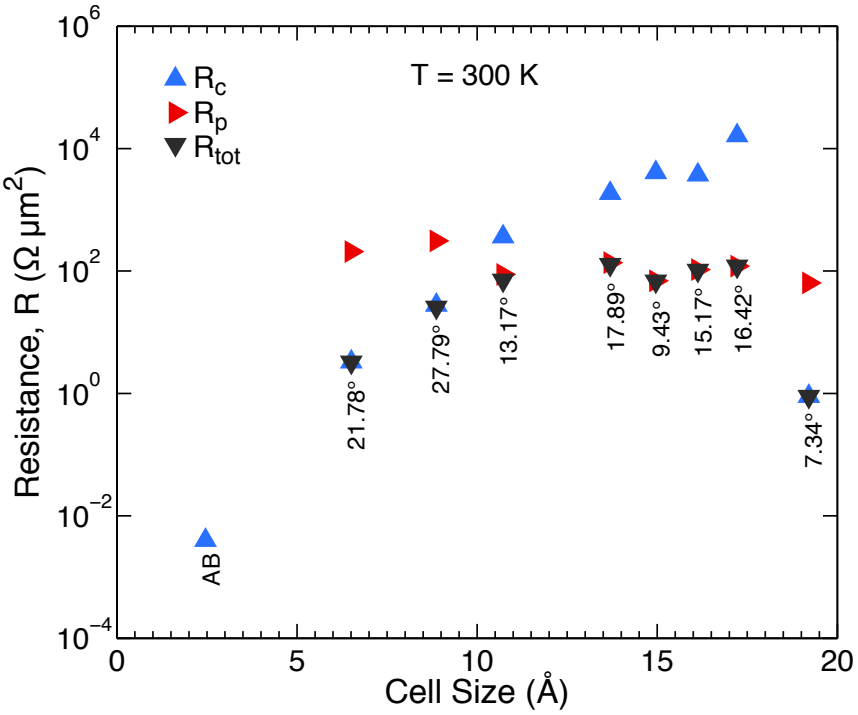

Figure 5.8: Coherent (R_c), phonon mediated (R_p) and total contact resistance ($R_{tot} = R_c||R_p$) as functions of cell size of twisted graphene at $E_F = 0.26$ eV and room temperature.

R_p and the coherent resistance R_c. The values for the room-temperature, phonon-mediated resistance R_p at a Fermi level of 0.26 eV are taken from Fig. 1 of Ref. [3]. The values for the coherent, room temperature resistance R_c at a Fermi level of 0.26 eV are taken from Fig. 5.6. These values along with the parallel combination R_{tot} are plotted in Fig. 5.8 as a function of the supercell lattice constant, and they are listed in Table 5.1. The rotation angle is shown on the plot for each set of resistances. For reference, the coherent resistance of the ideal AB structure is also shown. Its value of 3.9×10^{-3} $\Omega\mu\text{m}^2$ is 3 to 5 orders of magnitude less than that of any of the structures with a nonzero misorientation. For the two smallest cell sizes corresponding to 21.8° and 27.8°, the coherent resistance is smaller than the phonon-mediated resistance, and the total resistance is determined by the coherent resistance. The corresponding values of the total resistance are 3.2 $\Omega\mu\text{m}^2$ and 25 $\Omega\mu\text{m}^2$, respectively. For the intermediate cell sizes, the phonon-mediated resistance is less than the coherent resistance, so that the total resistance is determined by the phonon-mediated resistance. The value of the total resistance is on the order of 100 $\Omega\mu\text{m}^2$ for all of the intermediate cell sizes. The coherent resistance of the largest cell size corresponding to the smallest angle of 7.34° is two orders of magnitude smaller than the phonon-mediated resistance. Thus, for $\theta = 7.34°$, the total resistance is determined by the coherent resistance and its value is 0.9 $\Omega\mu\text{m}^2$.

The values for R_p taken from Ref. [3] must be viewed as an estimate using the best and most optimistic values available. Those were calculated from a Fermi golden rule expression using the calculated phonon modes of each misoriented bilayer with a misorientation angle θ and the initial and final density of states of single layer graphene. The system we consider consists of two misoriented semi-infinite stacks of AB graphite. This alters both the phonon modes and the initial and final density of states. The phonon modes are now three dimensional with a finite velocity

Rotation Angle θ	Lattice Constant	R_c	R_p	R_{tot}
AB	2.4595	3.89×10^{-3}		
21.7868	6.5073	3.28	208	3.23
27.7958	8.8679	27.7	311	25.5
13.1736	10.7208	363	87.8	70.7
17.8966	13.6940	1860	137	128
9.43	14.9606	4080	69.2	68.0
15.1782	16.1281	3720	105	102
16.4264	17.2166	16400	120	119
7.341	19.2094	0.902	64.0	0.890

Table 5.1: Coherent resistance R_c, phonon-mediated resistance R_p, and total resistance R_{tot} as a function of rotation angle and primitive-cell lattice constant. Resistance units are ($\Omega\mu\text{m}^2$). Angles are in degrees and the lattice constants are in Å. $T = 300$ K and $E_F = 0.26$ eV. The angles are ordered according to the supercell size from smallest to largest. The values for R_p are from Ref. [3].

perpendicular to the planes, and the initial and final density of states become the surface spectral functions of the two interface layers. Therefore, a re-calculation of the phonon-mediated interlayer resistance for a stacked structure is required to verify the values for R_p and, finally, R_{tot}. In the interim, the values for R_{tot} shown in Fig. 5.8 are the best and most optimistic ones available.

Assuming that the values for R_p are good estimates for the actual values, R_{tot} is still a sensitive function of the misorientation angle even in the presence of phonon-mediated transport. It varies by a factor of 40 as the angle is varied a few degrees from 17.9° to 21.8° and a factor of 76 as the angle varies from 9.4° to 7.3°. Over a range of intermediate angles, the interlayer resistance is determined by the phonon-mediated resistance with a relatively constant value near 100 $\Omega\mu\text{m}^2$ at a Fermi level of 0.26 eV. The resistance values for most angles are large for THz applications. If we take 1 $\Omega\mu\text{m}^2$ as an order-of-magnitude target resistance for THz applications, then only small misorientation angles with Fermi levels well away from the charge neutral point will meet the target. There is the one special angle of 21.8° that gives a minimal

primitive cell and a resistance in the target range, however, small variations away from that angle result in resistance values well outside of the target value.

5.4 Conclusion

In conclusion, we have calculated the coherent transmission and resistance of two semi-infinite stacks of AB graphite rotated with respect to each other at a commensurate angle θ. The values are well defined and they do not depend on an empirical energy broadening factor Γ. The fundamental limiting value is the coherent quantum-resistance of ideal AB graphene. It is on the order of 10^{-3} $\Omega\mu\text{m}^2$. For small misorientation angles, the coherent interlayer resistance is a strong function of the Fermi energy. It decreases rapidly towards the ideal, unrotated AB value at higher energies. For a wide range of intermediate angles the coherent interlayer resistance becomes very large (> 1000 $\Omega\mu\text{m}^2$), and the interlayer resistance is determined by the phonon-mediated resistance with a relatively constant value on the order of 100 $\Omega\mu\text{m}^2$. At room temperature, there can still be strong sensitivity of the resistance to the rotation angle. A few degrees of rotation can vary the resistance by one to two orders of magnitude. The general trends such as the strong energy dependence of the interlayer resistance for small angles should be relevant to other two-dimensional stacked materials.

Chapter 6

Conclusion

There is rapidly growing interest in vertically stacked van der Waals materials for electronic device applications. The most well studied and well understood van der Waals material is graphene. The effect of misorientation on the electronic structure of bilayer graphene has been studied extensively both theoretically and experimentally. After a few degrees misorientation, the in-plane dispersion becomes linear, and after about 10 degrees misorientation, the in-plane velocity is the same as that of single-layer graphene. Thus, misoriented graphene bilayers act as if they are electronically decoupled. The interlayer coupling can be modulated using an external electric field. This opens up possibilities for novel switching mechanism for post CMOS device applications.

In this work, we explored the quantum transport domain of misoriented layers of graphene for possible current switching mechanism that utilizes the exceptional properties of graphene. Our simulations show that the coherent electronic decoupling between two-dimensional misoriented bilayers is still present in lower dimensions when the overlap region is reduced to the nanometer scale. We found a current switching mechanism based on voltage control quantum phase of electrons to achieve large,

rapid modulation of current using a small voltage swing. This switching mechanism does not rely on a bandgap or a potential barrier. Therefore, it is not limited by the ideal thermal limitation of 60 mV/dec.

In vertically stacked van der Waals material devices the interfaces between different materials will, in general, be misoriented with respect to each other. The interlayer current and resistance is expected to be very sensitive to the rotation angle. Understanding the effect of the misorientation on the interlayer resistance is required to fully understand the design requirements and performance of proposed vertically stacked devices. In this work, the coherent, interlayer resistance of a misoriented, rotated interface in vertically stacked graphene is determined for a variety of misorientation angles and compared with previous values for the phonon-mediated, interlayer resistance.

The quantum transport simulations in misoriented layers of graphene were carried out using NEGF formalism. The Hamiltonian matrix element required for NEGF calculations were constructed using semi-empirical tight binding models, extended Hückel theory or density functional theory. Depending on the nature of the problem we started from simpler models and added sophistication of better models if necessary. The underlying physics governing the numerical results were elucidated using analytical models based on wave function approach. The critical findings of this work are summarized as follows:

- Two independently contacted, AA or AB stacked graphene nanoribbons behave as a resonant tunneling diode featuring negative differential resistance.

- A relative rotation of 90 degrees between two GNRs creates a crossbar with a nano-scale overlap region. The electronic states of the individual GNRs of an unbiased crossbar are decoupled from each other similar to the decoupling that

occurs in twisted bilayer graphene.

- The decoupling is a consequence of the cancellation of quantum phases of the electronic wavefunctions of the individual GNRs. As a result, the inter-GNR transmission is strongly suppressed over a large energy window.

- An external bias applied between the GNRs changes the relative phases of the wavefunctions resulting in modulation of the transmission and current by several orders of magnitude.

- A built-in potential between the two GNRs can lead to a large peak-to-valley current ratio (> 1000) resulting from the strong electronic decoupling of the two GNRs that occurs when they are driven to the same potential.

- Current switching by voltage control of the quantum phase in a graphene cross-bar does not rely on a bandgap or a potential barrier. Thus it is not limited by the fundamental thermal limitation of 60 mV/dec. It is robust even with an overlap of ~ 1.8 nm $\times$ 1.8 nm which is well-below the smallest horizontal length scale envisioned in the ITRS.

- The interlayer transport between two semi-infinite crossed GNRs is governed by the quantum interference between the standing waves of the individual GNRs.

- An external bias applied between the GNRs controls the wavelength and hence the relative phase of these standing waves.

- Sweeping the applied bias results in multiple constructive and destructive interference conditions.

- The oscillatory nature of the voltage controlled interference gives rise to an oscillatory current-voltage (I-V) response with multiple NDR regions.

- The period of oscillation is inversely proportional to the length of the finite ends of the GNRs.
- The fundamentally limiting quantum-resistance of the ideal AB stacked graphite is on the order of 10^{-3} $\Omega\mu\text{m}^2$.
- For small misorientation angles, the coherent interlayer resistance is a strong function of the Fermi energy. It decreases rapidly towards the ideal, unrotated AB value at higher energies.
- For a wide range of intermediate angles the coherent interlayer resistance becomes very large (> 1000 $\Omega\mu\text{m}^2$), and the interlayer resistance is determined by the phonon-mediated resistance with a relatively constant value on the order of 100 $\Omega\mu\text{m}^2$.
- At room temperature, there can still be strong sensitivity of the resistance to the rotation angle.
- A few degrees of rotation can vary the resistance by one to two orders of magnitude.
- The general trends such as the strong energy dependence of the interlayer resistance for small angles should be relevant to other two-dimensional stacked materials.

Bibliography

[1] K. M. M. Habib, F. Zahid, and R. K. Lake, "Negative differential resistance in bilayer graphene nanoribbons," *Applied Physics Letters*, vol. 98, no. 19, p. 192112, 2011. [Online]. Available: http://link.aip.org/link/?APL/98/192112/1

[2] K. M. M. Habib and R. K. Lake, "Current modulation by voltage control of the quantum phase in crossed graphene nanoribbons," *Phys. Rev. B*, vol. 86, p. 045418, Jul 2012. [Online]. Available: http://link.aps.org/doi/10.1103/PhysRevB.86.045418

[3] V. Perebeinos, J. Tersoff, and P. Avouris, "Phonon-mediated interlayer conductance in twisted graphene bilayers," *Phys. Rev. Lett.*, vol. 109, no. 23, p. 236604, 2012.

[4] X. Wu, X. Li, Z. Song, C. Berger, and W. A. de Heer, "Weak antilocalization in epitaxial graphene: Evidence for chiral electrons," *Phys. Rev. Lett.*, vol. 98, p. 136801, Mar 2007. [Online]. Available: http://link.aps.org/doi/10.1103/PhysRevLett.98.136801

[5] J. Hass, F. Varchon, J. Millán-Otoya, M. Sprinkle, N. Sharma, W. de Heer, C. Berger, P. First, L. Magaud, and E. Conrad, "Why multilayer graphene on 4h-sic($000\bar{1}$) behaves like a single sheet of graphene," *Phys. Rev. Lett.*, vol. 100, Jan 2008.

[6] B. Lopes dos Santos J. M., R. Peres N. M., and H. Castro Neto A., "Graphene bilayer with a twist: Electronic structure," *Phys. Rev. Lett.*, vol. 99, p. 256802, Jan 2007.

[7] S. Latil, V. Meunier, and L. Henrard, "Massless fermions in multilayer graphitic systems with misoriented layers: Ab initio calculations and experimental fingerprints," *Phys. Rev. B*, vol. 76, p. 201402, Jan 2007.

[8] S. Shallcross, S. Sharma, and O. A. Pankratov, "Quantum interference at the twist boundary in graphene," *Phys. Rev. Lett.*, vol. 101, no. 5, p. 056803, Aug 2008.

[9] A. Luican, G. Li, A. Reina, J. Kong, R. R. Nair, K. S. Novoselov, A. K. Geim, and E. Y. Andrei, "Single-layer behavior and its breakdown in twisted graphene layers," *Phys. Rev. Lett.*, vol. 106, no. 12, p. 126802, Mar 2011.

[10] E. Suárez Morell, P. Vargas, L. Chico, and L. Brey, "Charge redistribution and interlayer coupling in twisted bilayer graphene under electric fields," *Phys. Rev. B*, vol. 84, p. 195421, Nov 2011. [Online]. Available: http://link.aps.org/doi/10.1103/PhysRevB.84.195421

[11] L. Xian, S. Barraza-Lopez, and M. Chou, "Effects of electrostatic fields and charge doping on the linear bands in twisted graphene bilayers," *Phys. Rev. B*, vol. 84, Jan 2011.

[12] R. Bistritzer and H. MacDonald A., "Transport between twisted graphene layers," *Phys. Rev. B*, vol. 81, p. 245412, Jan 2010.

[13] S. Iijima, "Helical microtubules of graphitic carbon," *Nature*, vol. 354, pp. 56–58, 1991.

[14] J. Appenzeller, Y.-M. Lin, J. Knoch, Z. Chen, and P. Avouris, "Comparing carbon nanotube transistors - the ideal choice: a novel tunneling device design," *IEEE Trans. Elect. Dev.*, vol. 52, no. 12, pp. 2568 – 2576, 2005.

[15] K. S. Novoselov, A. K. Geim, S. V. Morozov, D. Jiang, M. I. Katsnelson, I. V. Grigorieva, S. V. Dubonos, and A. A. Firsov, "Two-dimensional gas of massless dirac fermions in graphene," *Nature*, vol. 438, no. 7065, pp. 197–200, November 2005.

[16] K. S. Novoselov, A. K. Geim, S. V. Morozov, D. Jiang, Y. Zhang, S. V. Dubonos, I. V. Grigorieva, and A. A. Firsov, "Electric Field Effect in Atomically Thin Carbon Films," *Science*, vol. 306, no. 5696, pp. 666–669, 2004.

[17] A. H. Castro Neto, F. Guinea, N. M. R. Peres, K. S. Novoselov, and A. K. Geim, "The electronic properties of graphene," *Rev. Mod. Phys.*, vol. 81, pp. 109–162, Jan 2009. [Online]. Available: http://link.aps.org/doi/10.1103/RevModPhys.81.109

[18] T. Ando, "Exotic electronic and transport properties of graphene," *Physica E: Low-dimensional Systems and Nanostructures*, vol. 40, no. 2, pp. 213 – 227, 2007.

[19] M. Y. Han, B. Özyilmaz, Y. Zhang, and P. Kim, "Energy band-gap engineering of graphene nanoribbons," *Phys. Rev. Lett.*, vol. 98, p. 206805, May 2007. [Online]. Available: http://link.aps.org/doi/10.1103/PhysRevLett.98.206805

[20] X. Li, X. Wang, L. Zhang, S. Lee, and H. Dai, "Chemically Derived, Ultrasmooth Graphene Nanoribbon Semiconductors," *Science*, vol. 319, no. 5867, pp. 1229–1232, 2008.

[21] K.-T. Lam and G. Liang, "An ab initio study on energy gap of bilayer graphene nanoribbons with armchair edges," *Applied Physics Letters*, vol. 92, no. 22, p. 223106, 2008.

[22] C. L. Lu, C. P. Chang, Y. C. Huang, J. M. Lu, C. C. Hwang, and M. F. Lin, "Low-energy electronic properties of the ab-stacked few-layer graphites," *Journal of Physics: Condensed Matter*, vol. 18, no. 26, p. 5849, 2006. [Online]. Available: http://stacks.iop.org/0953-8984/18/i=26/a=005

[23] H. Min, B. Sahu, S. K. Banerjee, and A. H. MacDonald, "Ab initio theory of gate induced gaps in graphene bilayers," *Phys. Rev. B*, vol. 75, no. 15, p. 155115, Apr 2007.

[24] Y. Zhang, T.-T. Tang, C. Girit, Z. Hao, M. C. Martin, A. Zettl, M. F. Crommie, Y. R. Shen, and F. Wang, "Direct observation of a widely tunable bandgap in bilayer graphene," *Nature*, vol. 459, no. 7248, p. 820, 2009.

[25] D. C. Elias, R. R. Nair, T. M. G. Mohiuddin, S. V. Morozov, P. Blake, M. P. Halsall, A. C. Ferrari, D. W. Boukhvalov, M. I. Katsnelson, A. K. Geim, and K. S. Novoselov, "Control of graphene's properties by reversible hydrogenation: Evidence for graphane," *Science*, vol. 323, no. 5914, pp. 610–613, 2009. [Online]. Available: http://www.sciencemag.org/content/323/5914/610.abstract

[26] K. Brenner and R. Murali, "Single step, complementary doping of graphene," *Applied Physics Letters*, vol. 96, no. 6, p. 063104, 2010. [Online]. Available: http://dx.doi.org/doi/10.1063/1.3308482

[27] D. B. Farmer, Y.-M. Lin, A. Afzali-Ardakani, and P. Avouris, "Behavior of a chemically doped graphene junction," *Applied Physics Letters*, vol. 94, no. 21, p. 213106, 2009. [Online]. Available: http://dx.doi.org/doi/10.1063/1.3142865

[28] G. Fiori and G. Iannaccone, "On the Possibility of Tunable-Gap Bilayer Graphene FET," *IEEE Electron Device Letters*, vol. 30, no. 3, pp. 261–264, March 2009.

[29] ——, "Ultralow-Voltage Bilayer Graphene Tunnel FET," *IEEE Electron Device Letters*, vol. 30, no. 10, pp. 1096–1098, Oct 2009.

[30] M. Gilbert, "Performance characteristics of scaled bilayer graphene pseudospin devices," *Electron Devices, IEEE Transactions on*, vol. 57, no. 11, pp. 3059 –3067, nov. 2010.

[31] S. K. Banerjee, L. F. Register, E. Tutuc, D. Reddy, and A. H. MacDonald, "Bilayer pseudospin field-effect transistor (bisfet): A proposed new logic device," *IEEE Elect. Dev. Lett.*, vol. 30, no. 2, pp. 158 – 160, 2009.

[32] P. Zhao, R. M. Feenstra, G. Gu, and D. Jena, "Symfet: A proposed symmetric graphene tunneling field-effect transistor," *IEEE Trans. Elect. Dev.*, vol. PP, no. 99, pp. 1 –7, 2013.

[33] L. Britnell, R. V. Gorbachev, R. Jalil, B. D. Belle, F. Schedin, A. Mishchenko, T. Georgiou, M. I. Katsnelson, L. Eaves, S. V. Morozov, N. M. R. Peres, J. Leist, A. K. Geim, K. S. Novoselov, and L. A. Ponomarenko, "Field-effect tunneling transistor based on vertical graphene heterostructures," *Science*, vol. 335, no. 6071, pp. 947–950, 2012. [Online]. Available: http://www.sciencemag.org/content/335/6071/947.abstract

[34] Y. Yoon and S. Salahuddin, "Barrier-free tunneling in a carbon heterojunction transistor," *Applied Physics Letters*, vol. 97, no. 3, p. 033102, 2010. [Online]. Available: http://dx.doi.org/doi/10.1063/1.3431661

[35] R. M. Feenstra, D. Jena, and G. Gu, "Single-particle tunneling in doped graphene-insulator-graphene junctions," *Journal of Applied Physics*, vol. 111, no. 4, p. 043711, 2012. [Online]. Available: http://link.aip.org/link/?JAP/111/043711/1

[36] T. Sohier and B. Yu, "Ultralow-voltage design of graphene pn junction quantum reflective switch transistor," *Applied Physics Letters*, vol. 98, no. 21, p. 213104, 2011. [Online]. Available: http://link.aip.org/link/?APL/98/213104/1

[37] V. H. Nguyen, A. Bournel, and P. Dollfus, "Large peak-to-valley ratio of negative-differential-conductance in graphene p-n junctions," *Applied Physics Letters*, vol. 109, no. 9, p. 093706, 2011. [Online]. Available: http://dx.doi.org/doi/10.1063/1.3587570

[38] V. N. Do and P. Dollfus, "Negative differential resistance in zigzag-edge graphene nanoribbon junctions," *Journal of Applied Physics*, vol. 107, no. 6, p. 063705, 2010. [Online]. Available: http://link.aip.org/link/?JAP/107/063705/1

[39] H. Ren, Q.-X. Li, Y. Luo, and J. Yang, "Graphene nanoribbon as a negative differential resistance device," *Applied Physics Letters*, vol. 94, no. 17, p. 173110, 2009. [Online]. Available: http://link.aip.org/link/?APL/94/173110/1

[40] S. Shallcross, S. Sharma, E. Kandelaki, and A. Pankratov O., "Electronic structure of turbostratic graphene," *Phys. Rev. B*, vol. 81, p. 165105, Apr 2010. [Online]. Available: http://adsabs.harvard.edu/abs/2010PhRvB..81p5105S

[41] L. Jiao, L. Zhang, L. Ding, J. Liu, and H. Dai, "Aligned graphene nanoribbons and crossbars from unzipped carbon nanotubes," *Nano Research*, vol. 3, pp. 387–394, Jan 2010.

[42] H. Yang, J. Heo, S. Park, H. J. Song, D. H. Seo, K.-E. Byun, P. Kim, I. Yoo, H.-J. Chung, and K. Kim, "Graphene barristor, a triode device with a gate-controlled schottky barrier," *Science*, vol. 336, no. 6085, pp. 1140–1143, 2012.

[43] S. Chuang, R. Kapadia, H. Fang, T. C. Chang, W.-C. Yen, Y.-L. Chueh, and A. Javey, "Near-ideal electrical properties of InAs/WSe_2 van der Waals heterojunction diodes," *App. Phys. Lett.*, vol. 102, no. 24, JUN 17 2013.

[44] T. Georgiou, R. Jalil, B. D. Belle, L. Britnell, R. V. Gorbachev, S. V. Morozov, Y.-J. Kim, A. Gholinia, S. J. Haigh, O. Makarovsky, L. Eaves, L. A. Ponomarenko, A. K. Geim, K. S. Novoselov, and A. Mishcheno, "Vertical field-effect transistor based on graphene-WS_2 heterostructures for flexible and transparent electronics," *Nature Nanotechnology*, vol. 8, no. 2, pp. 100 – 103, 2012.

[45] W. J. Yu, Z. Li, H. Zhou, Y. Chen, Y. Wang, Y. Huang, and X. Duan, "Vertically stacked multi-heterostructures of layered materials for logic transistors and complementary inverters," *Nat. Mat.*, vol. 12, pp. 246 – 252, 2013.

[46] W. Mehr, J. Dabrowski, J. Christoph Scheytt, G. Lippert, Y.-H. Xie, M. C. Lemme, M. Ostling, and G. Lupina, "Vertical graphene base transistor," *IEEE Elect. Dev. Lett.*, vol. 33, no. 5, pp. 691–693, 2012.

[47] D. Jena, "Tunneling trnasistors based on graphene and 2-D crystals," *Proc. IEEE*, vol. 101, no. 7, pp. 1585 – 1602, 2013.

[48] A. K. Geim and I. V. Grigorieva, "Van der waals heterostructures," *Nature*, vol. 499, pp. 419 – 425, 2013.

[49] M. J. W. Rodwell, M. Le, and B. Brar, "Inp bipolar ics: Scaling roadmaps, frequency limits, manufacturable technologies," *Proc. IEEE*, vol. 96, no. 2, pp. 271 – 286, 2008.

[50] G. Trambly de Laissardiere, D. Mayou, and L. Magaud, "Localization of dirac electrons in rotated graphene bilayers," *Nano Letters*, vol. 10, no. 3, pp. 804–808, 2010.

[51] J. M. B. Lopes dos Santos, N. M. R. Peres, and A. H. Castro Neto, "Continuum model of the twisted graphene bilayer," *Phys. Rev. B*, vol. 86, p. 155449, Oct 2012. [Online]. Available: http://link.aps.org/doi/10.1103/PhysRevB.86.155449

[52] S. Shallcross, S. Sharma, and O. Pankratov, "Emergent momentum scale, localization, and van hove singularities in the graphene twist bilayer," *Phys. Rev. B*, vol. 87, p. 245403, Jun 2013.

[53] Y. Kim, H. Yun, S.-G. Nam, M. Son, D. S. Lee, D. C. Kim, S. Seo, H. C. Choi, H.-J. Lee, S. W. Lee, and J. S. Kim, "Breakdown of the interlayer coherence in twisted bilayer graphene," *Phys. Rev. Lett.*, vol. 110, p. 096602, Feb 2013. [Online]. Available: http://link.aps.org/doi/10.1103/PhysRevLett.110.096602

[54] C. Caroli, R. Combescot, P. Nozieres, and D. Saint-James, "A direct calculation of the tunneling current: Iv. electron-phonon interaction effects," *J. Phys. C: Solid State Physics*, vol. 5, pp. 21–42, 1972.

[55] C. Rivas, R. Lake, W. R. Frensley, G. Klimeck, P. E. Thompson, , K. D. Hobart, S. L. Rommel, and P. R. Berger, "Full-band modeling of the excess current in a delta-doped silicon tunnel diode," *J. Appl. Phys.*, vol. 94, no. 8, pp. 5005–5013, 2003.

[56] K.-T. Lam and G. Liang, "A computational evaluation of the designs of a novel nanoelectromechanical switch based on bilayer graphene nanoribbon," in *IEEE Int. Electron Devices Meeting Tech. Dig.* New York: IEEE, 2009, pp. 37.3.1 – 37.3.4.

[57] K.-T. Lam, C. Lee, and G. Liang, "Bilayer graphene nanoribbon nanoelectromechanical system device: A computational study," *Applied Physics Letters*, vol. 95, no. 14, p. 143107, 2009. [Online]. Available: http://link.aip.org/link/?APL/95/143107/1

[58] O. F. Sankey and D. J. Niklewski, "Ab initio multicenter tight-binding model for molecular-dynamics simulations and other applications in covalent systems," *Phys. Rev. B*, vol. 40, no. 6, pp. 3979 – 3995, 1989.

[59] J. P. Lewis, K. R. Glaesemann, G. A. Voth, J. Fritsch, A. A. Demkov, J. Ortega, and O. F. Sankey, "Further developments in the local-orbital density-functional-theory tight-binding method," *Phys. Rev. B*, vol. 64, no. 19, p. 195103, 2001.

[60] Y.-W. Son, M. L. Cohen, and S. G. Louie, "Energy gaps in graphene nanoribbons," *Phys. Rev. Lett.*, vol. 97, no. 21, p. 216803, 2006. [Online]. Available: dx.doi.org/10.1103/PhysRevLett.97.216803

[61] J. W. González, H. Santos, M. Pacheco, L. Chico, and L. Brey, "Electronic transport through bilayer graphene flakes," *Phys. Rev. B*, vol. 81, no. 19, p. 195406, 2010.

[62] J. W. González, H. Santos, E. Prada, L. Brey, and L. Chico, Gate-controlled conductance through bilayer graphene nanoribbons, arXiv:1008.3255v1[cond-mat.mes-hall] (2010).

[63] J. L. Martins, N. Troullier, and S. H. Wei, "Pseudopotential plane-wave calculations for zns," *Phys. Rev. B*, vol. 43, no. 3, pp. 2213 – 2217, 1991.

[64] A. D. Becke, "Density-functional exchange-energy approximation with correct asymptotic behavior," *Phys. Rev. A*, vol. 38, no. 6, pp. 3098 – 3100, 1988.

[65] C. Lee, W. Yang, and R. G. Parr, "Development of the colle-salvetti correlation energy formula into a functional of the electron density," *Phys. Rev. B*, vol. 37, no. 2, pp. 785 – 789, 1988.

[66] J. Harris, "Simplified method for calculating the energy levels of weakly interacting fragments," *Phys. Rev. B*, vol. 31, pp. 1770–1779, 1985.

[67] W. M. C. Foulkes and R. Haydock, "Tight-binding models and density-functional theory," *Phys. Rev. B*, vol. 39, pp. 12 520–2536, 1989.

[68] A. A. Demkov, J. Ortega, O. F. Sankey, and M. P. Grumbach, "Electronic structure approach for complex silicas," *Phys. Rev. B*, vol. 52, no. 3, pp. 1618 – 1630, 1995.

[69] P. Jelinek, H. Wang, J. P. Lewis, O. F. Sankey, and J. Ortega, "Multicenter approach to the exchange-correlation interactions in ab initio tight-binding methods," *Phys. Rev. B*, vol. 71, no. 23, p. 235101, 2005.

[70] N. A. Bruque, M. K. Ashraf, T. R. Helander, G. J. O. Beran, and R. K. Lake, "Conductance of a conjugated molecule with carbon nanotube contacts," *Phys. Rev. B*, vol. 80, no. 15, p. 155455, 2009. [Online]. Available: dx.doi.org/10.1103/PhysRevB.80.155455

[71] J. Tomfohr and O. F. Sankey, "Theoretical analysis of electron transport through organic molecules," *J. Chem. Phys.*, vol. 120, no. 3, pp. 1542 – 1554, 2004.

[72] N. A. Bruque, R. R. Pandey, and R. K. Lake, "Electron transport through a conjugated molecule with carbon nanotube leads," *Phys. Rev. B*, vol. 76, no. 20, p. 205322, 2007. [Online]. Available: http://dx.doi.org/10.1103/PhysRevB.76.205322

[73] International Technology Roadmap for Semiconductors 2011 Ed. Emerging Research Devices (ERD). http://www.itrs.net/Links/2011ITRS.

[74] A. R. Botello-Mendez, E. Cruz-Silva, J. M. Romo-Herrera, F. Lopez-Urias, M. Terrones, B. G. Sumpter, H. Terrones, J.-C. Charlier, and V. Meunier, "Quantum transport in graphene nanonetworks," *Nano Letters*, vol. 11, no. 8, pp. 3058–3064, 2011. [Online]. Available: http://pubs.acs.org/doi/abs/10.1021/nl2002268

[75] M. Hanggi and L. O. Chua, "Cellular neural networks based on resonant tunneling diodes," *Intl. J. Cir. Th. App.*, vol. 29, pp. 487 – 504, 2001.

[76] K. M. M. Habib, A. Khitun, A. A. Balandin, and R. K. Lake, "Graphene nanoribbon crossbar nanomesh," in *2011 IEEE/ACM International Symposium on Nanoscale Architectures (NANOARCH)*, 2011, pp. 86 – 90.

[77] S. Khasanvis, K. M. M. Habib, M. Rahman, P. Narayanan, R. K. Lake, and C. A. Moritz, "Hybrid graphene nanoribbon-cmos tunneling volatile memory fabric," in *2011 IEEE/ACM International Symposium on Nanoscale Architectures (NANOARCH)*, 2011, pp. 189 – 195.

[78] J. P. Lewis, P. Jelinek, J. Ortega, A. A. Demkov, D. G. Trabada, B. Haycock, H. Wang, G. Adams, J. K. Tomfohr, E. Abad, H. Wang, and D. A. Drabold, "Advances and applications in the FIREBALL *ab initio* tight-binding molecular-dynamics formalism," *Phys. Stat. Sol. B*, vol. 248, no. 9, pp. 1989 – 2007, 2011.

[79] O. F. Sankey, A. A. Demkov, W. Windl, J. H. Fritsch, J. P. Lewis, and M. Fuentes-Cabrera, "The application of approximate density functionals to complex systems," *Int. J. Quantum Chem.*, vol. 69, pp. 327 – 340, 1998.

[80] M. Galperin, S. Toledo, and A. Nitzan, "Numerical computation of tunneling fluxes," *J. Chem. Phys.*, vol. 117, pp. 10 817–10 826, 2002.

[81] H. Zheng, Z. F. Wang, T. Luo, Q. W. Shi, and J. Chen, "Analytical study of electronic structure in armchair graphene nanoribbons," *Phys. Rev. B*, vol. 75, p. 165414, Apr 2007. [Online]. Available: http://link.aps.org/doi/10.1103/PhysRevB.75.165414

[82] B. Huard, J. A. Sulpizio, N. Stander, K. Todd, B. Yang, and D. Goldhaber-Gordon, "Transport measurements across a tunable potential barrier in graphene," *Phys. Rev. Lett.*, vol. 98, no. 23, p. 236803, Jun 2007.

[83] L. M. Zhang and M. M. Fogler, "Nonlinear screening and ballistic transport in a graphene $p - n$ junction," *Phys. Rev. Lett.*, vol. 100, no. 11, p. 116804, Mar 2008.

[84] K. Wakabayashi and M. Sigrist, "Zero-conductance resonances due to flux states in nanographite ribbon junctions," *Phys. Rev. Lett.*, vol. 84, pp. 3390–3393, Apr 2000.

[85] K. Wakabayashi, "Electronic transport properties of nanographite ribbon junctions," *Phys. Rev. B*, vol. 64, p. 125428, Sep 2001.

[86] H. Tong and M. W. Wu, "Strongly modulated transmissions in gapped armchair graphene nanoribbons with side-arm or on-site gate voltage," *Phys. Rev. B*, vol. 85, p. 205433, May 2012.

[87] Z. Z. Zhang, K. Chang, and K. S. Chan, "Resonant tunneling through double-bended graphene nanoribbons," *Applied Physics Letters*, vol. 93, no. 6, p. 062106, 2008.

[88] Z. Z. Zhang, Z. H. Wu, K. Chang, and F. M. Peeters, "Resonant tunneling through s- and u-shaped graphene nanoribbons," *Nanotechnology*, vol. 20, no. 41, p. 415203, 2009. [Online]. Available: http://stacks.iop.org/0957-4484/20/i=41/a=415203

[89] B. H. Zhou, W. H. Liao, B. L. Zhou, K.-Q. Chen, and G. H. Zhou, "Electronic transport for a crossed graphene nanoribbon junction with and without doping," *The European Physical Journal B*, vol. 76, no. 3, pp. 421–425, 2010.

[90] B. Zhou, B. Zhou, A. Zeng, and G. Zhou, "Electronic transport for pristine and doped crossed graphene nanoribbon junctions with zigzag interfaces," *Physics Letters A*, vol. 376, no. 20, pp. 1710 – 1713, 2012.

[91] L. Rosales, P. Orellana, Z. Barticevic, and M. Pacheco, "Transport properties of graphene nanoribbon heterostructures," *Microelectronics Journal*, vol. 39, no. 34, pp. 537 – 540, 2008.

[92] V. Hung Nguyen, J. Saint-Martin, D. Querlioz, F. Mazzamuto, A. Bournel, Y.-M. Niquet, and P. Dollfus, "Bandgap nanoengineering of graphene tunnel diodes and tunnel transistors to control the negative differential resistance," *Journal of Computational Electronics*, vol. 12, no. 2, pp. 85–93, 2013.

[93] S. B. Kumar, G. Seol, and J. Guo, "Modeling of a vertical tunneling graphene heterojunction field-effect transistor," *Applied Physics Letters*, vol. 101, no. 3, p. 033503, 2012.

[94] G. Fiori, A. Betti, S. Bruzzone, and G. Iannaccone, "Lateral graphenehbcn heterostructures as a platform for fully two-dimensional transistors," *ACS Nano*, vol. 6, no. 3, pp. 2642–2648, 2012.

[95] S. Khasanvis, K. M. M. Habib, M. Rahman, P. Narayanan, R. K. Lake, and C. A. Moritz, "Ternary volatile random access memory based on heterogeneous graphene-cmos fabric," in *2012 IEEE/ACM International Symposium on Nanoscale Architectures (NANOARCH)*, 2012, pp. 69–76.

[96] G. Kresse and J. Hafner, "Ab initio molecular dynamics for liquid metals," *Phys. Rev. B*, vol. 47, no. 1, pp. 558–561, Jan 1993.

[97] D. Kienle, J. I. Cerda, and A. W. Ghosh, "Extended h[u-umlaut]ckel theory for band structure, chemistry, and transport. i. carbon nanotubes," *Journal of Applied Physics*, vol. 100, no. 4, p. 043714, 2006. [Online]. Available: http://link.aip.org/link/?JAP/100/043714/1

[98] C. Tang, W. Yan, Y. Zheng, G. Li, and L. Li, "Dirac equation description of the electronic states and magnetic properties of a square graphene quantum dot," *Nanotechnology*, vol. 19, no. 43, p. 435401, 2008. [Online]. Available: http://stacks.iop.org/0957-4484/19/i=43/a=435401

[99] L. Brey and H. A. Fertig, "Electronic states of graphene nanoribbons studied with the dirac equation," *Phys. Rev. B*, vol. 73, p. 235411, Jun 2006. [Online]. Available: http://link.aps.org/doi/10.1103/PhysRevB.73.235411

[100] J.-C. Charlier, X. Gonze, and J.-P. Michenaud, "First-principles study of the electronic properties of graphite," *Phys. Rev. B*, vol. 43, pp. 4579–4589, Feb 1991. [Online]. Available: http://link.aps.org/doi/10.1103/PhysRevB.43.4579

[101] L. Jiang, Y. Zheng, C. Yi, H. Li, and T. Lü, "Analytical study of edge states in a semi-infinite graphene nanoribbon," *Phys. Rev. B*, vol. 80, p. 155454, Oct 2009. [Online]. Available: http://link.aps.org/doi/10.1103/PhysRevB.80.155454

[102] The resistance values in Ωcm given by Kim et al. are converted to $\Omega\mu\text{m}^2$ using an interlayer distance of 3.4 Å so that 1 Ωcm = 3.4 $\Omega\mu\text{m}^2$.

[103] W. Primak and L. H. Fuchs, "Electrical conductivities of natural graphite crystals," *Phys. Rev.*, vol. 95, pp. 22–30, Jul 1954. [Online]. Available: http://link.aps.org/doi/10.1103/PhysRev.95.22

[104] D. Z. Tsang and M. S. Dresselhaus, "The c axis electrical conductivity of kish graphite," *Carbon*, vol. 14, pp. 43 – 46, 1976.

[105] S. Ono, "C-axis resistivity of graphite in connection with stacking faults," *J. Phys. Soc. Jap.*, vol. 40, no. 2, pp. 498 – 504, 1976.

[106] T. Tsuzuku, "Studies on electronic processes in graphite during the last decade in Japan," *Carbon*, vol. 21, no. 4, pp. 415 – 427, 1983.

[107] K. Matsubara, K. Sugihara, and T. Tsuzuku, "Electrical resistance in the c direction of graphite," *Phys. Rev. B*, vol. 41, pp. 969–974, Jan 1990. [Online]. Available: http://link.aps.org/doi/10.1103/PhysRevB.41.969

[108] G. Venugopal, G. S. Kim, and S.-J. Kim, "Fabrication and characteristics of nanoscale stacked-tunneling-junctions on graphite flake using focused ion beam," *Jap. J. Appl. Phys.*, vol. 50, pp. 06GE06–1 – 06GE06–6, 2011.

[109] R. Lake, G. Klimeck, R. C. Bowen, and D. Jovanovic, "Single and multiband modeling of quantum electron transport through layered semiconductor devices," *J. Appl. Phys.*, vol. 81, no. 12, pp. 7845–7869, 1997.

[110] A. Baraskar, A. Gossard, and M. Rodwell, "Lower limits to specific contact resistivity," in *Indium Phosphide and Related Materials (IPRM), 2012 International Conference on*, 2012, pp. 196–199.

[111] J. J. M. Law, A. Carter, S. Lee, A. Gossard, and M. Rodwell, "Regrown ohmic contacts to inxga1-xas approaching the quantum conductivity limit," in *Device Research Conference (DRC), 2012 70th Annual*, 2012, pp. 199–200.

[112] J. Maassen, C. Jeong, A. Baraskar, M. Rodwell, and M. Lundstrom, "Full band calculations of the intrinsic lower limit of contact resistivity," *App. Phys. Lett.*, vol. 102, no. 11, pp. 111 605–111 605–4, 2013.

[113] http://arma.sourceforge.net.

[114] http://www.boost.org.

[115] http://www.boost.org/doc/libs/1_54_0/doc/html/mpi.html.

[116] N. A. Bruque, "High throughput ab initio modeling of charge transport for biomolecular-electronics," Ph.D. dissertation, University of California Riverside, Department of Electrical Engineering, in progress.

[117] T. R. Helander, M. S. Dissertation, University of California Riverside, 2010.

Appendix A

Twister User Manual

Twister is a C++ code that can calculate the electronic structure and transport of twisted or misoriented stacks of van der Waals materials including graphene and hBN. It was used to calculate the interlayer coherent resistance of misoriented layers of graphene presented in Chapter 5. It uses high performance math libraries like BLAS and LAPACK. Calculations are performed in parallel using the message passing interface (MPI).

Twister takes two input files: (1) an xml file for the simulation setup and (2) a standard Gaussian gjf file containing the atomic structure. Below, we provide two tutorials followed by the format of the xml file.

A.1 Tutorials

A.1.1 Graphene Bandstructure

To calculate bandstructure of graphene using Twister, create a simulation directory in your home directory. Create an xml file in the simulation directory with the following contents:

Listing A.1: grapheneEkLine.xml

```
<?xml version="1.0" encoding="UTF-8"?>

<Twister Version="0.6.1">

    <TBParams dtol="1E-3">
        <Param ec="0"/>
        <Param di0cc="1.42" ti0cc="3.16"/>
        <Param do0cc="3.35" to0cc="0.39" doXcc="0.0"/>
        <Param lmdxy="1.7" lmdz="0.6" alpha="1.65"/>
    </TBParams>

    <Calculation
        Active="true"
        Mode="BandStructure"
        OutPath="band"
        FileName="ekLine"
        NumBands="10"
    >
            <AtomicStructure FileName="grapheneEk.gjf">
                <Lattice a1="2.1300 1.2298" a2="2.1300 -1.2298"/>
        </AtomicStructure>

        <Neighbors Generate="true"/>
        <Bias>0.0</Bias>
        <KPoints>
            <KLine
                KxStart="0" KyStart="0"
                KxEnd="1.4749" KyEnd="0.8515"
                DelK="0.0005"
            />
```

```
31          <KLine
32              KxStart="1.4749" KyStart="0.8515"
33              KxEnd="0.7375" KyEnd="1.2773"
34              DelK="0.0005"
35           />
36           <KLine
37              KxStart="0.7375" KyStart="1.2773"
38              KxEnd="0" KyEnd="0"
39              DelK="0.0005"
40           />
41
42       </KPoints>
43    </Calculation>
44 </Twister>
```

This file holds all the details needed for the simulation. A detailed description of all the keywords used in List. A.1 is given in Sec. A.2. The `TBParams` tag lists the tightbinding parameters: (1) `ec`: C on-site energy, (2) `di0cc`: C-C in-plane nearest neighbor distance, (3) `do0cc`: C-C out-of-plane nearest neighbor distance, (4) `ti0cc`: C-C in-plane nearest neighbor tight binding parameter, (5) `to0cc`: C-C out-of-plane nearest neighbor tight binding parameter etc. The `Calculation` tag describes types of calculation to be performed (`Method="BandStructure"`), output directory (`OutPath="band"`), output filename (`FileName="ekLine"`), atomic structure filename (`FileName="grapheneEk.gjf"`), lattice vector (`a1="2.1300 1.2298"` `a2="2.1300 -1.229"`) and k-points. The k-points are specified by the `KLine` tags which tells Twister to create equally spaced k-points for the line segments from Γ through K and M to Γ.

The primitive cell of graphene contains two atoms described in List. A.2.

Listing A.2: grapheneEk.gjf

```
%chk=twistedEk.gjf.chk
%mem=6MW
%nproc=1
#p pbepbe/auto bepbe

graphene

0 1
C 0.00 0.00 0.00
C 1.42 0.00 0.00
```

Copy the Twister executable file `twister` to this simulation directory and run the simulation:

```
$ srun twister GrapheneEkLine.xml
```

Twister will calculate the band structure and save it in `band/ekLine_0.0000.dat` file. To convert this file to a MATLAB friendly mat file, issue:

```
$ ./convBandData band/ekLine_0.0000.dat
```

command. This will create `band/ekLine_0.0000.mat` file needed to plot the band structure. The bandstructure can be plotted using the following MATLAB script:

Listing A.3: plotGrapheneEkLine.m

```
clear all;
clc;

load('band/ekLine_0.0000.mat');

nbands = size(Ek, 1)-2;
nEV = nbands/2+2;
nEC = nEV + 1;
```

```
9
10 kx = Ek(1,:);
11 ky = Ek(2,:);
12
13 nk = [1:length(kx)];
14
15 figure;
16 plot(nk,Ek(nEV:nEC,:));
17 grid on;
18 set(gca,'Xtick',[1, 3407, 5202, length(kx)],'XTickLabel',{'\Gamma', 'K', 'M', '\
       Gammas'});
19 ylabel('Energy, E (eV)');
```

A.1.2 Transport Through AB Stacked Graphite

For the transport calculation, we create six layers AB stacked graphene. The bottom two AB layers constitute the bottom contact, the middle two layers constitute the device and the top two layers constitute the top contact. The resulting gjf file looks like this:

Listing A.4: grapheneTEk.gjf

```
1 %chk=twistedEk.gjf.chk
2 %mem=6MW
3 %nproc=1
4 #p pbepbe/auto bepbe
5
6 graphene
7
8 0 1
9 C 0.00 0.00 -8.375
```

```
C 1.42 0.00 -8.375
C 1.42 0.00 -5.025
C 2.84 0.00 -5.025
C 0.00 0.00 -1.675
C 1.42 0.00 -1.675
C 1.42 0.00 1.675
C 2.84 0.00 1.675
C 0.00 0.00 5.025
C 1.42 0.00 5.025
C 1.42 0.00 8.375
C 2.84 0.00 8.375
```

Here, atoms 1-4 constitute the bottom contact, 5-8 constitute the device and 9-12 constitute the top contact. The simulation setup file looks like this:

Listing A.5: grapheneTEk.xml

```
<?xml version="1.0" encoding="UTF-8"?>

<Twister Version="0.6.1">

    <TBParams dtol="1E-3">
        <Param ec="0"/>
        <Param di0cc="1.42" ti0cc="3.16"/>
        <Param do0cc="3.35" to0cc="0.39" doXcc="0.0"/>
        <Param lmdxy="1.7" lmdz="0.6" alpha="1.65"/>
    </TBParams>

    <Calculation
        Active="true"
        Mode="Transport"
        DeviceType="NonRGF"
        OutPath="trans"
```

```
        FileName="tekParallelo"
    >
                <AtomicStructure FileName="grapheneTEk.gjf">
                    <Lattice a1="2.1300 1.2298" a2="2.1300 -1.2298"/>
            <Layer
                BotContact="1 4"
                Device="5 8"
                TopContact="9 12"
            />
        </AtomicStructure>

        <Neighbors Generate="true"/>
        <Bias>0.0</Bias>
        <Energy Start="-1.2" End="1.2" DelE="0.01"/>
        <Eta>1E-3</Eta>
        <KPoints>
            <KParallelo
                K1x="1.4749" K1y="0.8515"
                K2x="-1.4749" K2y="0.8515"
                DelK="0.005"
            />
        </KPoints>
    </Calculation>
</Twister>
```

The simulation type is now changed to transport using `Mode="Transport"` tag. The output path and file name is also changed. The `BotContact="1 4"` attribute in the `Layers` tag tells Twister that the bottom contact consists of atom 1-4. Similarly `Device="5 8"` and `TopContact="9 12"` defines the device and the top contact, respectively. A uniform energy grid from -1.2 eV to 1.2 eV with 10 meV interval is

defined in the `Energy` tag. The one third of the first BZ is sampled using equally spaced k-points defined by the `KParallelo` tag.

To run the simulation in parallel in 16 nodes, we issue:

```
$ srun -n 16 twister grapheneTEk.xml
```

command. Twister will calculate transport and save the output in `trans/tekParallelo_0.0000.dat` file. The output file can be converted to MATLAB mat file using the following command.

```
$ ./convBandData band/tekParallelo_0.0000.dat
```

The following MATLAB script will plot the transmission.

Listing A.6: plotTEParallelo.m

```
clear all;
clc;

VV = 0.0;
plotTkParallelo = 'YES';
plotTkLine = 'NO';
plotTE = 'YES';

hBar = 1.054571628E-34;
e = 1.6E-19;

%% T(E,k)
EE = -0.6;

load(sprintf('tekParallelo_%0.4f.mat', VV));
nE = find(abs(E-EE)<1E-3);
nE = nE(1);

```

```
kt = k{nE};
kx = kt(:,1);
ky = kt(:,2);
kt = [];
Tk = TEk{nE};

nkx = 400;
nky = 400;

[kxs, kys] = meshgrid(linspace(min(kx), max(kx), nkx), linspace(min(ky), max(ky),
    nky));
Tks = griddata(kx, ky, Tk, kxs, kys);

if strcmp(plotTkParallelo, 'YES')
    figure;
    pcolor(kxs, kys, Tks);
    hold on;
    hold off;
    grid on;
    shading interp;
    axis equal;
    xlabel('k_x (1/A)');
    ylabel('k_y (1/A)');
    title(sprintf('E = %0.2f',EE));
    colorbar;
end

if strcmp(plotTkLine, 'YES')
    figure;
    plot(kx,ky,'.');
    grid on;
```

```
    axis equal;
    xlabel('k_x (1/A)');
    ylabel('k_y (1/A)');
end

%% T(E)
delk = 0.005;
factor = 3*delk^2*sin(pi/3);

TE = zeros(size(E));
for iE = 1 : length(E)
    TE(iE) = sum(TEk{iE});
end
TE = TE*factor;

G0 = 2*e^2/(hBar*2*pi)*1E16;

if strcmp(plotTE, 'YES')
    figure;
    plot(E, TE);
    grid on;
    xlabel('Energy, E (eV)');
    ylabel('Transmission, T (A^{-2})');

    figure;
    semilogy(E, TE);
    grid on;
    xlabel('Energy, E (eV)');
    ylabel('Transmission, T (A^{-2})');

    figure;
```

```
80      semilogy(E, 1./(TE*G0));
81      grid on;
82      xlabel('Energy, E (eV)');
83      ylabel('Resistance, R (\Omega cm^{2})');
84  end
```

A.2 Twister Tag Reference

In Twister, a simulation is defined in an xml file. In this section, we describe the tags and their attributes that define a simulation.

TBParams

The `TBParams` (tight binding parameters) tag contains multiple `Param` tags that define the tight binding parameters.

Param

Attributes:

- ec: C on-site energy in eV
- di0cc: C-C in-plane nearest neighbor distance in Å
- do0cc: C-C out-of-plane nearest neighbor distance in Å
- ti0cc: C-C in-plane nearest neighbor tight binding parameter in eV
- to0cc: C-C out-of-plane nearest neighbor tight binding parameter in eV
- lmdz: the parameter λ_z used in Eq. (5.5)
- lmdxy: the parameter λ_{xy} used in Eq. (5.5)

- alpha: the parameter α used in Eq. (5.5)

Calculations

The `Calculations` tag defines the calculation method, atomic structure, lattice vector, k-points, energy grid etc. An xml file can contain multiple `Calculations` tag but the one with `Active="true"` will be used for actual calculations.

Attributes:

- Active: true|false. The one with Active="true" will be used for actual calculations.
- DeviceType: NonRGF|RGF. Device type for NEGF calculations.
- OutPath: The path where the output file will be stored.
- FileName: The output filename.
- NumBands: Number of bands to be stored in the output file.

AtomicStructure

Defines the atomic structure.

Attributes:

- FileName: Name of the Gaussian gjf file.

Lattice

Defines the lattice vector.

Attributes:

- a1: a1="a1x a1y a1z" defines lattice vector $\vec{a}_1 = \vec{a}_{1x}\hat{x} + \vec{a}_{1y}\hat{y} + \vec{a}_{1z}\hat{z}$.
- a2: See a1.
- a3: See a1.

Layer

Defines the contacts and the device.

Attributes:

- BotContact: BotContact="1 4" defines the bottom contact consisting of atoms 1 to 4.
- Device: See BotContact.
- TopContact: See BotContact.

Neighbors

For debugging. Controls whether or not to save nearest neighboring supercells in a gjf file.

Attributes:

- Generate: true|false. True = save.
- FileName: Gjf filename for the neighbors.

KPoints

Defines how to generate the k-points.

KPoint

Individual k-points. For example, ⟨KPoint⟩0.0 0.0⟨/KPoint⟩ defines the Γ point.

KLine:

Creates a number of k-points that lie on a straight line joining two points.

Attributes:

- KxStart: x coordinate of the starting point.
- KyStart: y coordinate of the starting point.
- KxEnd: x coordinate of the ending point.
- KyEnd: y coordinate of the ending point.
- DelK: Δk.

KParallelo

Creates a parallelogram defined by $K_{1x}\hat{x} + K_{1y}\hat{y}$ and $K_{2x}\hat{x} + K_{2y}\hat{y}$ containing uniform mesh of k-points.

Attributes:

- K1x: K_{1x}.
- K1y: K_{1y}.

- K2x: K_{2x}.
- K2y: K_{2y}.
- DelK: Δk.

Bias

Defines the total bias between the top and the bottom contacts.

Potential

Defines how total bias drops within the device region. For example, ⟨`Potential StartAtom="1" EndAtom="4" Ratio="0.5"/`⟩ tells Twister that atom 1 to 4 has the potential energy of -bias*0.5 eV.

Energy

Defines the energy grid. For example, ⟨`Energy Start="-1.0" End="1.0" DelE="0.001"/`⟩ creates a uniform energy grid from -1.0 eV to 1.0 eV with 1 meV interval.

Eta

Defines η in eV.

A.3 Miscellaneous Scripts

The `convBandData` and `convTransData` scripts convert the band and the transmission outputs files to MATLAB friendly mat files. For completeness, we include those scripts below.

Listing A.7: convBandData: runs MATLAB script convBandDat2Mat.m for the conversion

```
#!/bin/bash
matlab -nosplash -nodesktop -nojvm -nodisplay -r "try, convBandDat2Mat('$1');
    catch, disp('ERROR!!'); end, quit"
```

Listing A.8: convTransData: runs MATLAB script convTransDat2Mat.m for the conversion

```
#!/bin/bash
matlab -nosplash -nodesktop -nojvm -nodisplay -r "convTransDat2Mat('$1'); quit"
```

Listing A.9: convBandDat2Mat.m: converts dat file to mat file

```
function convBandDat2Mat(datFile)

    Ek = load(datFile);
    matFile = [datFile(1:end-3), 'mat'];
    save(matFile);

end
```

Listing A.10: convTransDat2Mat.m: converts dat file to mat file

```
function convTransDat2Mat(datFile)
    [TEk, k, E] = importTek(datFile, []);

    matFile = [datFile(1:end-3), 'mat'];
    save(matFile);

end
```

Listing A.11: importTek.m: imports $T(E, \mathbf{k})$ from dat file to MATLAB cell array

```
function [T, k, EE] = importTek(fileName, E)
```

```
    fid = fopen(fileName, 'rt');

    iE = 1;
    while(~feof(fid))

        Ecell = textscan(fid, '%[E = ]%f');
        data = textscan(fid, '%f %f %f');

        if isempty(E)
            T{iE} = data{3};
            k{iE} = [data{1}, data{2}];
            EE(iE) = Ecell{2};
            iE = iE + 1;
        else
            if (abs(Ecell{2} - E) < 1E-4)
                T = data{3};
                k = [data{1}, data{2}];
                EE = E;
                break
            end
        end
    end
    fclose(fid);
end
```

Appendix B

C++ Libraries for Engineers: Armadillo and Boost

Armadillo [113] and Boost [114] are very useful C++ libraries for engineering and physics students. Armadillo provides high level abstraction over the low level math routines provided by BLAS and LAPACK libraries. Boost is a collection of widely useful, peer-reviewed C++ codes that can speed up the application development. It provides a C++ wrapper for low level MPI routines.

In Twister, these two libraries were used extensively. In this Appendix, we will discuss the installation procedure and some features of these libraries. In the following discussion, we assume that the reader has a working knowledge of C++ concepts, basic understanding of MPI and a good LINUX/UNIX background.

B.1 Boost

Boost is huge collection of C++ libraries. It is complementary to the standard C++ library. It helps programmers to speed up the application development by letting

them concentrate on the real problem they are trying to solve rather than bogged down to the lower level implementation details.

Boost library has a C++ wrapper (`boost::mpi`) for lower level MPI routines. By default, the MPI libraries are not enabled in boost libraries. In this section, we will discuss how to enable MPI and compile boost for the LATTE clusters. Later, we will provide a tutorial on how to use `boost::mpi` for transmitting user defined data types among multiple processes. A detailed documentation on boost can be found online in Ref. [114].

B.1.1 Compilation

Download the boost source code from Ref. [114], put it under ∼`/src` folder and untar the archive.

```
$ cd ~/src
$ tar -xvf boost_1_53_0.tar.bz2
```

A new folder named `boost_1_53_0` will be created. To configure boost for your host/-cluster, change directory to `boost_1_53_0` and use:

```
$ cd boost_1_53_0
$ ./bootstrap.sh
```

commands.

To enable MPI with boost we need to find out the MPI wrapper for C++ compiler (`mpic++`). To do that issue the following command:

```
$ which mpic++
```

In venti, `mpic++` is located at `/usr/local/bin/mpic++` but in excelso it is in `/usr/bin/mpic++`. Now edit `tools/build/v2/user-config.jam` file to include the following line for venti:

```
using mpi : /usr/local/bin/mpic++ ;
```

and for excelso:

```
using mpi : /usr/bin/mpic++ ;
```

Now that we have enabled MPI, let's configure it again:

```
$ ./bootstrap.sh --prefix=/usr/local
$ ./bootstrap.sh --show-libraries
```

The output of the last command should show that MPI is enabled now. Configuration is done, let's install it:

```
$ sudo ./b2 install | tee install.log
```

Boost libraries will be installed in `/usr/local/lib` and the header files will be installed in `/usr/local/include/boost` folder. Include boost in your program using:

```
#include <boost/mpi.hpp>
#include <boost/serialization/string.hpp>
#include <boost/serialization/access.hpp>
#include <boost/serialization/split_free.hpp>
namespace mpi = boost::mpi;
```

etc.

B.1.2 Transmitting User Defined Data Types Using boost::mpi

Sending and receiving built-in data types are easy using `boost::mpi`. Suppose you have a string and you want to broadcast it. For example, in the following code the master process a string to the slave processes.

```
#include <boost/mpi.hpp>
#include <boost/serialization/string.hpp>
#include <boost/serialization/access.hpp>
```

```
#include <boost/serialization/split_free.hpp>

using namespace std; // the standard namespace
namespace mpi = boost::mpi; // the mpi namespace

int main(int argc, char** argv){
    // master process id is 0
    const int master = 0;

    // initialize mpi, similar to calling MPI_Init()
    mpi::environment env(argc, argv);
    // the communicator object is responsible for
    // transmitting data, providing barriers etc.
    mpi::communicator world;

    string mpiTestString;

    // if this is the master process then initialize the string
    if (world.rank() == master){
        mpiTestString = "Hello world!";
    }

    // now we will broadcast this string to other
    // processes
    mpi::broadcast(world, mpiTestString, master);

    // print the mpiTestString
    cout << "Process# " << world.rank() << " says: " << mpiTestString;

    return 0;
}
```

If you compile and run this code in 4 cpu's, the output will be something like:

```
$ srun -n 4 hello
Process# 0 says: Hello world!
Process# 1 says: Hello world!
Process# 2 says: Hello world!
Process# 3 says: Hello world!
```

Thus, the string `mpiTestString` is actually broadcasted to all the processes.

Now, imagine you have your own data type defined by a class:

```
struct LatticeOpts{
    string a1;
    string a2;
    string a3;

    // your code goes here.
};
```

and you want to send/receive the objects of this class using MPI. To do so, your class must be 'serializable' which means that the data your class holds must be convertible to a sequence of bytes and vice versa. This can be done using `boost:serializable` library as follows.

```
#include <boost/serialization/access.hpp>

struct LatticeOpts{
    string a1;
    string a2;
    string a3;

    // your code goes here.

    // For MPI send/receive to work
```

```
    // declare this class as a friend of
    // boost::serialization::access class
    // so that the acces class can access your
    // class members.
    private:
    friend class boost::serialization::access;

    // Now define how your data can be serialized.
    template<class Archive>
    void serialize(Archive& ar, const unsigned int version){
        // add one line for each of your members
        ar & a1;
        ar & a2;
        ar & a3;
    }
};
```

In the code listed above, we have declared the `LatticeOpts` class as friend of `boost::serialization::access` class so that it can access our class members. Next we define how to serialize our class in the `serialize()` function. Inside this function we are archiving our class members one by one. Now it is possible to send/receive the object of `LatticeOpts` class using mpi.

```
LatticeOpts lvopts;

// your code goes here
// ...

mpi::broadcast(world, lvopts, master);

// your code goes here
```

```
// ...
```

In the master process, the `broadcast()` function will call the `serialize()` function to convert data members of `LatticeOpts` to a sequence of bytes and send it to the other processes over the network. In the other processes, `broadcast()` function will receive the sequence of bytes and call the `serialize()` function to convert it to suitable data types and assign those data to the data members.

A more detailed documentation of the MPI wrapper library can be found in Ref. [115].

B.2 Armadillo

Armadillo is a C++ linear algebra library aiming towards a good balance between speed and ease of use. It uses BLAS and LAPACK to perform the actual calculations. Thus, it is numerically efficient. The syntax is similar to MATLAB.

In this section, we will show how to compile armadillo on the LATTE clusters and present some of the codes I had to write to integrate armadillo with boost.

B.2.1 Compilation

Download armadillo source `armadillo-3.800.2.tar.gz` from Ref. [113] and put it in ∼`/src` directory. Untar the source and change to `armadillo-3.800.2` directory. By default armadillo cannot find Intel MKL and/or AMD ACML math libraries in venti and excelso clusters. For compiling armadillo on excelso using MKL change the `build_aux/cmake/Modules/ARMA_FindMKL.cmake` file so that the first few lines look like:

```
IF(CMAKE_SIZEOF_VOID_P EQUAL 8)
  SET(MKL_NAMES ${MKL_NAMES} mkl_intel_lp64)
```

```
3  ELSE(CMAKE_SIZEOF_VOID_P EQUAL 8)
4    SET(MKL_NAMES ${MKL_NAMES} mkl_intel)
5  ENDIF(CMAKE_SIZEOF_VOID_P EQUAL 8)
6
7  SET(MKL_NAMES ${MKL_NAMES} mkl_intel_thread)
8  SET(MKL_NAMES ${MKL_NAMES} mkl_core)
9  SET(MKL_NAMES ${MKL_NAMES} iomp5)
10 # Not needed/supported by MKL 11.0
11 #SET(MKL_NAMES ${MKL_NAMES} mkl_lapack)
12 #SET(MKL_NAMES ${MKL_NAMES} guide)
13 #SET(MKL_NAMES ${MKL_NAMES} mkl)
14
15 FOREACH (MKL_NAME ${MKL_NAMES})
16   FIND_LIBRARY(${MKL_NAME}_LIBRARY
17     NAMES ${MKL_NAME}
18         PATHS /usr/local/intel/mkl/lib/intel64 /usr/local/intel/lib/intel64
19     )
20
21   SET(TMP_LIBRARY ${${MKL_NAME}_LIBRARY})
22
23   IF(TMP_LIBRARY)
24     SET(MKL_LIBRARIES ${MKL_LIBRARIES} ${TMP_LIBRARY})
25   ENDIF(TMP_LIBRARY)
26 ENDFOREACH(MKL_NAME)
```

Note that MKL is installed in `/usr/local/intel` on excelso. For venti, the MKL is located at `/usr/local/intel/Compiler/11.1/056`. Therefore, you will need to modify line#18 for venti. Now, we are ready to compile armadillo. The following commands configure armadillo to use MKL, compile and install.

```
1  $ cmake .
```

```
$ make
$ make install
```

Armadillo will be installed in `/usr/local/lib64` and the header files will be installed in `/usr/local/include`. Include armadillo in your program using the following code.

```
#include <armadillo>
using namespace arma;
```

AMD ACML can be integrated with armadillo using similar procedure. Only difference is that now you will have to change the `build_aux/cmake/Modules/ARMA_FindACML.cmake` so that the first few lines look like the following.

```
SET(ACML_NAMES ${ACML_NAMES} acml)
FIND_LIBRARY(ACML_LIBRARY
  NAMES ${ACML_NAMES}
  PATHS /usr/local/amd/acml/gfortran64/lib/
)
```

B.2.2 Integrating armadillo with boost::mpi

Using armadillo library, it is very easy to create, manipulate and perform matrix operations. For example, in the follwing code, in line#1 a double complex 2-dimensional matrix `TkDT` is declared. In line#8, $\Sigma^t_{11} = t_{dt} g^s_t t^\dagger_{dt}$ is calculated. Similarly, line#16 calculates $G_{11} = \left[E\mathrm{I} - H_d(\mathbf{k}) - \Sigma^t_{11} - \Sigma^b_{11}\right]^{-1}$. In the backend, the BLAS and LAPACK are used for performing these operations.

```
cx_mat TkDT; // coupling matrix between device and top contact
cx_mat gst; // surface green function of top contact

// ...
```

```
// some code
// ...

cx_mat sig11Tp = TkDT*gst*trans(TkDT); // sigma top layer
cx_mat sig11Bt = trans(TkBD)*gsb*TkBD; // sigma bottom layer

// ...
// some code
// ...

cx_mat G11 = E*eye<cx_mat>(HkD.n_rows, HkD.n_cols); // G11 = E*I
G11 = inv(G11 - HkD - sig11Tp - sig11Bt); // G11 = inv[EI - H - SigL - SigR]

// ...
// some code
// ...
```

Armadillo matrices and vectors are dynamic in memory. The memory allocation and deallocation is done automatically on the fly.

In parallel programs it is important to exchange matrices between multiple processes. In order to transmit armadillo matrices and vectors using `boost::mpi`, we need to define `serialize()` functions for those matrices and vectors as shown below.

```
#include <string>
#include <sstream>
#include <armadillo>
#include <boost/serialization/access.hpp>
#include <boost/serialization/string.hpp>
#include <boost/serialization/split_free.hpp>

using namespace std;
```

```
9  using namespace arma;
10
11 namespace boost {namespace serialization {
12
13 //---- For stringstream ----
14 template<class Archive>
15 void save(Archive& ar, const stringstream& ss, const unsigned int version){
16     string s = ss.str();
17     ar & s;
18 };
19
20 template<class Archive>
21 void load(Archive& ar, stringstream& ss, const unsigned int version){
22     string s;
23     ar & s;
24     ss.str(s);
25 };
26
27 template<class Archive>
28 inline void serialize(Archive& ar, stringstream& ss, const unsigned int
       file_version){
29     split_free(ar, ss, file_version);
30 };
31
32 //---- For svec ----
33 template<class Archive>
34 void serialize(Archive& ar, svec& sv, const unsigned int version){
35     ar & sv(X);
36     ar & sv(Y);
37     ar & sv(Z);
38 };
```

```
39
40 //---- For Mat: armadillo matrices ----
41 template<class Archive, class T>
42 void save(Archive& ar, const Mat<T>& m, const unsigned int version){
43     stringstream ss;
44     m.save(ss);
45     ar & ss;
46 };
47
48 template<class Archive, class T>
49 void load(Archive& ar, Mat<T>& m, const unsigned int version){
50     stringstream ss;
51     ar & ss;
52     m.load(ss);
53 };
54
55 template<class Archive, class T>
56 inline void serialize(Archive& ar, Mat<T>& m, const unsigned int file_version){
57     split_free(ar, m, file_version);
58 };
59
60 //---- For Col: armadillo column vector ----
61 template<class Archive, class T>
62 void save(Archive& ar, const Col<T>& m, const unsigned int version){
63     stringstream ss;
64     m.save(ss);
65     ar & ss;
66 };
67
68 template<class Archive, class T>
69 void load(Archive& ar, Col<T>& m, const unsigned int version){
```

```
    stringstream ss;
    ar & ss;
    m.load(ss);
};

template<class Archive, class T>
inline void serialize(Archive& ar, Col<T>& m, const unsigned int file_version){
    split_free(ar, m, file_version);
};

}}
```

Defining these functions will allow you to transmit armadillo matrices and vectors through mpi:

```
// ...
// some code
// ...

cx_mat sig11Tp; //some matrix

// calculate sig11Tp on the master process and send it
// to the slaves
if (world.rank() == master){
    sig11Tp = TkDT*gst*trans(TkDT);
}

// Now we will broadcast this matrix to other
// processes
mpi::broadcast(world, sig11Tp, master);


```

```
18 // ...
19 // some code
20 // ...
```

In the master process, the `broadcast()` function calls the `serialize(Archive& ar, Mat⟨T⟩& m, const unsigned int file_version)` function which, in turn, calls the `void save(Archive& ar, const Mat⟨T⟩& m, const unsigned int version)` function. This `save` function converts the matrix to a string stream and broadcast it over the network. In the other processes, the `broadcast()` calls the same `serialize()` function but this time the `serialize()` function calls `void load(Archive& ar, Mat⟨T⟩& m, const unsigned int version)` function. This `load` function receives the string stream from the master, convert it to matrix and assign it to matrix `sig11Tp`.

Thus, once these `serialize()` functions are included in the code, it is very easy to use boost::mpi functions for transmitting matrices and vectors over the network.

Appendix C

Linux Beowulf Clusters

To facilitate computation, LATTE group has four Linux Beowulf Clusters: Supremo, Mocha, Venti and Excelso. Supremo and Mocha were built by Nicolas Bruque in 2004 and 2006 respectively [116]. These two clusters are now decommissioned. Venti was built by Thomas Helander in fall of 2009 [117]. These clusters have been being maintained by K M Masum Habib since 2010. The newest cluster, Excelso, was assembled by K M Masum Habib, Mahesh Neupane, Carlos Velasco and Supeng Ge and is being configured by K M Masum Habib.

Venti has one master node and 10 slave nodes. Each node of Venti has two quad-core Intel Xeon E5405s (45nm) processor. Most of these nodes have 64 GB ECC DDR2 667MHz RAM, while three of the nodes have 32 GB of RAM. All the nodes are mounted on a 42U rack. The cluster is connected via gigabit ethernet. Venti has total 88 CPUs and 600 GB of RAM running CentOS5.3. The cluster is monitored using Ganglia and job control is performed by SLURM.

Excelso, shown in Fig. C.1, is he most recent and advanced cluster of LATTE group. It has one master node and 12 slave nodes. Each of the slave nodes has two AMD Opteron 6320 8-Core 2.8GHz processor, 128 GB Kingston DDR3-1333MHz

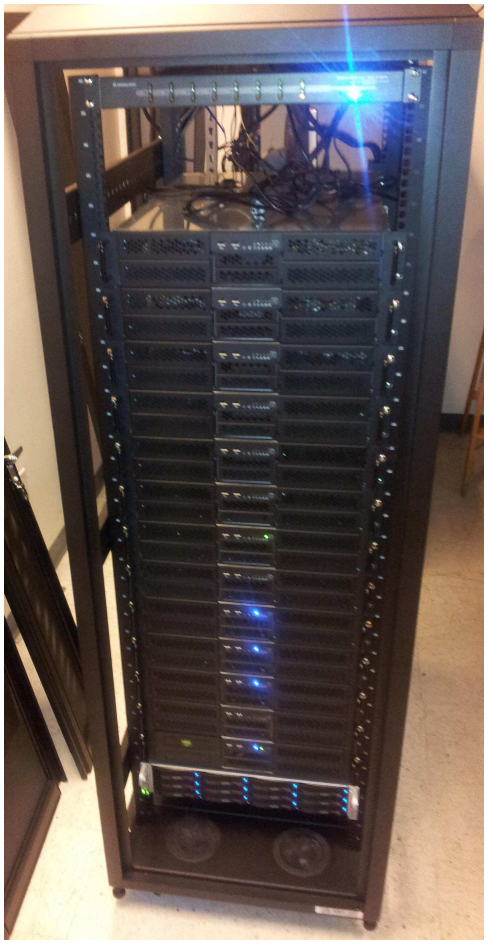

Figure C.1: Server rack containing the Excelso cluster and Calypso fileserver.

ECC REG Memory and one 128 GB M4 CT128M4SSD2 SSD. The master node has the same configuration except that it has two 480GB Samsung SM843 SSD configured in RAID1 and two 2TB Seagate ST2000NM0033 ES.3 SATA in RAID1 for operating system, software and data storage. The nodes are connected using gigabit ethernet using a Netgear GS748TS-100NAS 48-port Gigabit Smart Switch. Like Venti, the Excelso cluster is also mounted on a 36U rack to save floor space in the cluster room. In total, Excelso has 208 CPUs and 1.6 TB of RAM.

Excelso runs CentOS 6.4. It is monitored by Ganglia. The jobs are managed by SLURM. Libraries installed are: Intel MKL, AMD ACML, MPICH2 Boost and Armadillo. Computational tools installed are: MATLAB, COMSOL and Gaussian. Compilers and IDEs: Intel Fortran, Intel C/C++, AMD Open64, GCC, NetBeans and Eclipse.

A new fileserver, Calypso, was also built with Excelso. Calypso has one AMD Opteron 6320 8-Core 2.8GHz CPU, 32 GB Kingston DDR3-1333MHz ECC Memory, two 128 GB Crucial M4 CT128M4SSD2 SSD and twelve Seagate 2TB ST2000NM0033 HDD. It runs FreeBSD9.1 utilizing the state-of-the-art ZFS filesystem. The hard drives are configured as two RAID-Z2 devices providing 14TB of storage. ZFS also provides compression built-into the filesystem: 1.3 TB of data on Lattelocker is 750 GB on Calypso. It can tolerate upto four simultaneous disk failures

Calypso stores the users' home directories. In addition, it serves the the cluster maintenance website, the Ganglia webpage and user authentication (LDAP). Other services provided by Calypso include: DHCP, DNS, Network Boot (PXE), CentOS6.4 software repository, Data Backup, SAMBA etc.